Title

Finite Element Analysis of Cyclic Normal and Sliding Contact of Elastic-Plastic Homogeneous and Layered Half-Space Media — Effects of Interfacial Properties and Topography on Deformation Behavior

Author

Cen, Jialiang

Publication Date

2024

Peer reviewed|Thesis/dissertation

Finite Element Analysis of Cyclic Normal and Sliding Contact of Elastic-Plastic Homogeneous and Layered Half-Space Media – Effects of Interfacial Properties and Topography on Deformation Behavior

By

Jialiang Cen

A dissertation submitted in partial satisfaction of the
requirements for the degree of

Doctor of Philosophy

in

Engineering – Mechanical Engineering

in the

Graduate Division

of the

University of California, Berkeley

Committee in charge:

Professor Kyriakos Komvopoulos, Chair

Professor Peter Hosemann

Professor Grace Gu

Summer 2024

Finite Element Analysis of Cyclic Normal and Sliding Contact of Elastic-Plastic Homogeneous and Layered Half-Space Media – Effects of Interfacial Properties and Topography on Deformation Behavior

By

Jialiang Cen

Abstract

Finite Element Analysis of Cyclic Normal and Sliding Contact of Elastic-Plastic Homogeneous and Layered Half-Space Media – Effects of Interfacial Properties and Topography on Deformation Behavior

By

Jialiang Cen

Doctor of Philosophy in Engineering – Mechanical Engineering

University of California, Berkeley

Professor Kyriakos Komvopoulos, Chair

Fundamental understanding of contact interactions between two surfaces is of paramount importance as surface-surface contact phenomena can be found in a wide range of applications, such as microelectromechanical systems (MEMS), wire bonding in electronic packaging, total joint replacements (TJR), oscillating-slide actuators, bolted and riveted joints, shroud and snubber in turbine blades, and components operating in a microgravity environment. As result of contact interactions, material loss occurs and can lead to undesirable outcomes. Therefore, the primary objective of this dissertation was to develop a finite element method (FEM) based framework to investigate the effects of cyclic normal and shear (friction) traction, coefficient of friction, and surface topography on material damage, removal rate, and failure mechanisms.

First, the problem of a rigid flat and a patterned surface pressed against an elastic-plastic half-space exhibiting isotropic strain hardening was analyzed using the FEM to elucidate the development of plasticity. Simulation results in dimensionless form were obtained and discussed to illuminate the effects of geometry, imprint depth, and coefficient of friction on the evolution of plasticity. The deformation due to the impression of the patterned surface was largely affected by the interaction of the stress and strain fields produced by neighboring protrusions, resulting in a three-stage normal force response. Examination of plastic flow of the half-space material into the pattern cavities revealed that cavity filing became prominent with increasing protrusion distance of the patterned surface and decreasing coefficient of friction. This study introduced a computational methodology for fine-tuning key design and process parameters aimed to enhance the efficiency of metal imprinting.

Next, a plane-strain FEM model of a rigid cylinder in reciprocating sliding contact with an elastic-plastic half-space exhibiting isotropic strain hardening was introduced to investigate plasticity-induced damage leading to material loss in oscillatory sliding contact. By incorporating a quasi-static, isothermal damage model based on a ductile material failure criterion into the developed FEM model, plasticity-induced cumulative damage was tracked in terms of a dimensionless damage parameter. Numerical results yielded insight into the effects of normal load and coefficient of friction on material loss due to the accumulation of plasticity with oscillation cycles. Specifically, plastic deformation and wear increased with the number of cycles and coefficient of friction due to the intensification of plastic shearing. A non-monotonic increase

of wear with normal load was observed, which was explained by the distribution of plastic shear strain produced under high- and low-load oscillatory sliding conditions and the decrease of the fraction of contact area where slip occurred with the increase of the normal load. The developed computational methodology for exploring the evolution of plasticity, damage, and material loss in reciprocating sliding contacts is an effective tool for assessing the effects of load, friction, and material behavior on the mechanical performance of mechanical systems with components experiencing oscillatory contact.

Although most engineering surfaces are nominally smooth, they demonstrate random roughness over a wide range of nano/micro-scales. Henceforth, it is imperative to develop numerical models of the material removal rate for engineering interfaces undergoing reciprocating sliding that take into account the effect of the interface topography. To this end, an elastic-plastic contact mechanics analysis of an isotropic strain hardening half-space in oscillatory sliding contact with a rigid surface exhibiting multi-scale roughness characterized by fractal geometry was performed with the FEM. Cumulative damage was tracked by a dimensionless damage parameter and material stiffness degradation was modeled by a degradation parameter depending on fracture energy. Aside from the subsurface stress and plastic strain fields, the effects of fractal parameters (roughness) on the material removal rate were investigated. Contrary to the classical wear law, which predicts a liner dependence of wear rate on normal load, the material removal rate was found to exhibit a nonlinear dependence on normal load due to the occurrence of material interlocking introduced by the increase of surface conformity and the evolution of material loss. The developed model can be used to perform parametric studies of the material loss in mechanical devices operating in reciprocating sliding contact mode.

Delamination is a common failure process in layered materials. Thus, to provide insight into this fundamental problem, a contact mechanics analysis of interfacial delamination in elastic and elastic-plastic homogeneous and layered half-spaces in sliding contact was performed. A surface-based cohesive zone model was implemented in the FEM analysis to model surface separation at the interface. Complete delamination was determined by the critical separation distance of interfacial node pairs in mixed-mode loading based on a damage initiation criterion, exemplified by a quadratic relation of the interfacial normal and shear tractions. Linear stiffness degradation was accounted for by a scalar degradation parameter based on the effective separation distances corresponding to the critical effective cohesive strength and the fully degraded stiffness, defined by a mixed mode loading critical fracture energy criterion. Numerical results of the delamination profiles, stress fields, and plastic strain in both the surface layer and underlying half-space illuminated the effects of indentation depth and sliding distance on interfacial delamination for different combinations of elastic-plastic properties, cohesive strength, and layer thickness. The introduced model provides a capability for analyzing plasticity-induced cumulative damage in multilayered structures.

The investigations comprising this dissertation provide fundamental understanding of the evolution of stresses, plasticity, material loss, and delamination in contact surfaces subjected to normal loading, sliding, and small-amplitude oscillatory contact. The computational models of this work can be extended to study material loss (wear) in various applications involving contact interfaces, such as MEMS, TJR, and high-efficiency gas turbines.

Dedications

To my beloved wife, Siyao, for her unwavering support and unselfish love.

To my father, mother, grandfather, and grandmother, for raising me up and their unconditional love and support.

To my uncle and aunt for renting their garage to me.

Table of Contents

Dedications i
Table of Contents ii
List of Figures iv
List of Tables viii
Acknowledgements ix
Chapter 1 *Introduction* 1
Chapter 2 *On the mechanics of metal imprinting by nominally flat and patterned rigid surfaces* 4
2.1. Introduction 4
2.2. Simulation Procedure 6
2.2.1. Finite element modeling 6
2.2.2. Elastic-plastic material behavior 8
2.2.3. Dimensionless parameters 10
2.3. Results and discussion 10
2.3.1. Imprinting by a flat surface 10
2.3.2. Imprinting by a patterned template surface 12
2.4. Conclusions 21
Chapter 3 *Plasticity-induced damage and material loss in oscillatory contacts* 22
3.1. Introduction 22
3.2. Modeling Approach 24
3.2.1. Finite element mesh 24
3.2.2. Damage and degradation model 25
3.2.3. Constitutive model 28
3.2.4. Finite element simulations 29
3.2.5. Dimensionless parameters 29
3.3. Results and Discussion 29
3.4. Conclusions 35
Chapter 4 *A mechanics analysis of plasticity-induced damage leading to material loss at fractal contact interfaces undergoing fretting wear* 37
4.1. Introduction 37
4.2. Modeling and Computational Approaches 39

4.2.1. Surface Characterization 39
4.2.2. Finite Element Model 40
4.2.3. Damage Model 41
4.2.4. Constitutive Model 44
4.2.5. Finite Element Simulations 44
4.2.6. Dimensionless Parameters 45
4.3. Results and Discussion 45
4.4. Conclusions 54
Chapter 5 *A cohesive-zone-based contact mechanics analysis of delamination in homogeneous and layered half-spaces subjected to normal and shear surface tractions* 55
5.1. Introduction 55
5.2. Modeling Approach 57
5.2.1. Finite Element Model 57
5.2.2. Cohesive Zone Model and Interfacial Delamination 58
5.2.3. Constitutive Model 61
5.2.4. Dimensionless parameters 61
5.3. Results and Discussion 62
5.3.1. Delamination in Homogeneous Half-Spaces 62
5.3.2. Delamination in Layered Half-Spaces 65
5.4. Conclusions 72
Chapter 6 *Conclusions* 74
Bibliography 77

List of Figures

Figure 2.1 Finite element mesh of a substrate in contact with a flat surface.

Figure 2.2 Comparison of analytical (Hertz) and FEM solutions of the contact pressure distribution along the plane of symmetry ($x = 0$) for an elastic substrate compressed by a rigid flat punch.

Figure 2.3 Finite element mesh of a substrate in contact with a patterned surface.

Figure 2.4 Dimensionless strain and stress results for an elastic-plastic substrate indented by a rigid flat surface ($\theta = 90^o$, $\bar{d} = 0.25$, and $\mu = 0.1$): (a) equivalent plastic strain $\bar{\varepsilon}^p_{eq}$; (b) von Mises equivalent stress $\bar{\sigma}_{eq}$, and (c) residual von Mises equivalent stress $\bar{\sigma}_{eq}$ after full unloading.

Figure 2.5 Dimensionless normal force $\bar{P}$ versus dimensionless normal displacement $\bar{d}$ for an elastic-plastic substrate indented by a rigid flat surface ($\theta = 60^o$, 75^o, and 90^o and $\mu = 0.1$).

Figure 2.6 Distribution of dimensionless von Mises equivalent stress $\bar{\sigma}_{eq}$ in the plane of symmetry ($x = 0$) for an elastic-plastic substrate indented by a rigid patterned surface ($\theta = 90^o$, $\bar{s} = 1.0$, and $\mu = 0.1$): (a) $\bar{d} = 0.56$, (b) $\bar{d} = 1.06$, (c) $\bar{d} = 1.50$, and (d) $\bar{d} = 0$ (fully unloaded).

Figure 2.7 Distribution of dimensionless equivalent plastic strain $\bar{\varepsilon}^p_{eq}$ for $\bar{d} = 1.50$ (a) at the plane of symmetry ($x = 0$) and (b) in isomeric view, and (c) dimensionless maximum equivalent plastic strain $\bar{\varepsilon}^p_{eq,max}$ versus dimensionless normal displacement $\bar{d}$ for an elastic-plastic substrate indented by a rigid patterned surface ($\theta = 90^o$, $\bar{s} = 1.0$, and $\mu = 0.1$).

Figure 2.8 Dimensionless elastic, plastic, and frictional work $\bar{W}_e$, $\bar{W}_p$, and $\bar{W}_f$, respectively, versus dimensionless normal displacement $\bar{d}$ for an elastic-plastic substrate indented by a rigid patterned surface ($\theta = 90^o$, $\bar{s} = 1.0$, and $\mu = 0.1$).

Figure 2.9 (a) Dimensionless normal force $\bar{P}$ and (b) cavity area ratio $\bar{a}$ versus dimensionless normal displacement $\bar{d}$ for an elastic-plastic substrate indented by a rigid patterned surface ($\theta = 90^o$, $\bar{s} = 1.0$, and $\mu = 0.1$, 0.4, and 0.7).

Figure 2.10 Distribution of dimensionless von Mises equivalent stress $\bar{\sigma}_{eq}$ in the plane of symmetry ($x = 0$) for an elastic-plastic substrate indented by a rigid patterned surface ($\theta = 90^o$ and $\mu = 0.1$): (a) $\bar{d} = 0.5$ and $\bar{s} = 0.5$, (b) $\bar{d} = 1.0$ and $\bar{s} = 0.5$, (c) $\bar{d} = 1.5$ and $\bar{s} = 0.5$, (d) $\bar{d} = 0.5$ and $\bar{s} = 1.0$, (e) $\bar{d} = 1.0$ and $\bar{s} = 1.0$, (f) $\bar{d} = 1.5$ and $\bar{s} = 1.0$, (g) $\bar{d} = 0.5$ and $\bar{s} = 1.5$, (h) $\bar{d} = 1.0$ and $\bar{s} = 1.5$, and (i) $\bar{d} = 1.5$ and $\bar{s} = 1.5$.

Figure 2.11 (a) Dimensionless normal force $\bar{P}$ and (b) cavity area ratio $\bar{a}$ versus dimensionless normal displacement $\bar{d}$ for an elastic-plastic substrate indented by a rigid patterned surface ($\theta = 90^o$, $\bar{s} = 0.5$, 1.0, and 1.5, and $\mu = 0.1$).

Figure 2.12 Dimensionless maximum equivalent plastic strain $\bar{\varepsilon}^p_{eq,max}$ versus dimensionless normal displacement $\bar{d}$ for an elastic-plastic substrate indented by a rigid flat or a rigid patterned surface ($\theta = 90^o$, $\bar{s} = 0.5, 1.0$, and 1.5, and $\mu = 0.1$).

Figure 3.1 (a) Cross-sectional schematic of a rigid cylinder loaded against a half-space and (b) refined finite element mesh at the near-surface region of the half-space.

Figure 3.2 Effective stress $\bar{\sigma}$ versus equivalent strain $\bar{\varepsilon}$ plot illustrating the evolution of material damage and degradation during deformation.

Figure 3.3 Evolution of damage parameter ω during the (a-c) first oscillation cycle and after the (d) first, (e) second, and (f) fifth oscillation cycles.

Figure 3.4 Dimensionless penetration depth $\bar{d}$ versus number of oscillation cycles N for $\bar{P} = 13 - 79$ and $\mu = 0.3$.

Figure 3.5 Dimensionless plastic area $\bar{A}_p$ versus number of cycles N for: (a) $\bar{P} = 13 - 79$ and $\mu = 0.3$ and (b) $\mu = 0.1 - 0.3$ and $\bar{P} = 33$.

Figure 3.6 Dimensionless wear area $\bar{A}_w$ versus number of oscillation cycles N for (a) for $\bar{P} = 13 - 79$ and $\mu = 0.3$ and (b) $\mu = 0.1 - 0.3$ and $\bar{P} = 33$.

Figure 3.7 Contours of plastic shear strain γ^p_{xy} after the first ($N = 1$), second ($N = 2$), and third ($N = 3$) oscillation cycles for $\bar{P} = 13$ (left column), $\bar{P} = 79$ (right column), and $\mu = 0.3$.

Figure 3.8 Averaged fraction of the contact area in slip mode $\bar{A}_s$ before the instigation of the removal of fully damaged elements versus load $\bar{P}$ for $\mu = 0.3$.

Figure 4.1 Contact model consisting of four regions with different finite element refinements.

Figure 4.2. Effective stress $\bar{\sigma}$ versus equivalent strain $\bar{\varepsilon}$ diagram illustrating the evolution of damage leading to material degradation.

Figure 4.3 Normalized von Mises equivalent stress $\bar{\sigma}_M$ (left) and equivalent plastic strain $\bar{\varepsilon}^p$ (right) for $D = 1.4$, $\bar{G} = 2.5 \times 10^{-7}$, and $\bar{P} = 14.2 \times 10^{-5}$ obtained after (a,b) normal loading ($N = 0$), (c,d) the first oscillation cycle ($N = 1$), and (e,f) the fifth oscillation cycle ($N = 5$). The $\bar{\varepsilon}^p$ contours are within the boxed areas shown on the left.

Figure 4.4 Normalized von Mises equivalent stress $\bar{\sigma}_M$ (left) and equivalent plastic strain $\bar{\varepsilon}^p$ (right) for $\bar{G} = 2.5 \times 10^{-7}$ and $\bar{P} = 14.2 \times 10^{-5}$ obtained after normal loading ($N = 0$): (a,b) $D = 1.3$, (c,d) $D = 1.4$, and (e,f) $D = 1.5$. The $\bar{\varepsilon}^p$ contours are within the boxed areas shown on the left.

Figure 4.5 Normalized von Mises equivalent stress $\bar{\sigma}_M$ (left) and equivalent plastic strain $\bar{\varepsilon}^p$ (right) for $\bar{G} = 2.5 \times 10^{-7}$ and $\bar{P} = 14.2 \times 10^{-5}$ obtained after five oscillation cycles ($N = 5$): (a,b) $D = 1.3$, (c,d) $D = 1.4$, and (e,f) $D = 1.5$. The $\bar{\varepsilon}^p$ contours are within the boxed areas shown on the left.

Figure 4.6 Material removal rate $\bar{A}_r$ versus normal load $\bar{P}$ for various values of $\bar{G}$ and (a) $D = 1.3$, (b) $D = 1.4$, and (c) $D = 1.5$.

Figure 4.7 Normalized von Mises equivalent stress $\bar{\sigma}_M$ at the end of normal loading for various normal loads $\bar{P}$, $D = 1.4$, and $\bar{G} = 2.5 \times 10^{-7}$. Corresponding magnified stress distributions inside the boxed areas 1 and 2 shown on the left are displayed in the middle and right column, respectively.

Figure 4.8 Normalized plastic work $\bar{W}_p$, frictional work $\bar{W}_f$, and elastic work $\bar{W}_e$ versus oscillation cycles N and normal load $\bar{P}$ for $D = 1.3$ and $\bar{G} = 2.5 \times 10^{-7}$. The normalized material removal rate $\bar{A}_r$ computed for the maximum cycle number is also shown for each simulation case.

Figure 4.9 Normalized plastic work $\bar{W}_p$, frictional work $\bar{W}_f$, and elastic work $\bar{W}_e$ versus oscillation cycles N and normal load $\bar{P}$ for $D = 1.4$ and $\bar{G} = 2.5 \times 10^{-7}$. The normalized material removal rate $\bar{A}_r$ computed for the maximum cycle number is also shown for each simulation case.

Figure 4.10 Normalized maximum penetration depth $\bar{d}_{\max}$ averaged over the total accumulated oscillation cycles of each simulation versus normal load $\bar{P}$ for $\bar{G} = 2.5 \times 10^{-7}$ and (a) $D = 1.3$, (b) $D = 1.4$, and (c) $D = 1.5$.

Figure 5.1 Finite element mesh (top) and refined mesh adjacent to the contact interface (bottom) (The yellow dashed line corresponds to the delamination interface and the layer/substrate interface.)

Figure 5.2 The cohesive model of the effective traction $\bar{\sigma}$ versus effective separation $\bar{\delta}$ at the delamination interface.

Figure 5.3 Effective nodal separation $\bar{\delta}$ profiles at the delamination interface ($\bar{h} = 1$) obtained (—) before and (—) after unloading versus distance *x/w* measured from the center of initial contact (*x/w* = 0) for a homogeneous elastic-plastic half-space with $E = 100$ GPa, $Y = 200$ MPa, and $\sigma_c = 100$ MPa: (a) $\bar{s} = 0.1$, $\bar{d} = 0.002$, (b) $\bar{s} = 0.3$, $\bar{d} = 0.002$, and (c) $\bar{s} = 0.1$, $\bar{d} = 0.0025$.

Figure 5.4 Delamination fraction α after unloading versus sliding distance $\bar{s}$ for a homogeneous elastic-plastic half-space with $E = 100$ GPa, Y = 200 MPa, $\bar{d} = 0.002$, 0.0025, and $\sigma_c = 75-125$ MPa.

Figure 5.5 Contours of the equivalent von Mises stress σ_{eq} for a homogeneous elastic-plastic half-space with $E = 100$ GPa, $Y = 200$ MPa, and $\sigma_c = 100$ MPa at three sequential simulation stages: (a) indentation ($\bar{d}$ = 0.002), (b) sliding ($\bar{s}$ = 0.3, $\bar{d}$ = 0.002), and (c) unloading. (The horizontal black line corresponds to the delamination interface.)

Figure 5.6 Delamination ratio β after unloading versus elastic modulus ratio $\bar{E}$ for an elastic layered half-space with $E_s = 85-200$ GPa and $\sigma_c = 100$ MPa ($\bar{h}$ = 0.1, $\bar{d}$ = 0.002, and $\bar{s}$ = 0.1).

Figure 5.7. Contours of the equivalent von Mises stress σ_{eq} versus elastic modulus ratio $\bar{E}$ and delamination fraction α obtained before unloading for an elastic layered half-space with (a)–(c) $E_s = 100$ GPa and $E_l = 100, 200$, and 300 GPa ($\bar{E}$ = 1, 2, and 3, respectively), (d)–(f) E_l = 200 GPa and E_s = 100, 150, and 200 GPa ($\bar{E}$ = 2, 1.33, and 1, respectively), and $\sigma_c = 100$ MPa ($\bar{h}$ = 0.1, $\bar{d}$ = 0.002, and $\bar{s}$ = 0.1). (The horizontal black line corresponds to the delamination interface.)

Figure 5.8 Delamination fraction a after unloading versus yield strength ratio $\bar{Y}$ for an elastic-plastic layered half-space with $E_l = E_s = 100$ GPa ($\bar{E} = 1$), Y_s = 50–300 MPa, and $\sigma_c = 100$ MPa ($\bar{h}$ = 0.1, $\bar{d}$ = 0.0025, and $\bar{s}$ = 0.3).

Figure 5.9 Effective nodal separation $\bar{\delta}$ profiles at the delamination interface ($\bar{h}$ = 1) obtained (—) before and (—) after unloading versus distance x/w measured from the center of initial contact (x/w = 0) for a layered elastic-plastic half-space with $E_l = E_s = 100$ GPa ($\bar{E}$ = 1), $E_s =$ 200 MPa, (a) $Y_l = 150$ MPa ($\bar{Y} = 0.75$), (b) $Y_l = 300$ MPa ($\bar{Y}$ = 1.5), and $\sigma_c = 100$ MPa ($\bar{h}$ = 0.1, $\bar{d}$ = 0.0025, and $\bar{s}$ = 0.3).

Figure 5.10 Contours of the equivalent von Mises stress σ_{eq} before (left) and after (right) unloading versus yield strength ratio $\bar{Y}$ and delamination fraction α for an elastic-plastic layered half-space with $E_l = E_s = 100$ GPa ($\bar{E}$ = 1), $Y_s = 200$ MPa, $Y_l = 50, 150$, and 300 MPa ($\bar{Y} =$ 0.25, 0.75, and 1.5, respectively), and σ_c = 100 MPa ($\bar{h}$ = 0.1, $\bar{d}$ = 0.0025, and $\bar{s}$ = 0.3). (The horizontal black line corresponds to the delamination interface.)

Figure 5.11 Contours of the equivalent plastic strain ε_{eq}^{p} after unloading versus yield strength ratio $\bar{Y}$ and delamination fraction a for an elastic-plastic layered half-space with $E_l = E_s = 100$ GPa ($\bar{E}$ = 1), (a–c) $Y_s = 200$ MPa and $Y_l = 50, 150$, and 300 MPa ($\bar{Y}$ = 0.25, 0.75, and 1.5, respectively), (d–f) Y_l = 300 MPa and Y_s = 100, 200, and 300 MPa ($\bar{Y}$ = 3, 1.5, and 1, respectively), and σ_c = 100 MPa ($\bar{h}$ = 0.1, $\bar{d}$ = 0.0025, and $\bar{s}$ = 0.3). (The horizontal black line corresponds to the delamination interface.)

Figure 5.12 Effective nodal separation $\bar{\delta}$ profiles at the delamination interface ($\bar{h}$ = 1) obtained (—) before and (—) after unloading versus distance x/w measured from the center of initial contact (x/w = 0) for a layered elastic-plastic half-space with $E_l = E_s = 100$ GPa ($\bar{E}$ = 1), Y_l = 300 MPa, (a) Y_s = 100 MPa ($\bar{Y}$ = 3), (b) Y_s = 200 MPa ($\bar{Y} = 1.5$), (c) Y_s = 300 MPa ($\bar{Y}$ = 1), and σ_c = 100 MPa ($\bar{h}$ = 0.1, $\bar{d}$ = 0.0025, and $\bar{s}$ = 0.3).

Figure 5.13 Contours of the equivalent von Mises stress σ_{eq} before (left) and after (right) unloading versus yield strength ratio $\bar{Y}$ and delamination fraction a for an elastic-plastic layered half-space with $E_l = E_s = 100$ GPa ($\bar{E}$ = 1), Y_s = 300 MPa, Y_s = 100, 200, and 300 MPa ($\bar{Y}$ = 3, 1.5, and 1, respectively), and σ_c = 100 MPa ($\bar{h}$ = 0.1, $\bar{d}$ = 0.0025, and $\bar{s}$ = 0.3). (The horizontal black line corresponds to the delamination interface.)

Figure 5.14 Delamination fraction α after unloading versus delamination layer thickness $\bar{h}$ for an elastic-plastic layered half-space with $E_l = E_s = 100$ GPa ($\bar{E}$ = 1), Y_s = 200 MPa, Y_l = 100–400 MPa ($\bar{Y}$ = 0.5–2, respectively) and σ_c = 100 MPa ($\bar{d} = 0.002$, $\bar{s} = 0.2$).

List of Tables

Table 2.1 Geometrical parameters and coefficient of friction used in the FEM simulations.

Table 2.2 Mechanical properties of the substrate material.

Table 3.1 Input parameters of the FEM simulations.

Table 3.2 Material properties and damage parameters used in the FEM simulations.

Table 4.1 Input parameters of the fractal surface.

Table 4.2 Material properties and damage parameters used in the FEM simulations.

Acknowledgements

The graduate school journey has been a cornucopia of opportunities and rewards, enriching my life in myriad ways. Foremost, I extend my heartfelt gratitude to my adviser and dissertation chair, Professor Kyriakos Komvopoulos. His unwavering support, guidance, and encouragement in my graduate research as well as his empathy and caring for me during difficult times, such as my grandmother's illness, have been invaluable. His advice to "look for a greater purpose in life" has become a guiding principle for me. I am deeply influenced by his meticulous approach to research and his emphasis on critical thinking, traits that have shaped me profoundly.

I am also grateful to my dissertation committee members, Professor Peter Hosemann and Professor Grace Gu, for their valuable comments and suggestions to this dissertation. Additionally, I would like to appreciate the contributions of my qualifying exam committee members, Professor Tarek Zohdi, Professor Kris Pister and Professor Peter Hosemann, whose candid comments and recommendations have enhanced my research and knowledge as a Ph.D. candidate.

My sincere thanks extend to my friends and colleagues, Dr. Shengxi Wang, Dr. Behnoosh Baboukani, Dr. Anurag Roy, Dr. Maria Molina, Dr. Alexandros Spyromilios, Dr. Zhichao Song, Dr. Steven Volkman, Dr. Chi Chung Li, Dr. Brian Salazar, Dr. Hossein Heidari, Dr. Brett Kelly, Dr. Hannah Gramling, for their kind support, friendship, and invaluable advice. Their help during the challenging times on the journey was of paramount importance.

I am profoundly grateful to my wife, Siyao Pang, whose unconditional love and encouragement have been my pillars of strength. Her steadfast belief in my dreams and her never-give-up spirit have sustained me through the rigors of graduate school.

Finally, I express my deep appreciation to my parents and grandparents for their encouragement and sacrifices, and for my uncle and aunt for their generosity in renting out an affordable studio (garage) to me in the highly expensive San Francisco Bay Area.

CHAPTER 1

Introduction

Contact mechanics is an important branch of solid mechanics dealing with the deformation behavior of solid bodies experiencing surface-to-surface interactions under the influence of external loads (i.e. friction) and/or internal loads (i.e. gravity). Various contact mechanics approaches have been used to analyze and tune design performance for a wide range of applications involving mechanical systems with contact elements, including (but not limited to) electromechanical relays and sensors, artificial knee and hip implants where the femoral head and polymer liner are in direct contact under the applied normal and sliding load, hard-disk drives where data storage reliability can be greatly affected by microscopic surface damage due to intermittent microscopic contacts at the head-disk interface, high-power gas turbines whose efficiency and longevity are affected by fretting wear, such as that due to shroud and snubber contact with the turbine blade, and various surface measurement techniques where direct contact of a probe is used, such as surface profilometry and atomic force microscopy (AFM).

Early analysis of contact systems was mainly focused on elastic material behavior. Hertz (1882) demonstrated an ellipsoidal distribution of contact pressure resulting in elastic displacement and elliptical contact area in two elastic solids. However, the Hertzian contact theory was quite limited to perfectly elastic materials and frictionless contact conditions. Intensive efforts to analyze stick-slip, friction, and plasticity in various contact problems were encountered during the past 100 years or so. Small-amplitude reciprocating sliding is called fretting. This process affects the performance of many contact-mode mechanical elements, endangering functionality and durability. Cattaneo (1938) and Mindlin (1949) pioneered the first contact analyses of elastic bodies subjected to both normal and tangential loads and showed a deviation of the deformation from that predicted by Hertz theory. Later, stick-slip phenomenon, comprising a circular stick zone surrounded by an annulus slip zone in elastic contacts, was investigated by Mindlin and Deresiewcz (1953), and fretting maps in which the fretting process was partitioned into stick regime, mixed stick-slip regime and gross slip regime were presented by Vingsbo and Söderberg (1988). In addition to friction due to adhesion in elastic contacts subjected to light loads, Komvopoulos et al. (1986) obtained an analytical expression for plowing friction to account for high normal load and full plastic deformation of a rigid sphere sliding over a rigid perfectly plastic half-space.

The early surface contact studies established the field of contact mechanics and motivated the investigation of challenging contact problems. In recent years, the advancement of computational capabilities in conjunction with powerful numerical methods, such as the finite element method (FEM), impelled the analysis of more complex elastic-plastic contact problems. For example, Komvopoulos and Choi (1992) performed an FEM analysis of multi-asperity elastic microcontacts, which elucidated the interaction of the stress/strain fields of neighboring asperities, and Riccardi and Montanari (2004) used the FEM to analyze the indentation of an elastic-perfectly plastic substrate by a rigid flat cylindrical punch and predicted the high stresses and plastic strains arising at the contact edge. Failure of materials can occur via different mechanisms, such as excessive plasticity leading to the removal of material (wear) and interfacial delamination in layered media. The loss of material in the form of wear debris may result from various mechanical processes, such as surface scratching (Elwasli et al., 2015) and strong adhesion at the contact interface (Zhang and Etsion, 2021). Interfacial delamination may occur even in an initially uniform

material after strain hardening of its near surface region due to the applied surface tractions. FEM modeling with incorporated a cohesive zone model (CZM) has been used to study interfacial delamination in a coated substrate subjected to indentation loading (Liu and Yang 2012) and interlaminar/intralaminar delamination in a laminated composite under impact loading (Soroush et al., 2018).

The main objective of this dissertation was to develop a computational framework for modeling contact mechanics problems of elastic-plastic half-spaces in contact with nominally smooth rigid surfaces or surfaces exhibiting multi-scale roughness (fractal behavior) under the effects of normal (indentation) and tangential (friction) loadings. Specifically, plasticity evolution leading to damage accrual and eventual material removal and its relationship with other physical parameters were elucidated with the incorporation of plasticity-based material damage models. Additionally, the implementation of CZM modeling into FEM analysis provided an effective computational approach for investigating how delamination commences in elastic and elastic-plastic materials.

This dissertation is organized into six chapters as follows.

Chapter 2 presents a quasi-static plane-strain FEM analysis that sheds light into the evolution of plasticity in an elastic-plastic strain-hardening half-space indented by a rigid flat or patterned surface. Since the element size was the determining factor for accurate contact pressure distribution and normal load at the given vertical displacement, a mesh refinement study was first carried out for a rigid flat indenting an elastic half-space. The resulting contact pressure distribution is compared against an analytical solution to ensure the adequacy of the mesh. A parametric study was conducted for incremental vertical displacements and the resulting stress and plastic strain fields in conjunction with the evolution of the normal force for flat and patterned surfaces were examined. The effects of geometric factors, such as side wall angle in the flat surface and protrusion spacing and cavity filling in the patterned surface, and the coefficient of friction on the normal force response and the development of stress and strain fields are interpreted in the context of numerical results. Since the high plasticity regions could likely lead to material failure, a constitutive model accounting for material damage leading to the removal of material was introduced in the FEM model.

Chapter 3 provides a quasi-static plane-strain FEM analysis that elucidates the evolution of plasticity and material removal in an elastic-plastic half-space due to reciprocating sliding against a rigid surface. The strain hardening material was used and a plasticity-based ductile damage model was incorporated into the constitutive model to simulate the material loss by removing the fully damaged element. A dimensionless plastic-strain-based damage parameter was used for tracking damage accumulation in the elements. Once this damage parameter reached unity in an element, a linear stiffness degradation process was instigated, which was controlled by a dimensionless degradation parameter that increased from 0 to 1, at which juncture, the element was removed from the finite element mesh. Results are presented to elaborate the effects of normal load, oscillation cycles, and coefficient of friction on the penetration depth, development of plasticity, removal of material, and plastic and wear areas. The wear area is shown to exhibit a nonlinear dependence on normal load, in contrast to Archard's classic wear law, which is explained by considering the evolution of plastic shear strain under low- and high-load oscillation conditions.

Chapter 4 encompasses a quasi-static plane-strain FEM analysis of the fretting process for the case of an elastic-plastic half-space in contact with a rough rigid surface exhibiting fractal behavior. The analysis is based on the same constitutive models for strain hardening, material damage, and material degradation used in Chapter 3. Fractal geometry possesses scale-invariant properties, such as continuity, non-differentiability, and self-affinity, which are related to the intrinsic physical laws that govern the generation of surfaces. Fractal geometry was introduced by Mandelbrot (1967) to describe the irregularity and disorder of objects and was later implemented in contact mechanics studies to describe the topography of contact surfaces (Majumdar and Bhushan, 1990, 1991; Wang and Komvopoulos, 1994a, 1994b, 1995; Komvopoulos, 2020). The effects of fractal parameters, applied normal load, and oscillation cycles on the development of subsurface stresses and plastic strains are discussed in the light of numerical results obtained in dimensionless form. The material removal rate demonstrated a nonlinear dependence on normal load, in contradiction with Archard's classical wear law, attributed to the effects of surface conformity and mechanical interlocking of the fractal surface with strain hardened material, leading to the decrease of the loss of material.

Chapter 5 is dedicated to material failure due to interfacial delamination in homogeneous and layered elastic-plastic half-spaces exposed to the normal and tangential tractions applied by a rigid surface. A surface-based CZM is implemented in a quasi-static FEM analysis to simulate nodal separation at the delamination interface when the prescribed fracture energy dependent separation condition is satisfied. The effects of indentation depth, sliding distance, and cohesive strength between the layer and the half-space on the delamination process are first examined for the case of a homogeneous half-space to establish a basis for reference. The effects of material property mismatch on the evolution of delamination in an elastic layered half-spaces is examined next. It is shown that stress intensification in the surface layer is a key factor in promoting interfacial delamination. A nonlinear increase of the delaminated interfacial area with increasing layer-to-substrate yield strength ratio is predicted, which is explained by the evolution of the stress field in the layer. In addition, a relationship between the layer thickness and interfacial delamination area is obtained for various yield strength ratios.

Chapter 6 includes the conclusions of the dissertation accompanied by a summary of the main findings of each chapter and an outline of potential future studies based on the computational models developed in this work.

CHAPTER 2

On the mechanics of metal imprinting by nominally flat and patterned rigid surfaces

2.1. Introduction

Engraving a surface pattern on a solid body is of particular significance in several engineering and biotechnology fields, optoelectronics, haptic technology, arts, and cosmetics. One of the most common engraving processes is imprinting, also referred to as stamping when a sheet metal is forced into a rigid cavity. In this process, a rigid tool (template) is pressed against a soft substrate, causing it to plastically deform and attain a desired surface topology. Recent advances in tool patterning methods, such as lithography and chemical etching, have created opportunities for imprinting patterns of various length scales on metallic substrates, thereby modifying their surface properties and functionality. For example, the optical, friction, and gripping characteristics of a metal surface can be altered by stamping surface patterns exhibiting hierarchical architectures. It is theorized that exceptional surface properties can be obtained through functional adaptation of the surface structure at all length levels of hierarchy. However, multi-level patterning of metal surfaces by imprinting requires thorough insight into the effects of key process parameters (e.g., pattern geometry and applied pressure) and the deformation behavior of the imprinted material on the process efficacy. Accordingly, to accomplish this objective, it is necessary to illuminate the basic mechanics of metal imprinting.

One of the commonly used methods to alter the macroscopic shape of metallic parts is metal stamping (Lim et al., 2014). The high utility of this process has motivated numerous computational studies, mainly based on the finite element method (FEM), for elucidating the intricacies of the metal stamping process. For instance, Wang and Budiansky (1978) used an FEM model to analyze sheet metal stamping by arbitrarily shaped punches and found fair agreement between numerical and experimental results for hemispherical punch stretching. Oh (1982) proposed a rigid-viscoplastic FEM formulation for metal forming analysis, while Chandra (1986) introduced an elastic-viscoplastic FEM analysis for problems involving large strains and investigated frictional effects at the punch and die interfaces on the process characteristics. Ghosh and Kikuchi (1988) presented a thermomechanical FEM analysis of sheet metal forming that uses a time-dependent elastic-viscoplastic constitutive law to model the metal flow behavior at elevated temperatures. Zimniak and Piela (2000) performed thermomechanical FEM simulations of the cup stamping process by a square punch and observed good agreement with experimental findings. Kim et al. (2001) proposed a sensitivity and optimization analysis for designing the die shape in metal stamping that is based on a Lagrangian formulation and reported excellent agreement with sensitivity results obtained with the finite difference method.

The use of a master surface (template) to controllably modify the microscale topology of a metal surface has been proven to be a potent technique in surface engineering (Xia and Lim, 2010). However, conversely to macroscale metal stamping, the majority of significant developments in micro/nanoscale stamping technologies, particularly imprinting, have been realized with polymeric materials. When a polymer is compressed by a hard patterned surface, the imposed deformation causes the polymer to gradually flow into the surface cavities and permanently acquire the topology imposed by the patterned surface after photo-induced curing (Traub et al., 2016). Pourdavoud et al. (2017) employed surface patterning to create nanofeatures on organo-metal

halide perovskites for photonic devices. Hirai et al. (2001, 2004) studied the effects of applied pressure and height-to-volume cavity ratio on nanoimprint lithography and reported high stress concentrations at the cavity corners and an increase of the pressure needed to completely fill the cavities with increasing height-to-width cavity ratio. Zhou and Komvopoulos (2005) examined the effect of loading rate on polymer imprinting and introduced a mechanistic model that explains the viscoplastic flow of a polymer into the pattern cavities. Shiotsu et al. (2014) employed a fracture mechanics approach to study the separation of a hard mask from an imprinted polymer surface during unloading and observed friction-induced stretching of the polymer in the cavities before the instigation of interface cracking at the cavity corners, followed by crack growth along the side wall up to the top of the cavity during the detachment of the mask.

Contrary to polymeric materials, basic understanding of metal imprinting at the microscale is relatively sparse and largely empirical. Aizawa et al. (2014) devised a surface patterning method for imprinting high aspect ratio microcavities on aluminum with a diamondlike carbon-coated die and examined the effects of friction and incremental normal loading on cavity depth. Choi et al. (2017) developed an imprinting method for direct metal-to-metal patterning that uses a master stamp engraved with square nickel micropillars to form submicron square cavities on electrochemically polished pure aluminum at room temperature. Yamamoto and Kuwabara (2008) developed a form rolling process for imprinting microgrooves onto metal surfaces and reported high pattern transcription quality. La et al. (2020) developed a metal-to-metal micro/nanoscale imprinting process that utilizes heat to augment the pattern transcription onto a metal substrate. In addition to experimental studies, numerical analyses have also performed to provide insight into the mechanics of the imprinting process at small scales. Riccardi and Montanari (2004) used an FEM model to analyze the indentation of an elastic-perfectly plastic material by a flat cylindrical rigid punch and observed the development of high stresses and plastic strains at the punch edge, a rapid stress decay with increasing distance from the contact edge, and the formation of plastic shear bands at 45^{o} from the surface plane. These investigators also examined the evolution of the plastic zone below the rigid indenter and the formation of a pile-up for a strain hardening material and the effect of friction on the normal force. Komvopoulos and Choi (1992) investigated the interaction of the stress fields generated in an elastic semi-infinite solid by a rigid surface consisting of an array of spherical protrusions and predicted a critical distance below which the effect of neighboring deformation becomes significant. In a series of contact mechanics studies of elastic-plastic patterned media, Gong and Komvopoulos (2004a, 2004b) examined the effect of the pattern geometry (meandered or sinusoidal) on the resulting deformation and stress fields and the propensity for crack initiation due to applied mechanical and thermal (friction) surface tractions. Xu et al. (2014) used the FEM to study the compression of isotropic hardening aluminum by a flat punch and reported the development of high stresses at the contact edge, extending into the substrate at 45^{o} from the surface normal.

The objective of the present study was to provide a comprehensive mechanics analysis of metal imprinting and obtain solutions of important process parameters in dimensionless form. Using a rigid, flat surface as the control geometry, the effects of surface pattern geometry (i.e., shape, size, and spacing of meandered surface protrusions), coefficient of friction, and penetration depth on the normal force, energy dissipation, and plastic flow behavior of an elastic-plastic substrate material exhibiting isotropic strain hardening were examined in the context of finite element simulations. The numerical results presented below illuminate the importance of the plastic flow behavior of the deformed material in metal imprinting and pave the way for further

extending this modeling work to examine other important effects, such as more complex pattern geometries, oscillatory movement at the template/substrate interface, frictional heating, substrate temperature, and other stress-stain constitutive laws.

2.2. Simulation Procedure

2.2.1. Finite element modeling

Figure 2.1 shows the quartered FEM model of a substrate ($w \times t \times l = 150 \times 300 \times 200$ μm) and a flat template ($a = b = c = 50$ μm) with vertical ($\theta = 90^{o}$) side walls. Due to symmetry, only a quarter of the contact geometry needs to be analyzed. The template edges are rounded off to a radius of curvature equal to 5 μm to prevent the excessive distortion of adjacent substrate elements during the deformation and also because ideally sharp corners are unrealistic. The nodes at the bottom boundary of the mesh ($z = -t$) are fully constrained, whereas the nodes at the left ($y = 0$) and right ($y = l$) boundaries are fixed in the y-direction. To account for the large strain gradients in the vicinity of the contact interface, the mesh adjacent to the template/substrate interface is refined with 2-μm-size elements. To enhance the computational efficiency, the near-surface mesh that does not come into contact with the template is refined with 4-μm-size elements, whereas the bulk of the substrate is meshed with 20-μm-size elements. The substrate is discretized by 100,700 8-node cubic elements with 109,080 nodes, of which 50% are allocated to the surface regions, whereas 5,942 10-node tetrahedral elements with 9,071 nodes are used to mesh the flat template.

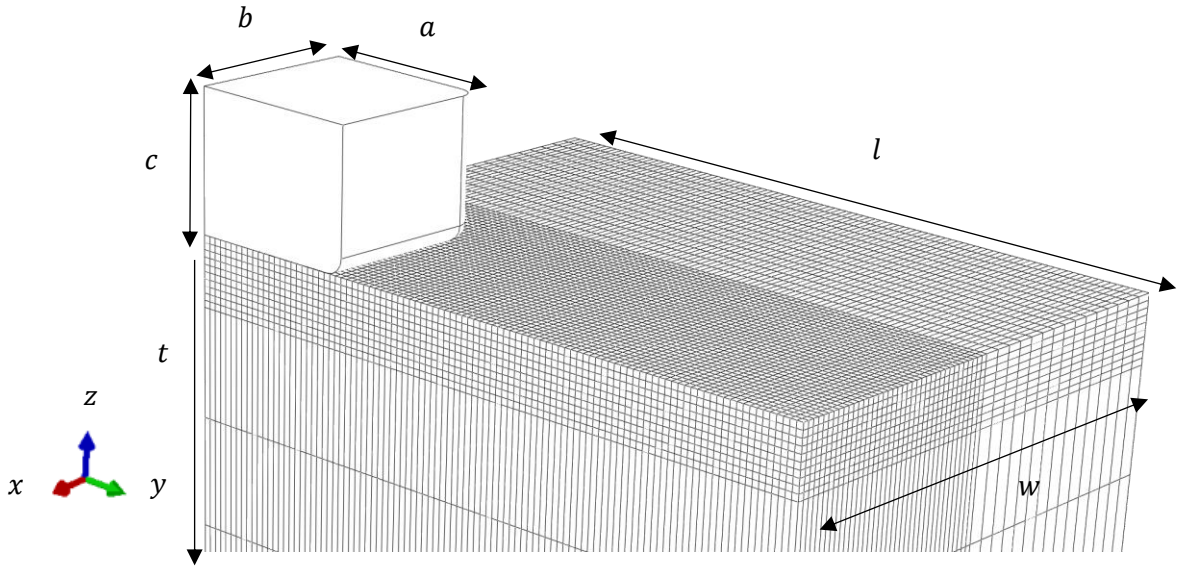

Figure 2.13 Finite element mesh of a substrate in contact with a flat surface.

Surface contact is simulated with a finite sliding algorithm that treats the deformable substrate and the rigid surface as slave and master surfaces, respectively, and controls the relative separation and slip between the interacting surfaces. When a slave node comes into contact anywhere along the master surface, it is constrained to slide along that surface by the algorithm, which tracks the position of the slave node relative to the master surface during contact

deformation. The finite sliding algorithm was implemented in the present FEM analysis by means of automatically generated contact elements. At each integration point of a contact element, the overclosure was adjusted to inhibit that point on the deforming surface to penetrate the rigid surface and the relative shear slip was computed afterwards.

To determine an appropriate mesh refinement, the plane-strain contact problem of a rigid flat punch in frictionless normal contact with an elastic half-space discretized by various mesh sizes was analyzed and numerical solutions of the contact pressure distribution were compared with the analytical solution given by (Johnson, 1985)

$$p(y) = \frac{P}{\pi a}\left[1 - \left(\frac{y}{a}\right)^2\right]^{-1/2} \quad , \tag{2.1}$$

where P is the normal force per unit length in the x-direction and y is the distance from the center of contact. Figure 2.2 shows a comparison between FEM results of the contact pressure distribution at $x = 0$ for refined meshes adjacent to the substrate surface with an element size equal to 2 and 4 μm and the analytical solution for $P = 0.1$ N/m and substrate elastic modulus and Poisson's ratio equal to 70 GPa and 0.35, respectively. The good agreement of the variation of the contact pressure with the dimensionless distance $\bar{y} = y/a$ obtained with the two FEM meshes and the theoretical solution validates the selection of a refined mesh with 2-μm-size elements and confirms the applicability of the modeling assumptions.

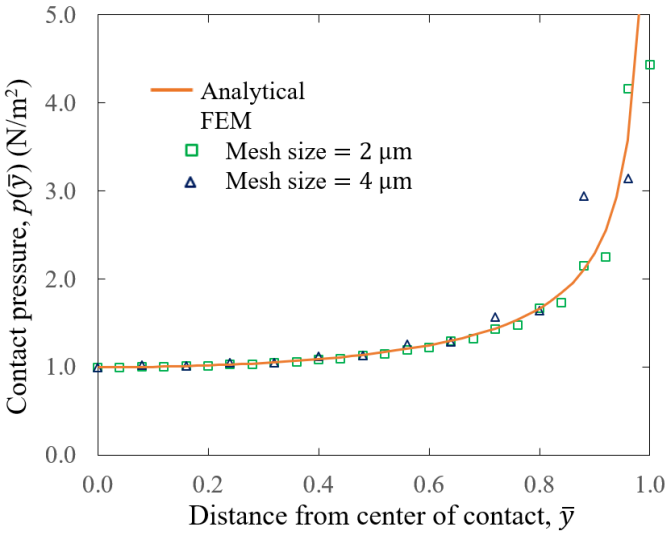

Figure 2.14 Comparison of analytical (Hertz) and FEM solutions of the contact pressure distribution along the plane of symmetry ($x = 0$) for an elastic substrate compressed by a rigid flat punch.

Figure 2.3 shows the FEM model of a patterned template b × c × l = 50 × 40 × 200 μm with protrusion edges rounded off to a radius of curvature equal to 5 μm in contact with the same substrate as that shown in Fig. 2.1. Because the $x = 0$ plane is a symmetry plane, only half of the contact geometry has to be modeled. Because the objective was to analyze the effect of neighboring protrusions on the deformation behavior, only a unit cell of the geometry is modeled, i.e., one protrusion between two half-width protrusions. The patterned template is meshed with ~20,000

10-node tetrahedral elements having 29,598 nodes. Likewise with the flat template/substrate model, the pure master-slave option is used to simulate surface contact. Similar to the previous FEM model, the nodes at the left ($y = 0$) and right ($y = l$) boundaries of the mesh are fixed in the y-direction, whereas the nodes at the bottom boundary of the mesh ($z = -t$) are fully constrained.

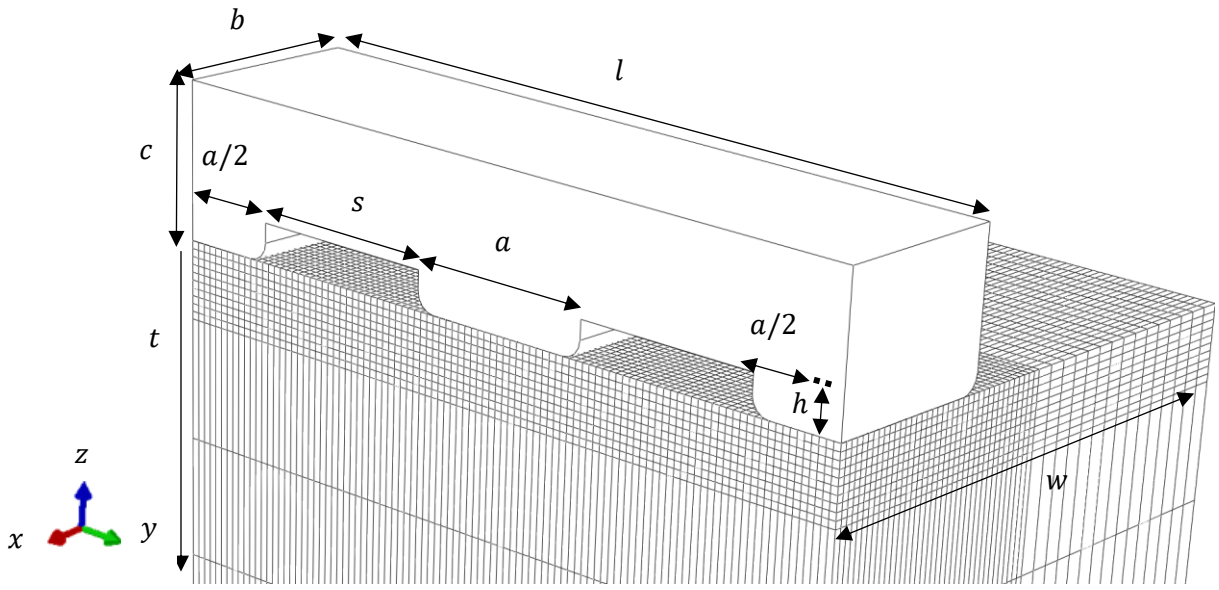

Figure 2.15 Finite element mesh of a substrate in contact with a patterned surface.

All FEM simulations were performed in displacement-control mode, i.e., the indenting rigid template was quasi-statically advanced towards the stationary substrate up to a maximum normal displacement $d = 10$ and 15 μm for the nominally flat and patterned templates in approximately 70 and 120 increments, respectively. Table 2.1 gives the magnitudes of geometric parameters and the coefficient of friction μ at the template/substrate contact interface used in the analysis. All of the FEM simulations were performed with the multi-physics code ABAQUS/Standard (implicit solver).

2.2.2. Elastic-plastic material behavior

The substrate is modelled as an isotropic strain hardening material obeying the following constitutive law:

$$\sigma = E\varepsilon \quad (\sigma < \sigma_Y) \tag{2.2a}$$

$$\sigma = K\varepsilon^n \quad (\sigma \geq \sigma_Y) \tag{2.2b}$$

where σ is the true stress, ε is the true strain, E is the elastic modulus, σ_Y is the yield strength, K is the strength coefficient, and n is the strain hardening exponent. The mechanical properties of the substrate given in Table 2.2 are typical of aluminum (Rashad et al., 2015). The strain hardening exponent n was assumed to be equal to the ultimate strain ε_u. Consequently, the strain hardening coefficient was computed in terms of the ultimate strength σ_u and corresponding ultimate strain ε_u by $K \approx \sigma_u/\varepsilon_u^n$.

Yielding is determined by the von Mises yield criterion, given by

$$\sigma_{\mathrm{eq}} = \left(\frac{3}{2} S_{ij} S_{ij}\right)^{1/2} = \sigma_Y \tag{3}$$

where σ_{eq} is the von Mises equivalent stress and S_{ij} are components of the deviatoric stress tensor.

The evolution of plasticity is traced by the equivalent plastic strain $\varepsilon_{\mathrm{eq}}^{p}$, given by

$$\varepsilon_{\mathrm{eq}}^{p} = \int_{\Omega} \left(\frac{2}{3} d\varepsilon_{ij}^{p} d\varepsilon_{ij}^{p}\right)^{1/2} \tag{4}$$

where Ω is the strain path used to track the accumulation of plasticity and $d\varepsilon_{ij}^{p}$ denotes plastic strain increments.

Table 2.1 Geometrical parameters and coefficient of friction used in the FEM simulations.

Indentation depth of flat surface, d	10 μm
Indentation depth of patterned surface, d	15 μm
Side wall angle, θ	$60°, 75°, 90°$
Protrusion distance, s	$25, 50, 75$ μm
Protrusion width, a	50 μm
Protrusion height, h	10 μm
Coefficient of friction, μ	$0.1, 0.5, 0.7$

Table 2.2 Mechanical properties of the substrate material.

Elastic modulus E (GPa)	Yield strength σ_Y (MPa)	Yield strain ε_Y	Poisson's ratio ν	Ultimate strength σ_u (MPa)
70	57	0.014	0.35	105
Ultimate strain ε_u	Strain hardening coefficient K (MPa)	Strain hardening exponent n	Fracture strain ε_f	
0.115	135	0.115	0.18	

2.2.3. Dimensionless parameters

To present general solutions, the input and output parameters of the analysis are normalized by appropriate quantities. Thus, the dimensionless von Mises equivalent stress and equivalent plastic strain are defined by $\bar{\sigma}_{\mathrm{eq}} = \sigma_{\mathrm{eq}}/\sigma_Y'$ and $\bar{\varepsilon}^p_{\mathrm{eq}} = \varepsilon^p_{\mathrm{eq}}/\varepsilon^p_{\max}$, where σ_Y' is the current yield strength (i.e., the stress at the current strain on the strain hardening curve) and $\varepsilon^p_{\max}$ is the maximum plastic strain at the current step. In addition, the dimensionless normal force and elastic, plastic, and friction energies are given by $\bar{P} = P/(A_a\sigma_Y')$, $\bar{W}_e = W_e/W$, $\bar{W}_p = W_p/W$, and $\bar{W}_f = W_f/W$, respectively, where A_a is the apparent contact area and W is the total work. Finally, the dimensionless normal displacement, protrusion spacing, maximum equivalent plastic strain, and fraction of cavity area (volume) filled by the substrate material are defined by $\bar{d} = d/a$ (flat surface) or d/h (patterned surface), $\bar{s} = s/a$, $\bar{\varepsilon}^p_{\mathrm{eq,max}} = \varepsilon^p_{\mathrm{eq,max}}/\varepsilon_f$, and $\bar{\alpha} = A_c'/A_c$, respectively, where ε_f is the fracture strain, A_c' is the cross-sectional cavity area filled by the deformed substrate material, and A_c is the apparent cross-sectional area of the cavity.

2.3. Results and discussion

2.3.1. Imprinting by a flat surface

Figure 2.4 shows isostress contours of the dimensionless equivalent plastic strain $\bar{\varepsilon}^p_{\mathrm{eq}}$ and von Mises equivalent stress $\bar{\sigma}_{\mathrm{eq}}$ before and after full unloading for $\theta = 90^{\mathrm{o}}$, $\bar{d} = 0.25$, and $\mu = 0.1$. The large plastic strains at the contact edge and especially the corners of the residual impression (Fig. 2.4(a)) are due to the high stress concentrations at these regions (Fig. 2.4(b)) that produce large stress and strain gradients at the perimeter of the impression. The development of high stresses at the contact edge and corners of the impression is consistent with the analytical and FEM results shown in Fig. 2.2. High stresses at the contact edge developed with the instigation of loading and spread into the substrate at 45° from the surface normal as the load was increased, consistent with other studies (Riccardi and Montanari, 2004; Xu et al., 2014), causing severe plastic shearing of the substrate material against the edge and side walls of the rigid template. When the template was withdrawn, the plastic zone around the impression inhibited the full release of the elastic strain energy accumulated in the surrounding elastic zone, resulting in high localized residual stresses at the edge and corners of the impression and material pile-up around the impression (Fig. 2.4(c)). High residual stresses can significantly affect the mechanical behavior of the imprinted material (Xing and Lu, 2004) and degrade the quality of the imprinted surface in subsequent material processing (e.g., deburring and planarization). The pile-up geometry is controlled by the plastic flow of material around the contact edge and against the side walls of the flat template.

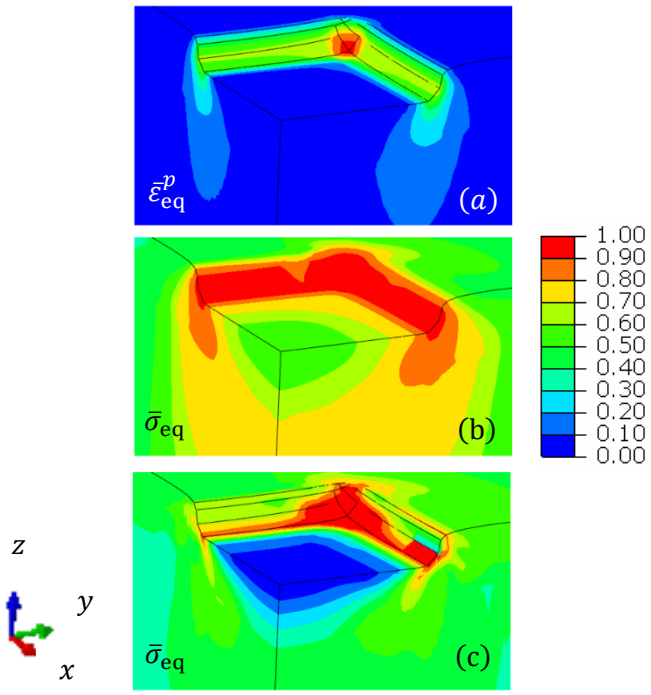

Figure 2.16 Dimensionless strain and stress results for an elastic-plastic substrate indented by a rigid flat surface ($\theta = 90^o$, $\bar{d} = 0.25$, and $\mu = 0.1$): (a) equivalent plastic strain $\bar{\varepsilon}^p_{eq}$; (b) von Mises equivalent stress $\bar{\sigma}_{eq}$, and (c) residual von Mises equivalent stress $\bar{\sigma}_{eq}$ after full unloading.

Figure 2.5 shows the variation of the dimensionless normal force $\bar{P}$ with the dimensionless normal displacement $\bar{d}$ and side wall angle θ for $\mu = 0.1$. The force response reveals a two-stage deformation behavior influenced by the plastic flow of material adjacent to the template surface and the side wall angle. The linear increase of the normal force in the first deformation stage is illustrative of the elastic behavior of the deformed substrate. In the second deformation stage, the contact force increases gradually with the progression of plasticity in the vicinity of the template front. The deformation in this stage is characterized by the flow of material first sideways and then upwards, resulting in plastic shearing against the template's edge and side walls and the formation of a pile-up. Thus, the force response in this deformation stage is predominantly controlled by plastic flow in the substrate and the template geometry. The latter effect is evidenced from the fact that the side wall angle affects the normal force only in the second deformation stage when the formation of a pile-up becomes pronounced. The increase of the normal force with decreasing side wall angle is attributed to the growth of the contact area due to the interaction of the pile-up material with the sloped side wall. The smaller the side wall angle, the larger the increase of the contact area due to the pile-up effect and, consequently, the higher the normal force to further deform the material. Because this effect was not observed with vertical side walls ($\theta = 90^{\text{o}}$), the normal force for $\theta = 90^{\text{o}}$ is solely due to the plastic flow of the material.

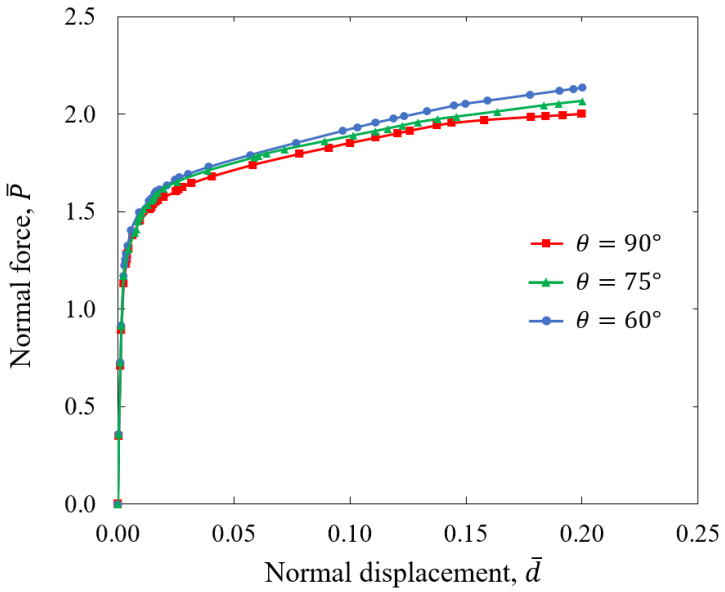

Figure 2.17 Dimensionless normal force $\bar{P}$ versus dimensionless normal displacement $\bar{d}$ for an elastic-plastic substrate indented by a rigid flat surface ($\theta = 60^o$, 75^o, and 90^o and $\mu = 0.1$).

2.3.2. Imprinting by a patterned template surface

Figure 2.6 shows isostress contours of the dimensionless von Mises equivalent stress $\bar{\sigma}_{\text{eq}}$ at the symmetry plane ($x = 0$) of the substrate due to surface imprinting by a patterned rigid template versus the dimensionless normal displacement $\bar{d}$ for $\theta = 90^{\text{o}}$, $\bar{s} = 1.0$, and $\mu = 0.1$. In the early stage of imprinting (Fig. 2.6(a)), the deformation below the protrusions of the patterned template is similar to that of the flat template (Fig. 2.4(b)), i.e., high stresses are localized at the protrusion edge and corners. However, as the imprinting process proceeds, the substrate material begins to flow into the cavities between the protrusions and the high stress pockets expand in the 45° direction below the contact surface (Fig. 2.6(b)), eventually joining each other to form a high stress band below each protrusion (Fig. 2.6(c)). After the patterned template is retracted, high residual stresses are produced in the near-surface region of the substrate just below the contact interface (Fig. 2.6(d)), in profound difference with the residual stress field generated by the flat template (Fig. 2.4(c)).

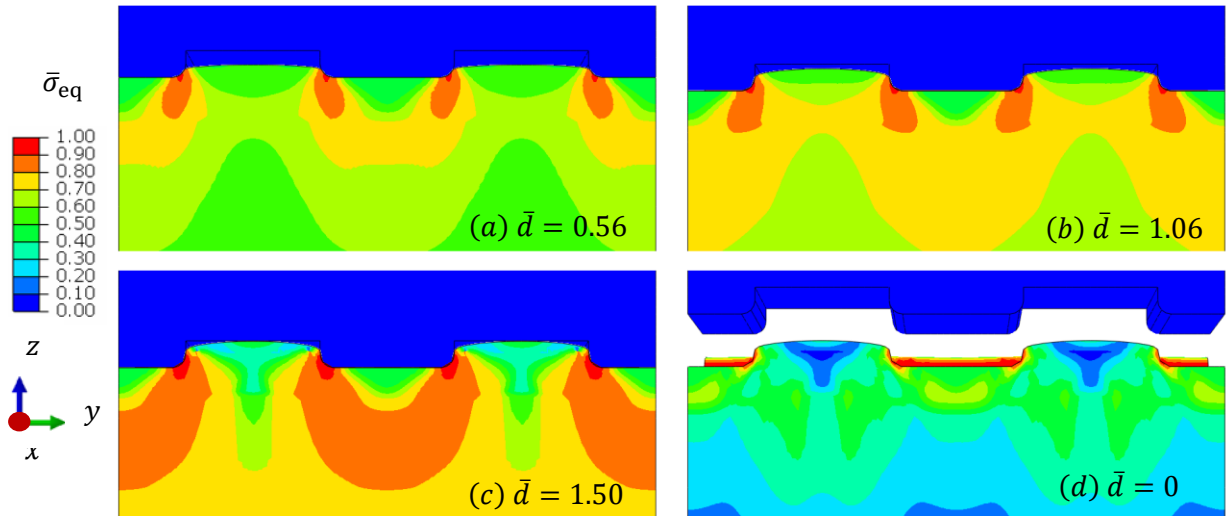

Figure 2.18 Distribution of dimensionless von Mises equivalent stress $\bar{\sigma}_{eq}$ in the plane of symmetry ($x = 0$) for an elastic-plastic substrate indented by a rigid patterned surface ($\theta = 90^o$, $\bar{s} = 1.0$, and $\mu = 0.1$): (a) $\bar{d} = 0.56$, (b) $\bar{d} = 1.06$, (c) $\bar{d} = 1.50$, and (d) $\bar{d} = 0$ (fully unloaded).

Further insight into the deformation induced by the patterned template surface can be obtained in the light of the distribution of the dimensionless equivalent plastic strain $\bar{\varepsilon}^p_{\text{eq}}$ at the symmetry plane ($x = 0$) of the substrate (Fig. 2.7(a)) and the isometric overview of the deformed substrate (Fig. 2.7(b)) for $\theta = 90^{\text{o}}$, $\bar{d} = 1.50$, $\bar{s} = 1.0$, and $\mu = 0.1$. Likewise with the flat template, the highest plastic strains are localized at the protrusion corners of the patterned template, where excessive plastic shearing occurs as the material is forced into the cavities (Fig. 2.7(b)). The foregoing deformation may lead to material transfer at those regions of excessive plastic shearing, contaminating the template surface and, consequently, degrading the imprinting quality. Figure 2.7(c) shows the variation of the dimensionless maximum equivalent plastic strain $\bar{\varepsilon}^p_{\text{eq,max}}$ with the dimensionless normal displacement $\bar{d}$ for flat and patterned template surfaces, $\theta = 90^{\text{o}}$, and $\mu = 0.1$. While the slope of the $\bar{\varepsilon}^p_{\text{eq,max}}$ curve of the patterned surface is initially larger than that of the flat surface, for a dimensionless normal displacement of the patterned surface $\bar{d} > 1.0$, the two curves exhibit equal slopes, implying similar deformation behavior. This trend is attributed to the progressive filling of the cavities, eventually leading to a patterned surface behavior similar to that of the flat surface. However, as shown in Fig. 2.7(a), complete filling of the cavities does not occur due to the existing geometric constraints and the plastic flow of the material, consistent with the findings of a previous study (Hirai et al., 2001). Nevertheless, it will be shown later that the fraction of unfilled cavity volume is small. Therefore, it may be inferred that for relatively large normal displacements the deformation behavior of the patterned template approximates that of the flat template.

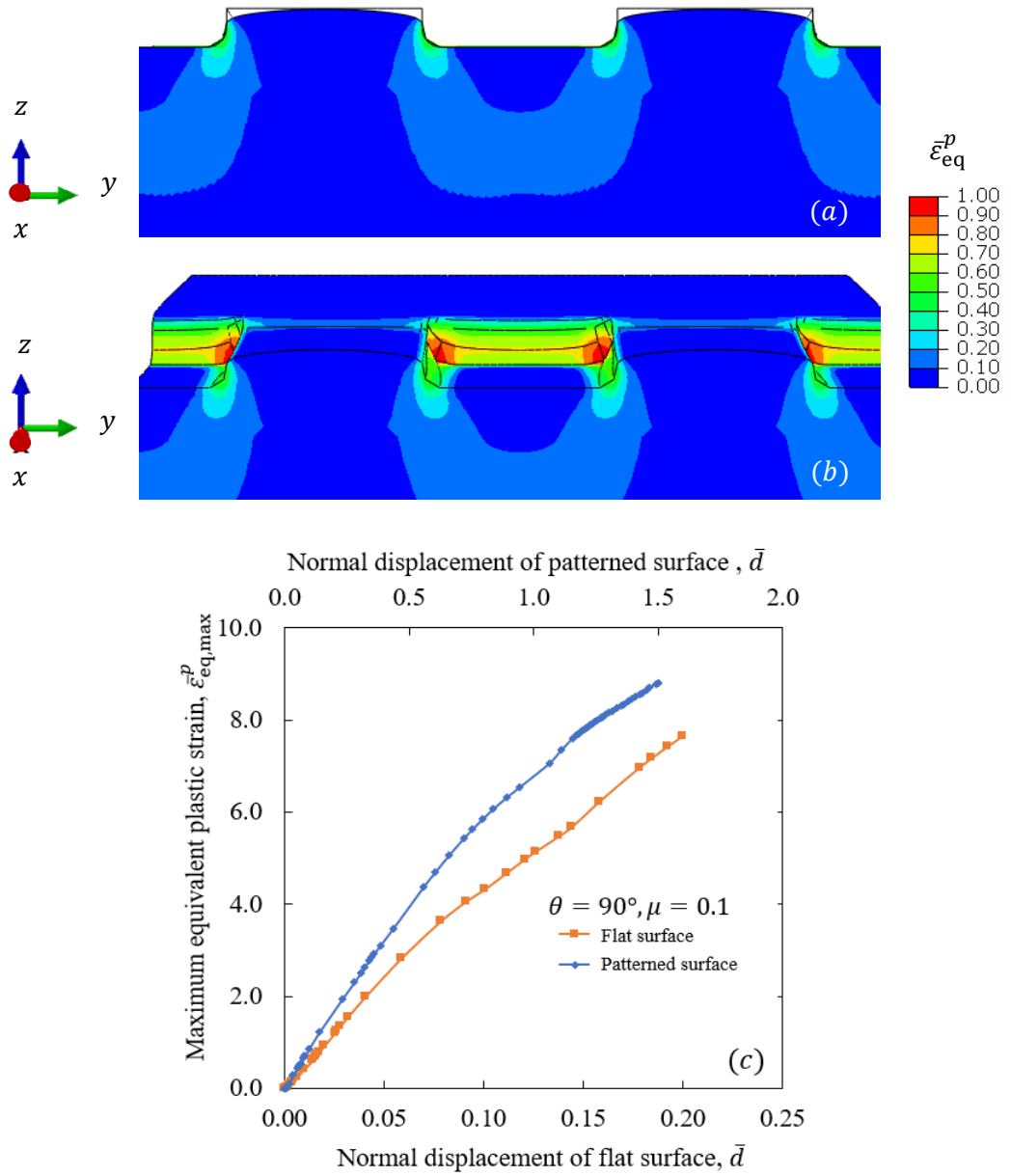

Figure 2.19 Distribution of dimensionless equivalent plastic strain $\bar{\varepsilon}^p_{eq}$ for $\bar{d} = 1.50$ (a) at the plane of symmetry ($x = 0$) and (b) in isomeric view, and (c) dimensionless maximum equivalent plastic strain $\bar{\varepsilon}^p_{eq,max}$ versus dimensionless normal displacement $\bar{d}$ for an elastic-plastic substrate indented by a rigid patterned surface ($\theta = 90^o$, $\bar{s} = 1.0$, and $\mu = 0.1$).

It is noted that the equivalent plastic strain contours shown in Figs. 2.4(a) and 2.7 reveal the development of large plastic strain gradients in the vicinities of the substrate adjacent to the corners of the rigid template, which act as stress raiser points. The constitutive laws used in conventional plasticity theory, such as that used in the present analysis, do not include size effects. In microscale plasticity, however, metallic materials that are nonuniformly deformed into the plastic regime may exhibit a strong size effect, whereby the smaller the size the stronger the

material response. This has led to the development of various theories of strain gradient plasticity, which employ an internal material length scale to account for size effects in microscale plastic deformation (Fleck and Hutchinson, 1993; Fleck et al., 1994; Abu Al-Rub and Voyiadjis, 2004; Chakravarthy and Curtin, 2011). The present analysis can be extended to include size effects encountered at micron and submicron scales in metal imprinting by implementing in the analysis a constitutive law in which the yield stress exhibits a dependence on both strain and strain gradient.

The deformation behavior of the patterned template surface can be further interpreted in terms of the energy characteristics of the problem at hand. Figure 2.8 shows the dimensionless elastic, plastic, and frictional work $\bar{W}_e$, $\bar{W}_p$, and $\bar{W}_f$, respectively, versus the dimensionless normal displacement $\bar{d}$ for $\theta = 90^o$, $\bar{s} = 1.0$, and $\mu = 0.1$. As expected, the dominant deformation mode during the initial stage of imprinting is elastic. However, a sharp transition from elastic to plastic dominated deformation commences at a very small normal displacement ($\bar{d} \approx 0.02$), beyond which the elastic and plastic works exhibit opposite trends. Thus, the elastic and plastic works demonstrate two-stage variation. The initial rapid increase of the plastic work is attributed to the accumulation of plasticity at the protrusion edges and corners, whereas the subsequent gradual increase is associated with the progressive filling of the cavities. In fact, the slope of the plastic work stabilizes at $\bar{d} \approx 0.8$, consistent with the constant slope of $\bar{\varepsilon}^p_{\text{eq,max}}$ for $\bar{d} \geq 1.0$ (Fig. 2.7(c)). The extremely low frictional work dissipation is due to the low coefficient of friction ($\mu = 0.1$) and indicates the dominance of plasticity in imprinting processes involving low-friction and/or well-lubricated template/substrate material systems demonstrating low adhesion (Komvopoulos, 2012). Another factor contributing to the very low frictional work is that relative slip at the template/substrate interface is mostly confined over a very small fraction of the contact area at the protrusion edges, partly due to the vertical side walls ($\theta = 90^o$), where localized excessive shearing guides the material into the cavities (Figs. 2.7(a) and 2.7(b)).

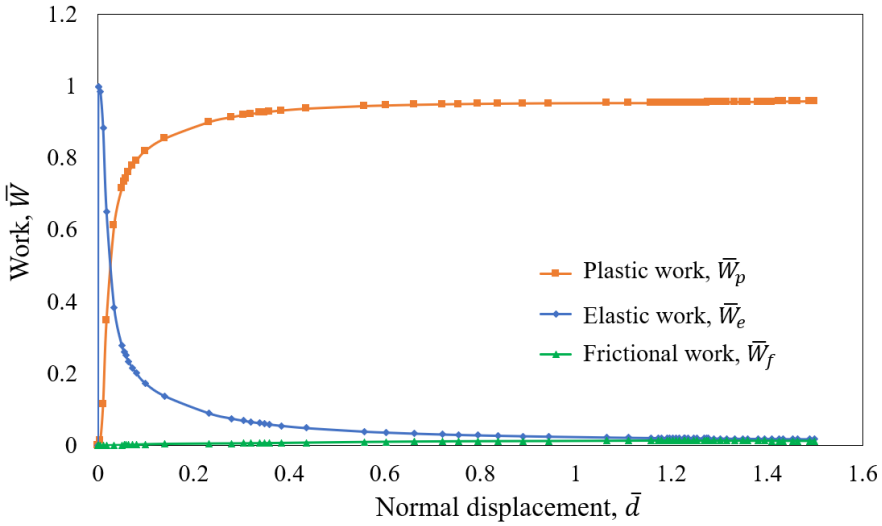

Figure 2.20 Dimensionless elastic, plastic, and frictional work $\bar{W}_e$, $\bar{W}_p$, and $\bar{W}_f$, respectively, versus dimensionless normal displacement $\bar{d}$ for an elastic-plastic substrate indented by a rigid patterned surface ($\theta = 90^o$, $\bar{s} = 1.0$, and $\mu = 0.1$).

Figure 2.9 illustrates the effect of the coefficient of friction on the imprinting behavior of a patterned template surface for $\theta = 90^{o}$ and $\bar{s} = 1.0$. The force-displacement response shown in Fig. 2.9(a) reveals several important trends. First, the normal force is marginally affected by the variation of the coefficient of friction. This seemingly counterintuitive effect can be explained by considering the effect of friction on the contact intimacy at the template/substrate interface. For a given normal displacement, the contact area decreases with the increase of coefficient of friction because friction impedes the plastic flow of material and, consequently, filling of the template cavities. This is evidenced from the fact that the friction effect becomes notable only in the second stage of the imprinting process where the cavities are significantly filled with plastically deformed material. Thus, the slightly higher normal force for lower coefficient of friction is attributed to the establishment of a relatively larger contact area (due to the effect of cavity filling), requiring a higher normal force to further advance the template into the substrate. A second important observation is that the force-displacement response demonstrates a profound change in both slope and linearity at $\bar{d} \approx 1.2$, implying a marked change in contact geometry, which is attributed to the substantial filling of the cavities. Indeed, as shown in Fig. 2.9(b), the cavity area ratio $\bar{a}$ increases above ~0.8 in the dimensionless normal displacement range $\bar{d} \geq 1.2$, with the rate of cavity filling and force slope both decreasing in this range. A third observation from Fig. 2.9(b) is that higher friction leads to less cavity filling, consistent with the indirect effect of the coefficient of friction on the normal force through the contact area discussed earlier. Evidently, as the contact area increases with the proliferation of cavity filling, a larger force is needed to push the template into the substrate. The gradual saturation of cavity filling is demonstrated by the progressively decreasing slope of the cavity area ratio with increasing normal displacement (Fig. 2.9(b)).

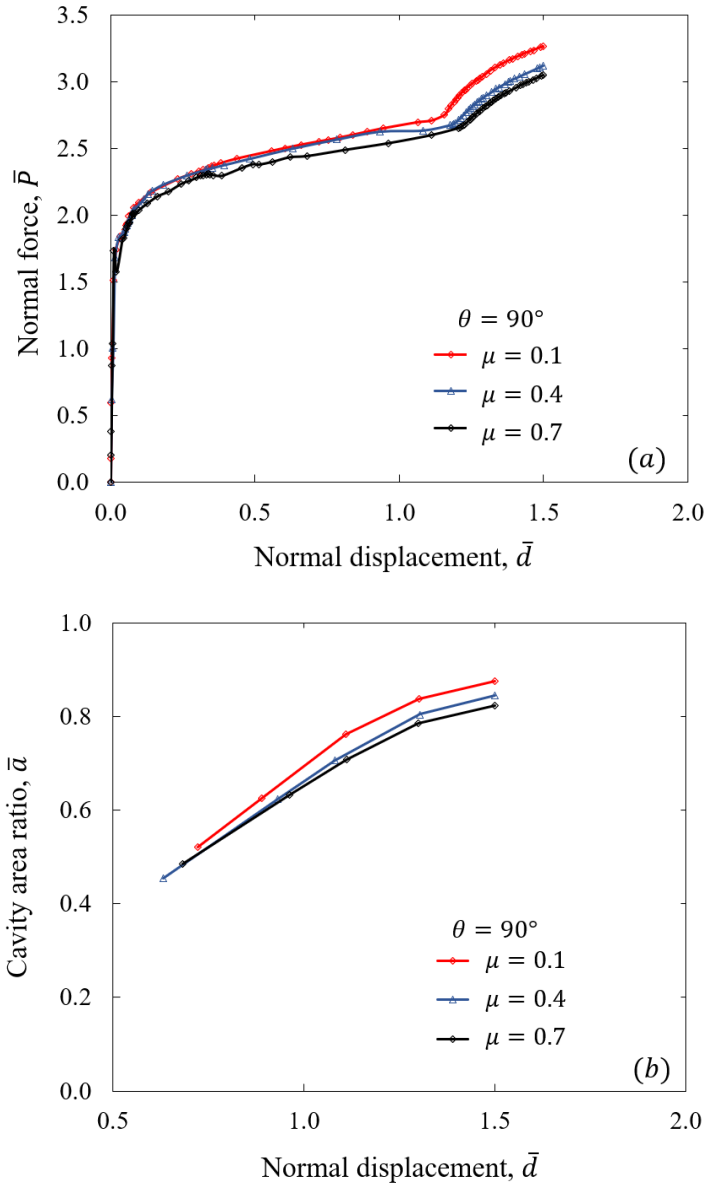

Figure 2.21 (a) Dimensionless normal force $\bar{P}$ and (b) cavity area ratio $\bar{a}$ versus dimensionless normal displacement $\bar{d}$ for an elastic-plastic substrate indented by a rigid patterned surface ($\theta = 90^o$, $\bar{s} = 1.0$, and $\mu = 0.1$, 0.4, and 0.7).

Another important factor of the imprinting process is the lateral distance of the pattern protrusions. Figure 2.10 shows isostress contours of the dimensionless von Mises equivalent stress $\bar{\sigma}_{\text{eq}}$ for $\bar{d} = 0.5 - 1.5$, $\bar{s} = 0.5 - 1.5$, $\theta = 90^o$, and $\mu = 0.1$. The results reveal stress intensification with increasing normal displacement and decreasing protrusion lateral distance due to the strengthening interaction of the stress fields of neighboring protrusions. Consequently, the highest stresses in the substrate arise for $\bar{d} = 1.5$ and $\bar{s} = 0.5$ (Fig. 2.10(c)). However, for relatively small normal displacement and large protrusion spacing, the neighboring deformation effect becomes secondary and the stress field below each protrusion resembles that of a flat punch. Since the foregoing situation is observed for $\bar{d} = 0.5$ and $\bar{s} = 1.5$ (Fig. 2.10(g)), it may be inferred that for patterned surfaces with protrusions spaced apart by distances of $\gtrsim$1.5 times the protrusion

width, the stress field below each protrusion is independent of the spatial distribution of the protrusions, consistent with the findings of another study (Komvopoulos and Choi, 1992). The interaction of the stress fields of neighboring protrusions can be further interpreted by considering the plastic flow of material flowing into the cavities. The protrusion distance controls the cavity volume and, in turn, the degree of cavity filling by plastically deformed material. Thus, for a small protrusion distance (e.g., $\bar{s} = 0.5$), the small cavity volume leads to premature filling, and the stress field remote from the template/substrate contact interface becomes uniform (Fig. 2.10(c)) similar to that of the flat surface.

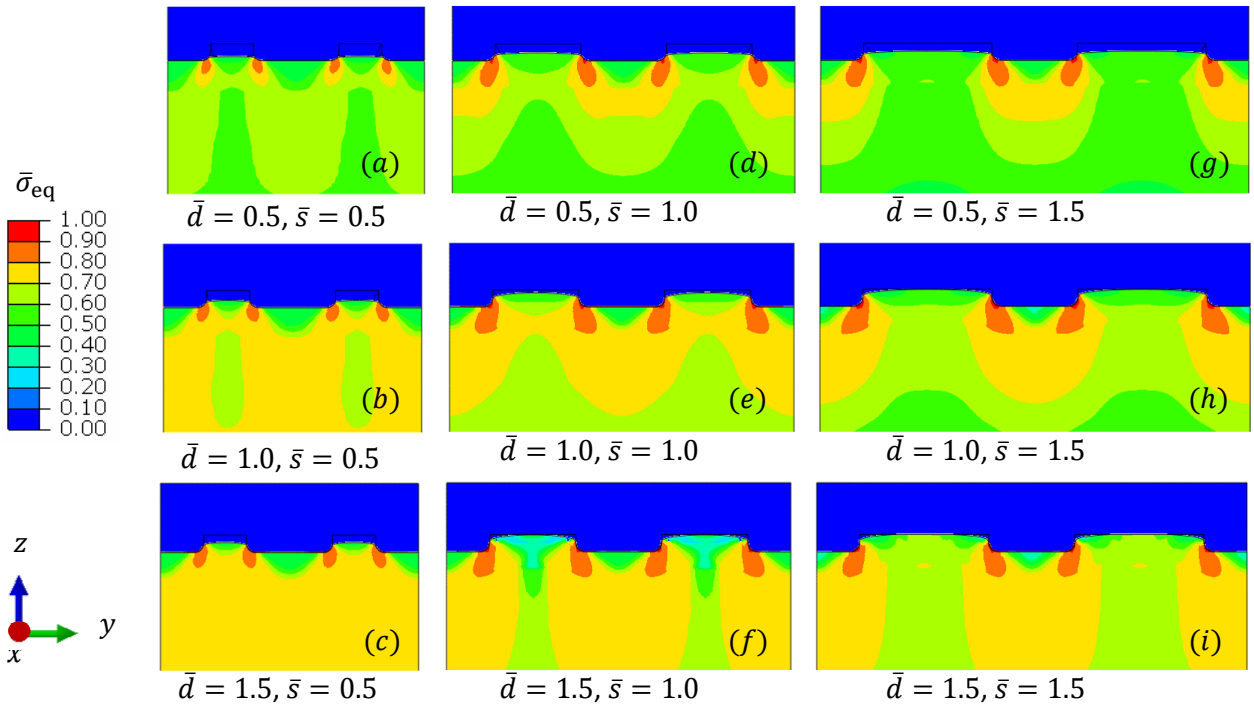

Figure 2.22 Distribution of dimensionless von Mises equivalent stress $\bar{\sigma}_{eq}$ in the plane of symmetry ($x = 0$) for an elastic-plastic substrate indented by a rigid patterned surface ($\theta = 90^o$ and $\mu = 0.1$): (a) $\bar{d} = 0.5$ and $\bar{s} = 0.5$, (b) $\bar{d} = 1.0$ and $\bar{s} = 0.5$, (c) $\bar{d} = 1.5$ and $\bar{s} = 0.5$, (d) $\bar{d} = 0.5$ and $\bar{s} = 1.0$, (e) $\bar{d} = 1.0$ and $\bar{s} = 1.0$, (f) $\bar{d} = 1.5$ and $\bar{s} = 1.0$, (g) $\bar{d} = 0.5$ and $\bar{s} = 1.5$, (h) $\bar{d} = 1.0$ and $\bar{s} = 1.5$, and (i) $\bar{d} = 1.5$ and $\bar{s} = 1.5$.

The variation of the dimensionless normal force $\bar{P}$ and cavity area ratio $\bar{a}$ with the dimensionless normal displacement $\bar{d}$, shown in Figs. 2.11(a) and 2.11(b), respectively, provides further insight into the protrusion spacing effect on the imprinting process. For a small protrusion distance (i.e., $\bar{s} = 0.5$), the force-distance response is similar to that of the flat surface (Fig. 2.5), suggesting a secondary effect of protrusion spacing on global parameters, such as the normal force. However, larger protrusion distances (i.e., $\bar{s} = 1.0$ and 1.5) not only increase proportionally the normal force but also induce a transition to a rapidly intensifying force at $\bar{d} \approx 1.0 - 1.2$. The sharp force increase beyond this critical normal displacement is attributed to the pronounced effect of cavity filling, which depends on the protrusion distance. As shown in Fig. 2.11(b), the filling rate of the cavities is significantly affected by the protrusion distance. While the filling of smaller cavities ($\bar{s} = 0.5$) increases moderately with the normal displacement, the larger cavities are filled up much faster, approaching saturation for $\bar{d} > 1.5$. Thus, the increase of the normal force with

the protrusion distance may be associated with the concomitant increase of the real contact area and the more prominent strain hardening due to the enhancement of material plastic shearing inside the larger cavities.

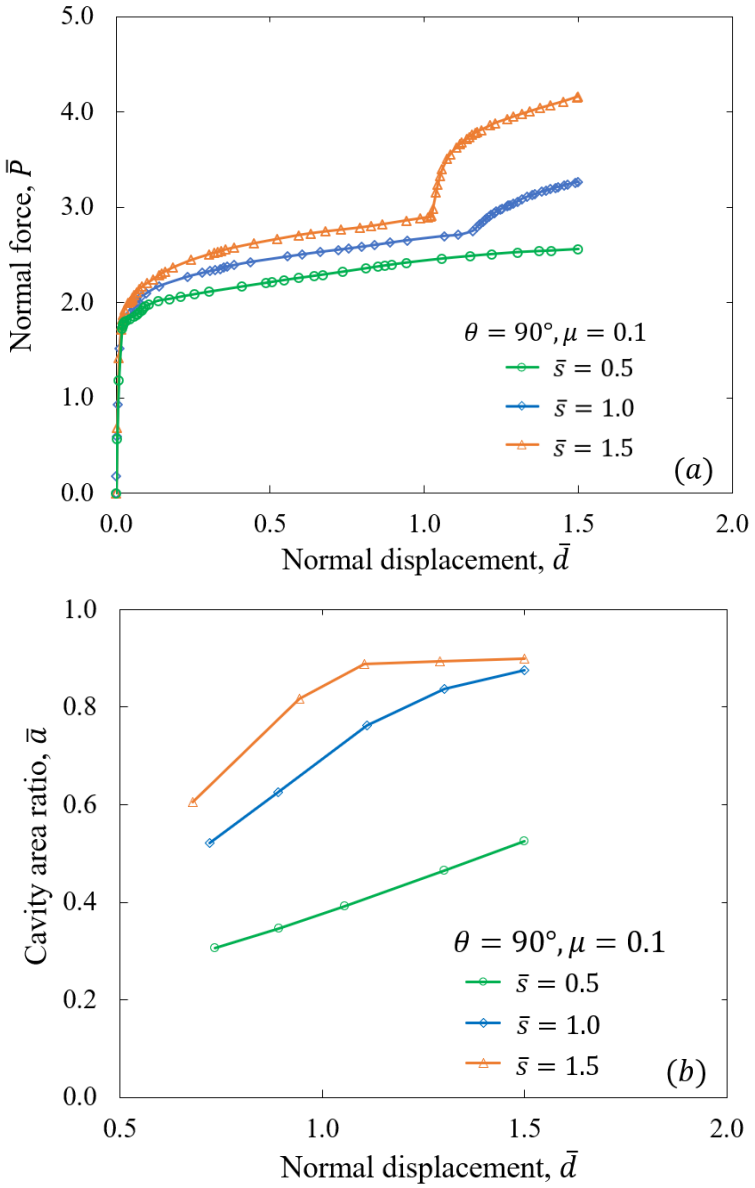

Figure 2.23 (a) Dimensionless normal force $\bar{P}$ and (b) cavity area ratio $\bar{a}$ versus dimensionless normal displacement $\bar{d}$ for an elastic-plastic substrate indented by a rigid patterned surface ($\theta = 90^o$, $\bar{s} = 0.5$, 1.0, and 1.5, and $\mu = 0.1$).

The transcription of the template geometry onto the substrate surface can be discussed in the context of the cavity area ratio results shown in Figs. 2.9(b) and 2.11(b). While increasing the normal displacement augments the replication of the template geometry on the imprinted surface, increasing the coefficient of friction and/or decreasing the protrusion spacing yields an opposite effect. This can be explained by considering the effect of friction on the plastic shear resistance of material sliding against the template surface and the dependence of cavity volume on protrusion distance discussed above. Specifically, higher friction hinders material flow into the cavities,

whereas a smaller protrusion distance reduces the free space for upward moving plastic material. These results suggest that coating the template surface with a lubricious film that reduces the adhesion of the interacting surfaces by increasing material incompatibility (Komvopoulos, 2012) or applying heat to enhance the flow ability of the substrate material by lowering its yield strength can greatly enhance the imprinting process.

Figure 2.12 shows the effect of the protrusion lateral distance (or cavity volume) on the variation of the dimensionless maximum equivalent plastic strain $\bar{\varepsilon}^{p}_{\mathrm{eq,max}}$ with the dimensionless normal displacement $\bar{d}$ for $\theta = 90^{\mathrm{o}}$ and $\mu = 0.1$. A solution of the flat surface is also shown for comparison. The increase of $\bar{\varepsilon}^{p}_{\mathrm{eq,max}}$ with $\bar{s}$ is consistent with the force results shown in Fig. 2.11(a), that is, for fixed $\bar{d}$, $\bar{\varepsilon}^{p}_{\mathrm{eq,max}}$ increases with $\bar{s}$. Moreover, as the normal displacement increases, the slopes of the strain curves of the patterned surface approach that of the flat surface, consistent with the similar deformation behaviors of patterned and flat surfaces observed at relatively large normal displacements.

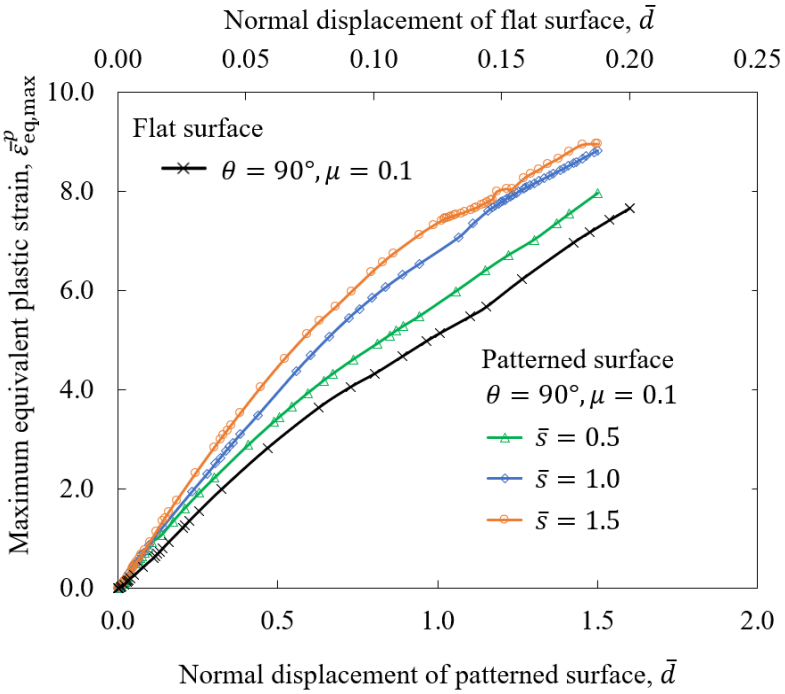

Figure 2.24 Dimensionless maximum equivalent plastic strain $\bar{\varepsilon}^{p}_{eq,max}$ versus dimensionless normal displacement $\bar{d}$ for an elastic-plastic substrate indented by a rigid flat or a rigid patterned surface ($\theta = 90^{o}$, $\bar{s} = 0.5, 1.0$, and 1.5, and $\mu = 0.1$).

In addition to metal imprinting, the present analysis has direct implications in other fields where knowledge of the mechanics of a patterned surface compressing a metallic surface is critical to the optimization of the material process. An illustrative example of an important application area is ultrasonic wire bonding, an indispensable method for manufacturing interconnects in the semiconductor industry (Long et al., 2017). In this process, a bonding tool with a patterned surface (typically V-shaped or nominally flat with a meandered surface micropattern) is used to grip onto a bonding wire of a soft metal like copper or aluminum. The oscillation of the patterned tool against

the metal wire under an applied load causes plastic flow of the wire into the tool cavities, establishing a strong grip which is critical to subsequent plastic shearing of the wire against the substrate to form a strong bond. Therefore, the quality of the bond depends strongly on the normal force, oscillation amplitude, and plastic flow of the metal wire into the tool cavities. The numerical methodology developed in this study can be easily extended to include oscillation at the template/substrate interface, heating due to sliding friction, energy dissipation in the form of plastic deformation and substrate heating, or even other types of constitutive stress-strain laws. A comprehensive analysis of the foregoing effects should be invaluable to the design of more efficient tools for metal imprinting and for optimizing the process via tactical tuning of key parameters. The effect of the oscillatory motion of a patterned template on the deformation behavior of a metallic substrate will be examined in a forthcoming publication.

2.4. Conclusions

The mechanics of metal imprinting by nominally flat and patterned surfaces was examined in the light of FEA simulations. A parametric analysis of numerical results in dimensionless form was used to elucidate the effects of surface pattern parameters on the mechanical behavior of the plastically deformed substrate material. In the case of flat-surface imprinting, high stresses and strains develop at the contact edge and corners of the rigid template, where the material exhibits excessive shearing and strain hardening. The evolution of the normal force comprises two deformation stages: an initial predominantly elastic response characterized by a large slope and a steady-state response dominated by plasticity where the normal force increases gradually with the progression of deformation. The effect of the side wall angle becomes pronounced with the advancement of plasticity, with a smaller side wall angle producing a higher normal force due to the development of a larger contact area. Although a similar deformation pattern is observed in the case of patterned-surface imprinting during the initial stage of deformation, i.e., high stress and strain concentrations at the edges and corners of the pattern protrusions, the deformation behavior is significantly affected by the evolution of plasticity that intensifies the interaction of neighboring stress/strain fields and increases the plastic flow of material into the cavities. This results in a three-stage force response, with the first two stages showing similarity with those of the flat surface and the third stage characterized by the sharp increase of the normal force caused by cavity filling that increases the contact area significantly. The normal force, cavity filling, and intensity of stress/strain fields increase with increasing protrusion distance and decreasing coefficient of friction. At large normal displacements (i.e., advanced cavity filling), the maximum equivalent plastic strain in the material adjacent to the protrusion edges and corners and the subsurface stress field in the substrate approach those of flat-surface imprinting. The results of this study provide insight into the effects of significant design and material parameters in metal imprinting and establish a modeling framework for investigating other important effects, such as oscillation and frictional heating at the template/substrate interface, more complex pattern geometries, and other constitutive models.

CHAPTER 3

Plasticity-induced damage and material loss in oscillatory contacts

3.1. Introduction

Oscillatory sliding contact affects the performance and longevity of a wide range of contact-mode electromechanical systems, contributing to frictional energy dissipation and the removal of material in the form of fine wear debris. The primitive studies of Cattaneo (1938) and Mindlin (1949) illuminated the effect of normal and tangential (shear) traction at the contact interface of two elastic bodies on the inception of slip and the deviation of the deformation response from that predicted by the classical contact theory of Hertz (1882). Mindlin and Deresiewicz (1953) investigated the contact behavior of two identical elastic spheres and reported an increase of the tangential force Q with the lateral displacement under constant load P in conjunction with the development of a circular stick zone at the center of the contact region surrounded by an annulus slip zone. The stick zone shrunk with the increase of the tangential force and ultimately vanished when $Q = \mu P$, where μ is the coefficient of friction. When the preceding slip condition was satisfied, the tangential force remained constant and full slip initiated at the contact interface. These early studies provided the incentive to examine the instigation of stick and slip under various contact conditions. For instance, Björklund (1997) investigated elastic contact of a rough surface with a perfectly flat surface under both normal and tangential loadings and observed a dependence of micro-slip at the contact interface on the standard deviation of the asperity heights. Jäger (1998) obtained analytical solutions of the tangential traction and displacements in an elastic half-space subjected to quasi-static normal and tangential loadings. Block and Keer (2008) used the summation of evenly spaced Flamant solutions to analyze periodic contact under various interfacial conditions, such as complete stick, partial slip, and frictionless sliding. Goryacheva et al. (2012) examined two-dimensional elastic contact between a flat half-space and a patterned half-space with periodically arranged grooves of variable height and identical material properties. It was shown that when the slip condition $\tau = \mu p$ (where τ and p are the nominal shear stress and contact pressure, respectively) was satisfied, the edges of the slip zones reached the groove edges, causing a transition from partial slip at the boundaries to global slip of the bodies, with the wider grooves augmenting the growth of the slip zone with the increase of the tangential load. Klimchuk and Ostryk (2020) investigated the two-dimensional Cattaneo–Mindlin elastic contact problem of two identical cylindrical bodies and obtained analytical results of the stresses inside the bodies and the contact interface and elucidated the effect of friction on the distribution of the maximum tangential stress and the development of an adhesive region at the contact interface.

Despite important insight into the mechanics of oscillatory contacts derived from the previous studies, analyzing the material removal process in oscillatory contacts requires computational methods that account for the effect of various inelastic deformation processes on cumulative damage. For instance, Kuno et al. (1989) investigated both analytically and experimentally the effect of crack initiation and propagation on fretting fatigue. Fouvry et al. (1996) used an elastic Hertzian-Mindlin contact description to quantify damage and observed wear debris formation under gross slip conditions. Giannakopoulos and Suresh (1997) used a three-dimensional finite element model of a sphere in oscillatory contact with a flat surface of the same material to study the effects of partial slip, interfacial friction, and externally applied mean stress

on the evolution of deformation and damage. Ambrico and Begley (2000) used a plane-strain model of a rigid cylinder cyclically loaded onto a flat elastic-plastic substrate to examine the progression of plasticity in the substrate during fretting and obtained numerical results that illuminate the development of plasticity, shakedown, and ratcheting in the substrate in terms of the coefficient of friction and the cyclically applied tangential force. Etsion (2010) argued that the assumptions made in the classical Cattaneo-Mindlin problem may not be physical and proposed an alternative approach for solving this problem in which the inception of sliding is treated as a plastic failure mode. Eriten et al. (2011) used Mindlin's partial slip response to monotonic and cyclic loading and incorporated elastic-plastic preload and preload-dependent friction coefficient models to predict the tangential response of the spherical asperity contacts between nominally flat surfaces undergoing fretting in terms of geometric and material properties. Song and Komvopoulos (2014) used a modified Mindlin theory to model stick-slip at the asperity contacts between a rigid fractal surface in oscillatory contact with an elastic-plastic half-space, considering the contributions of adhesion and plowing friction mechanisms to the friction force. Chen and Etsion (2019) used the finite element method (FEM) to investigate the inception of sliding at the contact interface of a coated elastic-plastic sphere strongly adhered to a rigid plane and obtained numerical results that explain the effect of the hard coating thickness on the static coefficient of friction.

Cumulative plasticity is a precursor to the loss of material in oscillatory contacts. Archard (1953) introduced the concept of the real area of contact for nominally flat surfaces and proposed an empirical law of adhesive wear in which the wear rate varies linearly with the load and is independent of the apparent area of contact. Atomistic simulations of wear particle formation at the asperity level performed by Aghababei et al. (2017) showed a dependence of the volume of wear debris on the asperity junction size, consistent with Archard's postulated dependence of the adhesive wear volume on the real area of contact; however, the former atomistic simulations did not reveal a correlation between the volume of wear debris and the applied load. Frérot et al. (2018) provided two physics-based interpretations of the wear coefficient used in Archard's wear equation. Dimaki et al. (2020) used the discrete element method to study the effects of adhesion, yield stress, and shear strength on the modes of asperity deformation and fracture in adhesive wear. Salib et al. (2008) presented a FEM model of an elastic-plastic sphere fully adhered to a rigid flat plate and approximated the volume of a wear particle formed at the inception of sliding by assuming particle detachment along a slip path of maximum shear strain within the plastic zone; however, large discrepancies were found between predicted and experimental values of the wear coefficient. Pereira et al. (2017) used a statistical analysis that combines a microscale roughness model with a macroscale fretting wear model to explore the evolution of fretting wear. Yue and Abdel Wahab (2017) used an energy-based FEM model to obtain estimates of the wear scar and the wear volume under conditions of partial slip and gross sliding, constant and variable coefficient of friction, and fixed load. Wang et al. (2020) combined FEM modeling with a model reduction method to study the role of the slip amplitude, load, and oscillation cycles in fretting wear. Zhang and Etsion (2021) incorporated a ductile fracture criterion in a FEM model of an elastic-plastic, full-stick, spherical contact subjected to normal and tangential loadings and simulated the removal of material due to adhesive wear by eliminating those elements that satisfied the failure criterion, assuming wear particle formation due to cracking below the contact interface.

Damage models have been extensively used in numerical analyses to predict the removal of material. For instance, Ben Tkaya et al. (2007) explored the effect of the attack angle on the scratch behavior of isotropic and kinematic strain hardening materials and simulated damage

initiation at a specified equivalent plastic strain and material removal due to the evolution of damage, depending on energy dissipation. Elwasli et al. (2015) incorporated the constitutive model of Johnson and Cook (1985) in an FEM model and analyzed the removal of material by scratching. Lou et al. (2014) proposed a damage model based on a ductile fracture criterion, which accounts for compressive and tensile stress triaxiality states. Mostaani et al. (2015) used FEM simulations of the scratching process to evaluate the effectiveness of the previous damage models to capture various deformation modes, e.g., plowing, wedge formation, and cutting.

Motivated by the foregoing studies and other recent efforts to model the removal of material in oscillatory contacts, a plane-strain FEM model of a rigid cylinder in reciprocating sliding contact with an elastic-plastic, strain hardening half-space was developed to examine the loss of material with the progression of plasticity-induced damage. A principal objective was to introduce a computational methodology, which can elucidate the effects of load, friction, oscillation cycles, and material behavior on the evolution of plasticity resulting in cumulative damage and ultimately the loss of material. The non-monotonic wear behavior encountered over a wide load range is interpreted in terms of the plastic shear strain distribution and the initiation of slip at the contact interface. Numerical results illuminate the effects of the applied load, plastic shear strain, and interfacial slip on the removal of material. An important contribution of the present study is the development of a computational framework for examining the effects of other important parameters (e.g., strain rate, oscillation amplitude, and frictional heating) on the evolution of damage leading to the loss of material in mechanical systems with elements operating in reciprocating sliding contact mode.

3.2. Modeling Approach

3.2.1. Finite element mesh

The plane-strain problem examined in this study is schematically depicted in Fig. 3.1(a). A rigid cylinder of radius R is pressed against an elastic-plastic half-space under a normal load P and then oscillated in the horizontal direction. The oscillation amplitude and the penetration depth are denoted by δ and d, respectively. The half-space is discretized by a $60R \times 60R$ mesh consisting of 79,613 four-node, reduced-integration, quadrilateral elements with a total of 79,936 nodes. To accurately capture the large strain gradients in the region where penetration and oscillation of the rigid cylinder takes place and to reduce the computation time, the FEM mesh is compartmentalized in three segments centered at point O, which is where the cylinder first contacts the half-space surface (Fig. 3.1(b)). The $0.4R \times 2R$ near-surface region of the mesh is uniformly refined with $0.004R$ size elements, as shown in Fig. 1(b), representing ~63% of the total number of elements. Outside of this region, a $1.2R \times 4R$ region is meshed with elements of gradually increasing size from $0.004R$ to $0.4R$. Finally, the outer part of the mesh is uniformly meshed with $0.4R$ size elements. The displacements of the nodes at the bottom boundary of the mesh are constrained in both x- and y-directions, whereas the nodes at the left and right boundaries of the mesh are free. Preliminary simulations confirmed that the above model dimensions, mesh refinement, and boundary conditions do not affect the magnitudes of global parameters (e.g., penetration depth). An oscillation cycle comprises four consecutive simulation steps of incrementally increased x-displacement of the cylinder up to the specified oscillation amplitude, i.e., incremental lateral sliding of the cylinder in the distance ranges $[0, \delta]$, $[\delta, 0]$, $[0, -\delta]$, and $[-\delta, 0]$. In each simulation,

the number of oscillation cycles N was sequentially increased to 10, while the load was fixed throughout the simulation.

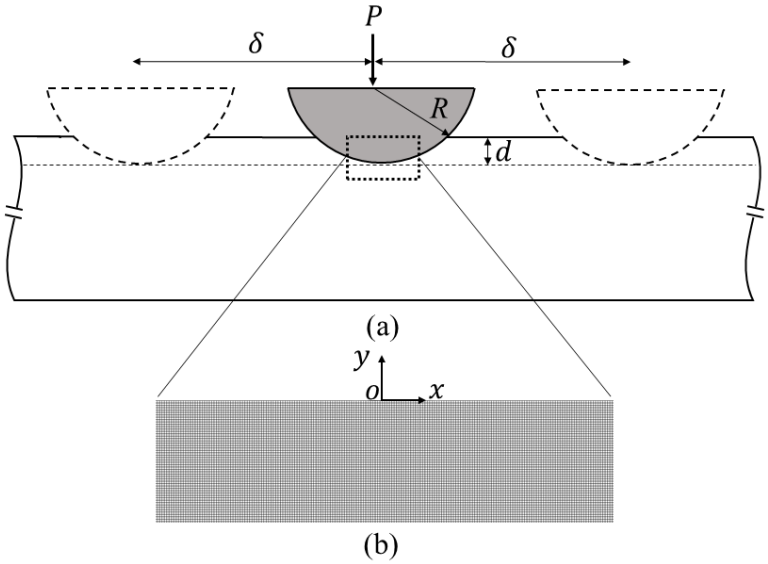

Figure 3.1 (a) Cross-sectional schematic of a rigid cylinder loaded against a half-space and (b) refined finite element mesh at the near-surface region of the half-space.

Surface contact was simulated with a finite sliding algorithm, which treats the surfaces of the deformable half-space and the rigid cylinder as slave and master surfaces, respectively, and controls the relative separation and slip between the interacting surfaces. Each slave node encountering the master surface is constrained to slide against the master surface, while the position of the slave node relative to the master surface is continuously tracked by the algorithm during the deformation. The finite sliding algorithm was implemented in the FEM analysis by using automatically generated contact elements. At each integration point of a contact element, the overclosure was adjusted to prevent a surface point of the deformed half-space to penetrate the surface of the rigid cylinder and the relative shear slip was computed afterwards. Coulomb friction was modeled by assigning to the contact elements a coefficient of friction, which relates the maximum allowable shear stress at the contact interface to the local contact pressure. Table 3.1 gives the geometric parameters, oscillation amplitude, and coefficient of friction used in the FEM simulations.

3.2.2. Damage and degradation model

The accumulation of plastic deformation due to the repetitive oscillation of the rigid cylinder under the applied load leads to cumulative damage, eventually resulting in the removal of a fully damaged element. The evolution of cumulative damage in an isotropic strain hardening material is depicted in the effective stress $\bar{\sigma}$ versus equivalent strain $\bar{\varepsilon}$ plot shown in Fig. 3.2. The stress-strain response comprises three characteristic deformation regions, namely elastic, strain hardening, and material degradation. Initially the material exhibits a linear elastic behavior up to the initial yield strength Y_0 (point A), beyond which the increase of stress causes the development of plastic deformation. In the absence of plasticity-induced damage leading to material degradation, the stress increases monotonically due to strain hardening (dashed curve in Fig. 3.2). However, a

different response is encountered when the evolution of plasticity is accompanied by cumulative damage, quantified by the dimensionless damage variable ω ($0 \leq \omega \leq 1$) given by

$$\omega = \int \frac{d\bar{\varepsilon}^p}{\bar{\varepsilon}_i^p} \tag{3.1}$$

where $\bar{\varepsilon}^p$ is the equivalent plastic strain and $\bar{\varepsilon}_i^p$ is the equivalent plastic strain at $\omega = 1$ (point B). Material degradation manifests itself in the form of a continuous decrease in yield stress and stiffness, controlled by the degradation parameter D ($0 \leq D \leq 1$). Full material degradation (failure) is attained when the equivalent plastic strain at failure $\bar{\varepsilon}_f^p$ is reached (point C). A gradual material degradation process is modeled to avoid the instantaneous removal of the fully damaged elements ($\omega = 1$), which can generate artificial stress waves and dynamic effects.

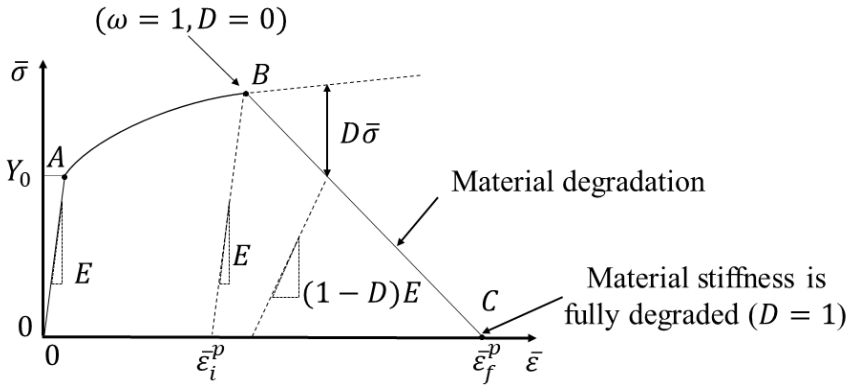

Figure 3.2 Effective stress $\bar{\sigma}$ versus equivalent strain $\bar{\varepsilon}$ plot illustrating the evolution of material damage and degradation during deformation.

A failure criterion is needed to model damage accumulation (path AB) and material degradation (path BC) of the plastically deformed elements. A common failure criterion for materials demonstrating significant ductility is that proposed by Johnson and Cook (1985), which for quasi-static, isothermal, strain hardening deformation takes the form,

$$\bar{\varepsilon}_i^p = A + B\, e^{C\eta} \tag{3.2}$$

where A, B, and C are material damage constants and η is a triaxiality parameter, given by $\eta = \sigma_m/\bar{\sigma}_M$, where σ_m is the hydrostatic stress and $\bar{\sigma}_M$ is the von Mises effective stress. Table 3.2 gives the material properties and the damage constants used in the FEM simulations. The mechanical properties given in Table 3.2 are typical of A2024-T351 aluminum alloy, which is widely used in aerospace, automotive, machining, and other industrial applications due to its high strength, low weight, good machinability, and good fatigue resistance (Asad et al., 2014).

To ensure a smooth transition from the fully damaged state (point B) to the failure state (point C), an approach based on the fracture energy for creating a crack of unit area (Hillerborg et al., 1976) was implemented in the analysis. A linear material degradation process (path BC) was modeled based on the relation (ABAQUS/CAE, 2020)

$$D = \frac{l_c\,\bar{\varepsilon}^p}{2\,G_f}\,\bar{\sigma}_c \tag{3.3}$$

where l_c is a characteristic length that depends on the aspect ratio of the element sides, G_f is the fracture energy for creating a crack of unit area, and $\bar{\sigma}_c$ is the effective stress at the inception of material degradation, i.e., $\omega = 1$ (point B). The purpose for using l_c in Eq. (3.3) is to prevent an artificial decrease of the energy dissipation due to strain localization induced by the refinement of the FEM mesh. For a first-order, plane-strain element, l_c is set equal to the square root of the area of a finite element. Thus, an artificial decrease in energy dissipation was avoided by using an element aspect ratio close to unity and setting l_c equal to the square root of the area of the smallest finite elements. The degradation parameter D is defined by the relation $\bar{\sigma}^* = (1 - D)\bar{\sigma}$, where $\bar{\sigma}^*$ is the reduced effective stress due to the damage. A finite element is removed from the FEM model when $D = 1$. The value of G_f (Table 3.2) used in all simulations corresponds to 2024-T351 aluminum alloy.

Table 3.1 Input parameters of the FEM simulations.

Parameter	Magnitude
Cylinder radius, R (mm)	5
Half-space height (mm)	300
Half-space width (mm)	300
Refined mesh height (mm)	2
Refined mesh width (mm)	10
Refined mesh size (mm)	0.02
Oscillation amplitude, δ (mm)	0.5
Coefficient of friction, μ	0.1, 0.3, 0.5

Table 3.2 Material properties and damage parameters used in the FEM simulations.

Parameter	Magnitude
Density, ρ (kg/m^3)	2700[(a)]
Initial yield strength, Y_0 (MPa)	352[(a)]
Elastic modulus, E (GPa)	73[(a)]
Poisson's ratio, ν	0.33[(a)]
Fracture energy, G_f (N/mm)	20[(a)]
Damage parameter, A	0.13[(b)]
Damage parameter, B	0.13[(b)]
Damage parameter, C	–1.5[(b)]
Strain hardening coefficient, K (MPa)	440[(a)]
Strain hardening exponent, n	0.42[(a)]

[(a)]Asad et al. (2014).
[(b)]Johnson and Holmquist (1989).

3.2.3. Constitutive model

To model quasi-static, isothermal, isotropic strain hardening material behavior, the half-space is modelled to follow the constitutive stress-strain law (Johnson and Cook, 1985)

$$\bar{\sigma} = Y_0 + K\bar{\varepsilon}^n \tag{3.4}$$

where K is the strain hardening coefficient and n is the strain hardening exponent.

Yielding is determined by the von Mises yield criterion, given by

$$\bar{\sigma} = \left(\frac{3}{2}S_{ij}S_{ij}\right)^{1/2} = Y \tag{3.5}$$

where S_{ij} are components of the deviatoric stress tensor and Y is the current yield strength.

The evolution of plasticity is described by the equivalent plastic strain $\bar{\varepsilon}^p$, computed by

$$\bar{\varepsilon}^p = \int_{\Omega} \left(\frac{2}{3} d\varepsilon_{ij}^p d\varepsilon_{ij}^p \right)^{1/2} \tag{3.6}$$

where Ω is the strain path used to track the accumulation of plasticity and $d\varepsilon_{ij}^p$ are plastic strain increments.

3.2.4. Finite element simulations

All of the FEM simulations were performed in displacement-control mode using the multi-physics code ABAQUS/Explicit (ABAQUS/CAE, 2020). Special attention was given to the selection of the time step. A large time step in a quasi-static analysis that uses the explicit solver can yield significant dynamic effects, whereas a small time step can greatly increase the computation time. A mass scaling factor k_m was used in this study to reduce the computation time by $k_m^{1/2}$. To ensure that the selected time step preserves the quasi-static condition, the kinetic energy must be less than 5% of the internal energy. For the time step $\Delta t \approx 10$ ns used in all the simulations, the kinetic energy was found to be about 1% to 4% of the internal energy, which is within the admissible range.

3.2.5. Dimensionless parameters

To obtain generalized solutions, the input and output simulation parameters were normalized by appropriate quantities. Specifically, the dimensionless load $\bar{P}$ is defined by P/P_{Y0}, where P_{Y0} is the load at initial yield expressed by $P_{Y0} = \pi R(p_0^2/E^*)$, where p_0 is the maximum Hertzian pressure at the inception of yielding given by $p_0 = 1.79Y_0$ (Mises yield criterion) and $E^* = E/(1-\nu^2)$, where E and ν are the elastic modulus and Poisson's ratio, respectively. The dimensionless normal displacement (penetration depth) is defined by $\bar{d} = d/R$. The dimensionless plastic area is given by $\bar{A}_p = A_p/A_i$, where A_p is the plastic area, computed by summing up the areas of all the elements with $\bar{\varepsilon}^p > 0.002$, and A_i is the contact area established between the cylinder and the half-space before the commencement of oscillation, assuming a unit length distance in the out-of-plane direction. The dimensionless wear area $\bar{A}_w$ is obtained by dividing the wear area A_w, i.e., the sum of the areas of all the elements removed from the model ($D = 1$), by the plastic area A_p computed at the same instant of the simulation. The averaged fraction of the contact area in slip mode $\bar{A}_s$ is calculated before the removal of the fully damaged elements (i.e., $\omega < 1$) by dividing the total slip area by the total contact area, assuming a unit length distance in the out-of-plane direction, with both areas averaged over the same oscillation cycle.

3.3. Results and Discussion

Insight into the progression of damage in an elastic-plastic half-space can be obtained by tracking the damage parameter ω during oscillation. Figure 3.3 shows the evolution of ω in the first 5 oscillation cycles for $\bar{P} = 13$ and $\mu = 0.3$. Forward plastic shearing during the right stroke of the first cycle ($N = 1/4$) caused damage to the elements adjacent to the contact interface, surface sinking, and the formation of a shallow pile-up (Fig. 3.3(a)). Subsequent backward sliding of the

cylinder up to the center of oscillation ($N = 1/2$) resulted in the lateral expansion of the damage zone and additional damage at the right oscillation edge ($x = +\delta$) due to more plastic deformation accumulated during the unloading (Fig. 3.3(b)). Backward plastic shearing during the left stroke of the first cycle ($N = 3/4$) enlarged the damage zone in the lateral direction, increased the material pile-up at the left oscillation edge ($x = -\delta$), and produced a pocket of excessive damage adjacent to the left oscillation edge (Fig. 3.3(c)), which extended slightly toward the oscillation center ($x = 0$) at the end of the first cycle ($N = 1$) (Fig. 3.3(d)). The asymmetric damage distribution showing more damage at the left oscillation edge is attributed to the larger volume of material plowed during backward sliding due to the increase of the penetration depth in the previous stage of forward sliding. The second cycle ($N = 2$) created a fairly uniform, highly intensified, enlarged damage zone extending deeper into the substrate owing to further advancement of the cylinder into the half-space (Fig. 3.3(e)). The damage zone continued to expand in the following cycles due to the proliferation of plasticity, as shown by the damage contours obtained after 5 cycles (N =5) (Fig. 3.3(f)). Repetitive forward and backward plastic shearing resulted in material build-up at both oscillation edges, larger pile-ups, and deeper penetration of the cylinder. Moreover, the removal of the fully damaged elements (ω =1) adjacent to the contact interface when the degradation parameter D reached unity also contributed to the increase of the penetration depth. As this process perpetuated itself during the oscillation, elements at deeper locations reaching full damage (ω =1) were also removed (D =1), aiding to the enlargement of both the damage zone and the pile-ups (Fig. 3.3(f)).

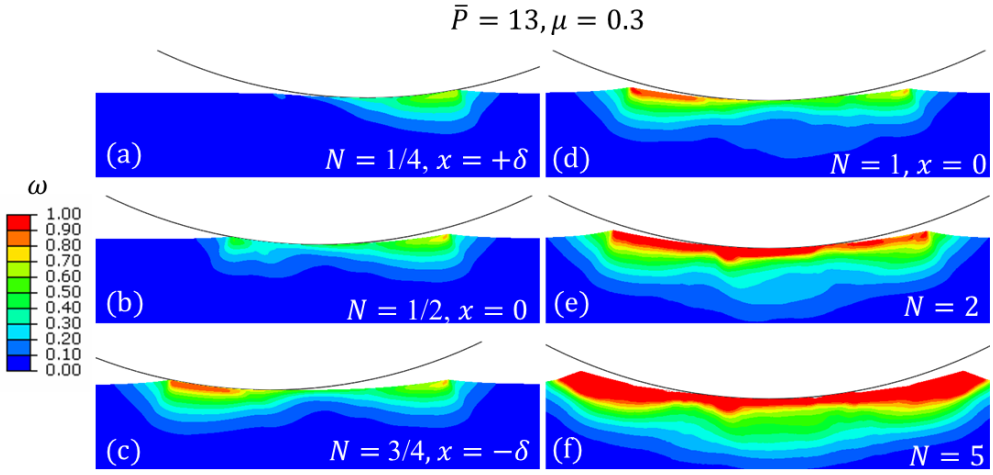

Figure 3.3 Evolution of damage parameter ω during the (a-c) first oscillation cycle and after the (d) first, (e) second, and (f) fifth oscillation cycles.

Figure 3.4 shows the dimensionless normal displacement (penetration depth) $\bar{d}$ as a function of oscillation cycles N for $\bar{P} = 13 - 79$ and $\mu = 0.3$. As expected, the penetration depth increased with the load. Even though some of the simulations did not reach 10 oscillation cycles due to convergence problems, the obvious trend is for $\bar{d}$ to stabilize after a few cycles. This trend is more apparent in the high-load cases ($\bar{P} \geq 33$) showing a stable $\bar{d}$ after ~5 cycles. This behavior may be attributed to the greater conformity of the cylinder with the substrate at higher loads that intensified plastic shearing and fostered the formation of larger pile-ups.

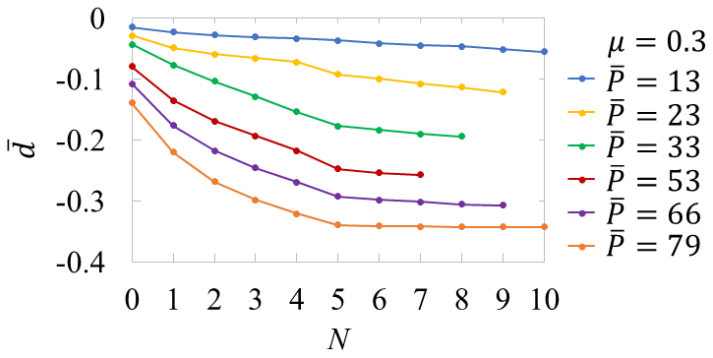

Figure 3.4 Dimensionless penetration depth $\bar{d}$ versus number of oscillation cycles N for $\bar{P} = 13 - 79$ and $\mu = 0.3$.

The effects of the load and the coefficient of friction on the development of plasticity during oscillatory contact can be further interpreted in the light of the simulation results of the dimensionless plastic area $\bar{A}_p$ shown in Fig. 3.5 (The fewer oscillation cycles attained in some of the simulations are due to convergence problems instigated by the excessive deformation of some elements). All of the simulations show a sharp increase of $\bar{A}_p$ after a few cycles. The results also show that the lower the load and the higher the coefficient of friction, the more cycles for $\bar{A}_p$ to stabilize. Conversely to the sharp increase of A_p with the load (data not shown here for brevity), $\bar{A}_p$ decreased with the increase of the load (Fig. 3.5(a)), indicating the development of more plastic deformation during the loading phase than the oscillation phase of the high-load simulations. This does not imply that a low load produces a larger plastic area A_p (for a given number of cycles), but a more prominent effect of the shear surface traction due to sliding in the oscillation phase of the low-load simulations. For instance, after 10 cycles, the plastic zone for $\bar{P} = 13$ increased by a factor of ~5 compared to a factor of ~2 for $\bar{P} = 79$. Furthermore, the increase of $\bar{A}_p$ with μ at a given load (Fig. 3.5(b)) demonstrates an increasing contribution of the shear surface traction to plasticity with increasing friction. The increase of friction augmented plastic shearing in the subsurface, dramatically increasing $\bar{A}_p$ after a few cycles. For example, for a fixed load ($\bar{P} = 33$), the plastic zone size in the high-friction simulation ($\mu = 0.5$) increased by a factor of >3.5 after only 4 cycles, as opposed to a factor of <3 in the low-friction simulation ($\mu = 0.1$).

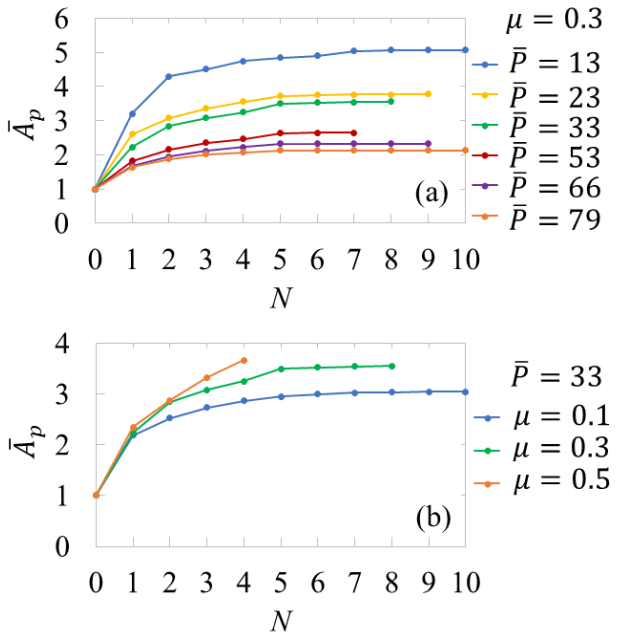

Figure 3.5 Dimensionless plastic area $\bar{A}_p$ versus number of cycles N for: (a) $\bar{P} = 13 - 79$ and $\mu = 0.3$ and (b) $\mu = 0.1 - 0.3$ and $\bar{P} = 33$.

Important insight into the development of plasticity with the accumulation of oscillation cycles leading to the loss of material was obtained by tracking the dimensionless damage parameter ω during the evolution of damage in the plastically deformed elements. The increase of ω can be linked to the progression of damage. When $\omega = 1$ ($D = 0$) in a certain element, it is presumed that the element enters the material degradation regime where it undergoes a stiffness reduction, resulting in the decrease of its load carrying capacity (Fig. 3.2) and, ultimately, its removal from the model when full degradation is reached ($D = 1$). Figure 3.6(a) shows the variation of $\bar{A}_w$ with the number of oscillation cycles N for $\mu = 0.3$ and $\bar{P} = 13 - 79$. All of the simulations demonstrate a fairly linear increase of $\bar{A}_w$ with N, consistent with the linear variation of the wear volume with the sliding distance predicted by Archard's wear law. Figure 6(b) shows the effect of the coefficient of friction μ on the evolution of $\bar{A}_w$ for $\bar{P} = 33$. The marginal plastic shearing in the low-friction simulation ($\mu = 0.1$) did not cause any loss of material. However, the increase of the coefficient of friction intensified plastic shearing, yielding a fairly linear increase of $\bar{A}_w$ with N, much faster in the high-friction simulation ($\mu = 0.5$) than the intermediate-friction simulation ($\mu = 0.3$).

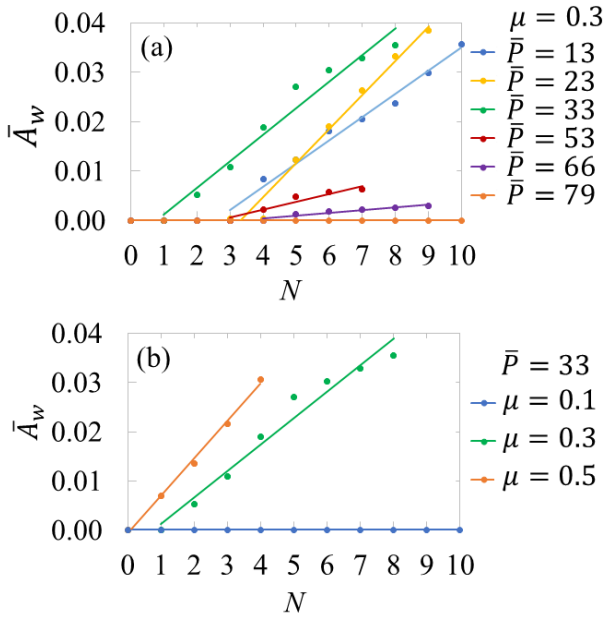

Figure 3.6 Dimensionless wear area $\bar{A}_w$ versus number of oscillation cycles N for (a) for $\bar{P} = 13 - 79$ and $\mu = 0.3$ and (b) $\mu = 0.1 - 0.3$ and $\bar{P} = 33$.

Furthermore, Fig. 3.6(a) shows an increasing trend of the wear area with the load increase up to $\bar{P} = 33$, which is also consistent with Archard's wear law. However, an opposite trend is shown for higher loads ($\bar{P} \geq 53$). This seemingly counterintuitive behavior can be explained by considering iso-strain contour distributions of the plastic shear strain γ_{xy}^p representative of low-load ($\bar{P} = 13$) and high-load ($\bar{P} = 79$) oscillatory contact, corresponding to the linear increase of wear with accumulating cycles and no wear, respectively (Fig. 3.6(a)). For low-load oscillatory contact, γ_{xy}^p is confined at the oscillation edges after the first cycle, with the left zone of γ_{xy}^p demonstrating slightly higher plastic strains (Fig. 3.7(a)), a consequence of the asymmetric nature of the shearing process. The second cycle increased the deformation in the two plastic shear zones (especially the right zone), enlarged the material pile-ups at the oscillation edges, and increased further the penetration of the cylinder into the half-space (Fig. 3.7(c)). A similar, though less pronounced, tendency was encountered after the third cycle, with the highest γ_{xy}^p arising at the contact interface (Fig. 3.7(e)). Thus, in the low-load simulation, the region showing the highest propensity for material loss is adjacent to the contact interface, where plastic shearing is more prominent. For high-load oscillatory contact, however, the iso-strain contours of γ_{xy}^p reveal a different deformation behavior. Specifically, while plastic shearing is again confined at the oscillation edges after the first cycle (Fig. 3.7(b)), the plastic shear zones are located well below the contact interface and the strains are smaller than those in the low-load simulation (Fig. 3.7(a)). (Note the use of different magnifications in the low- and high-load simulation results shown in Fig. 3.7 to better reveal the regions of high γ_{xy}^p strain.) This difference is attributed to the significantly larger volume of material resisting the oscillatory motion of the cylinder for $\bar{P} = 79$ than $\bar{P} = 13$, as evidenced by the results of the penetration depth (Fig. 3.4). Similar to the low-load simulation, the penetration depth and the size of the plastic shear zones increased in the second (Fig. 3.7(d) and third (Fig. 3.7(f)) cycles of the high-load simulation; however, the maximum γ_{xy}^p is located

away from the contact interface and its magnitude is less than that in the low-load simulation. As a result, less plastic shearing occurred in the high-load simulation due to less slip at the contact interface, a consequence of the reduced lateral movement instigated by the larger volume of material surrounding the deeper penetrating cylinder. This mitigated the conducive effect of friction on plastic shearing, consequently suppressing the build-up of plasticity-induced damage and, in turn, weakening the propensity for wear.

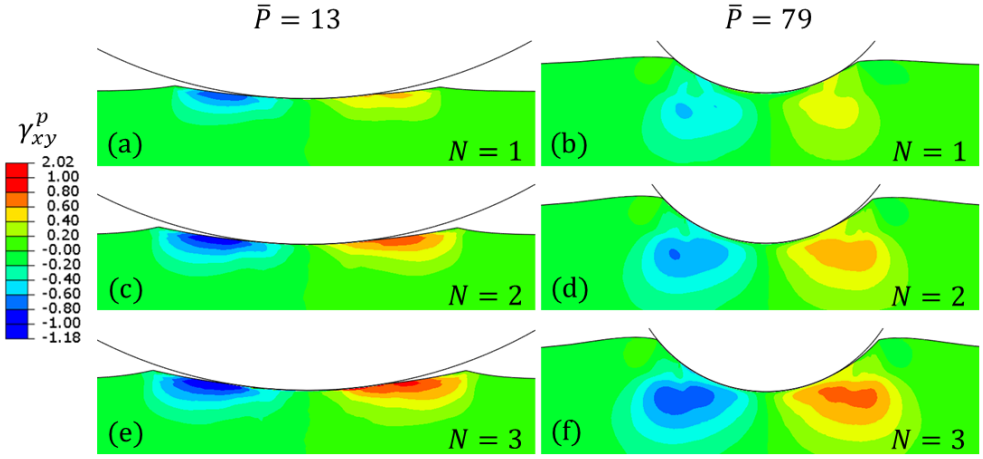

Figure 3.7 Contours of plastic shear strain γ_{xy}^{p} after the first ($N = 1$), second ($N = 2$), and third ($N = 3$) oscillation cycles for $\bar{P} = 13$ (left column), $\bar{P} = 79$ (right column), and $\mu = 0.3$.

Additional insight into the reduced interfacial slip in high-load oscillatory contacts can be obtained by inspecting the effect of the applied load on the amount of slip at the contact interface. Figure 3.8 shows the averaged fraction of the contact area in slip mode $\bar{A}_s$, calculated before the instigation of material loss, (i.e., $\omega < 1$), as a function of load $\bar{P}$ for $\mu = 0.3$. The decreasing tendency of $\bar{A}_s$ with increasing $\bar{P}$ confirms the decrease of the interfacial slip with the load increase. In particular, $\bar{A}_s$ is greater than 30% in the low-load range ($\bar{P} < 20$) and less than 15% in the high-load range ($\bar{P} > 60$). The results shown in Fig. 3.8 provide additional support to the decreasing intensity of plastic shearing (henceforth, less damage accumulation and lower propensity for material loss) with the increase of the applied load.

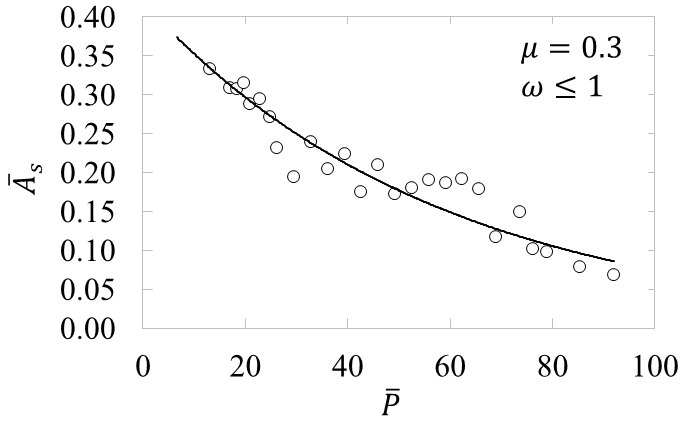

Figure 3.8 Averaged fraction of the contact area in slip mode $\bar{A}_s$ before the instigation of the removal of fully damaged elements versus load $\bar{P}$ for $\mu = 0.3$.

The present analysis provides a mechanistic understanding of the synergistic effects of load and friction on plasticity-induced damage leading to the progressive material degradation and, ultimately, the loss of material in oscillatory contacts. The quasi-static, isothermal, strain hardening constitutive model used in this study can be modified to account for strain rate and temperature effects on plasticity-induced damage by implementing the full ductile failure criterion of Johnson and Cook (1985) and a multi-scale roughness description by superimposing a fractal surface profile to the cylinder's contour to create a fractal-regular surface (Wang and Komvopoulos, 1994). From a fundamental standpoint, this study provides a computational framework for performing parametric studies of the mechanical performance of oscillatory contacts operating under various loading and friction conditions.

3.4. Conclusions

A contact mechanics analysis of the evolution of plasticity in oscillatory contacts was performed to examine how the accumulation of plasticity-induced damage and material degradation lead to the removal of material. A damage model based on a ductile failure criterion was used to simulate the loss of material by removing the fully damaged elements from the model. A parametric FEM study was conducted to elucidate the effects of the applied load and coefficient of friction on the advancement of plasticity and the loss of material in terms of the representative dimensionless parameters. The main findings of the present study can be summarized as following.

(1) A dimensionless damage parameter ω was used to track the progression of plasticity-induced damage that leads to the loss of material in oscillatory contacts for a range of load and coefficient of friction.
(2) The penetration depth increased with the load and the number of oscillation cycles, showing a clear trend to stabilize after a few cycles, which was more evident in the high-load simulations.
(3) The dimensionless plastic and wear areas increased with the coefficient of friction due to the intensification of plastic shearing, revealing the critical role of friction in the development of plasticity, the advancement of damage, and the instigation of material loss.

(4) The dimensionless wear area increased linearly with the oscillation cycles and the load up to a threshold, consistent with Archard's classical theory of adhesive wear. However, an opposite trend was observed with loads above the load threshold, which was explained by considering the distribution of the plastic shear strain in the low- and high-load oscillations and the load dependence of the averaged fraction of contact area in slip mode. While the highest plastic shear strains arose adjacent to the contact interface in the low-load oscillations, their locations shifted well below the contact interface and their magnitudes decreased in the high-load oscillations.
(5) The averaged fraction of the contact area in slip mode demonstrated an overall tendency to decrease with the increase of the load, indicating a significant decrease in interfacial slip at high loads, which was attributed to the restricted movement of the cylinder due to the larger volume of the surrounding material. Consequently, less plastic shearing occurred in the high-load oscillations, resulting in less damage accumulation and loss of material.

The results of this study provide insight into the effects of the load and the coefficient of friction on the loss of material in oscillatory contacts due to the accumulation of plasticity. An important contribution of this work is the development of a computational methodology for performing mechanistic analyses of the effects of other important parameters, such as strain rate, temperature, surface roughness, and oscillation amplitude, on the evolution of plasticity-induced damage and the loss of material in oscillatory contacts.

CHAPTER 4

A mechanics analysis of plasticity-induced damage leading to material loss at fractal contact interfaces undergoing fretting wear

4.1. Introduction

Small-amplitude oscillatory sliding (fretting) affects the performance and durability of a wide range of contact-mode devices, such as microelectromechanical systems, artificial total joint replacements, oscillating-slide actuators, bolted and riveted joints, shrink-fitted couplings, and components operating in a microgravity environment. Fretting contact conditions are conducive to localized accumulation of plasticity, ultimately leading to the loss of material in the form of fine wear debris. Consequently, insight into the evolution of plasticity in oscillatory contacts is critical to the effective operation and endurance of many load-bearing components. The majority of the investigations focused on fretting wear of materials have been mostly based on experimental evidence. For example, Waterhouse (1984) discussed fretting wear of steels under conditions of extremely low frequencies and high temperatures and in the presence of aqueous solutions causing the removal of material by chemical dissolution. Vingsbo and Söderberg (1988) developed fretting maps entailing three regimes – stick (limited surface damage), mixed stick-slip (mild wear with possible cracking), and gross slip (severe damage). Experiments by Zhou and Vincent (1995) revealed the existence of another fretting regime, between the stick-slip and gross slip regimes, where wear of ductile materials comprises particle detachment and fatigue crack nucleation. Li and Lu (2013) investigated room-temperature fretting wear of Inconel 600 alloy in dry air and found a correlation of damage and wear mechanisms with oscillation amplitude. Specifically, partial slip (microslip) was dominant at small amplitudes and surface damage was influenced by localized adhesive wear in the stick zone with cracks only forming in the stick-slip region, whereas the gross slip zone became dominant with the increase of the oscillation amplitude and oxidation and delamination wear were the prevalent mechanisms of material loss. The foregoing studies are representative of a vast literature illustrative of the complex nature of the fretting wear process. This is mainly due to variations in the contact interface conditions (i.e., stick and slip zones), normal and tangential tractions, oscillation amplitude, and environmental conditions. Therefore, understanding the development of stresses and plasticity leading to surface damage and, consequently, the loss of material in oscillatory contacts is of utmost importance.

The first mechanics analyses dealing with stick-slip at the contact interface of identical elastic bodies, attributed to Cattaneo (1938) and Mindlin (1949), yielded a deformation behavior significantly different from that predicted by the classical contact theory of Hertz (1896), which neglected the presence of interfacial shear (friction) traction. However, contrary to identical materials, as in the Cattaneo-Mindlin problem, deriving analytical solutions for contacting dissimilar materials is not straightforward due to coupling of the normal and shear tractions, implying that even in the absence of shear traction, a normal traction can cause microslip at the contact interface. The solution becomes even more cumbersome when plastic deformation of the contact bodies is included in the analysis. Therefore, it is necessary to implement numerical approaches to circumvent this problem. Bazrafshan et al. (2018) used the boundary element method to examine stick-slip at the contact interface of two bodies with dissimilar properties in the presence of adhesion, modeled by a Dugdale approximation of the adhesive energy, and confirmed that the evolution of the slip zone over the contact area differed from that predicted by

the Cattaneo-Mindlin solution. McColl et al. (2004) incorporated a modified version of the classical wear equation introduced by Archard (1953) in a finite element method (FEM) analysis of fretting wear and predicted the variation of the contact pressure, relative slip at the contact interface, subsurface stresses, and wear profile with the number of fretting cycles for different normal loads. Bortoleto et al. (2013) implemented Archard's linear wear law and adaptive meshing to predict the loss of material in dry sliding in a similar FEM analysis; however, the numerical approach overestimated the mass loss measured from experiments. Martínez et al. (2012) performed an FEM analysis that also used adaptive meshing at the end of each converged increment and based on a power-law relationship between the wear volume and the normal load derived from fitting wear data, in contrast with Archard's linear wear law, they obtained solutions for the loss of material in reciprocating sliding. Hu et al. (2016) performed an FEM analysis of the role of plasticity in fretting wear using fictitious eigenstrains to make mesh adjustments for the nodes removed from the slip zone and observed a steady movement of the stick-slip boundary into the stick region when the yield strength was locally exceeded, subsequently leading to gross wear damage. Elwasli et al. (2015) incorporated the constitutive model developed by Johnson and Cook (1985) in an FEM model to analyze the removal of material by the scratch process. Sarkar et al. (2019) introduced a localized gradient damage model into an FEM code, which was more effective in reducing the range of stress oscillations than the conventional damage model. Zhang et al. (2019) used a kinematic hardening constitutive relation in an FEM model to simulate cyclic ratcheting in fretting wear leading to the formation of wear debris and reported that the total wear volume was a linear function of frictional energy dissipation. Cen and Komvopoulos (2022) developed an FEM model to examine the evolution of plasticity-induced damage resulting in the loss of material from an isotropic strain hardening half-space in reciprocating sliding contact with a rigid cylinder and obtained numerical results illuminating the effects of normal load and friction on the development of plasticity, the accrual of damage, and the loss of material with the number of oscillation cycles.

Although the previous studies provided valuable insight into the evolution of stick-slip at contact interfaces and numerical approaches for predicting the loss of material under fretting conditions, they cannot be applied to real surfaces exhibiting multi-scale roughness. Most engineering surfaces demonstrate similar characteristics at different length scales, a property known as self-affinity that is described by fractal geometry (Mandelbrot, 1967). Accordingly, significant advances in contact mechanics were encountered since the early analytical studies to implement fractal geometry for describing the topography of contacting surfaces (Majumdar and Bhushan, 1990, 1991; Wang and Komvopoulos, 1994a, 1994b, 1995; Yan and Komvopoulos, 1998). For example, Komvopoulos and Yan (1997) used a two-dimensional (2D) scale-independent fractal description that resembled a real engineering surface to obtain analytical solutions for different adhesion force components, such as van der Waals, electrostatic, and capillary forces, and to analyze deformation at the asperity level at the contact interface of microelectromechanical systems in terms of surface roughness (fractal) parameters, applied voltage, and material properties. Song and Komvopoulos (2014) used a modified Mindlin theory to model stick-slip at the asperity contacts established between a rigid fractal surface in oscillatory contact with an elastic-plastic half-space and included the contributions of adhesion and plowing friction mechanisms to the friction force in their theoretical treatment of oscillatory contact behavior. Hu et al. (2000) developed an adaptive FEM approach for frictionless elastic contact of fractal surfaces and used an iterative procedure to refine the finite element mesh both in the contact zone and the interior of the contacting bodies. Sahoo and Ghosh (2007) performed a three-dimensional (3D) FEM analysis of a rigid plane in contact with an elastic or elastic-plastic fractal

surface with varying fractal parameters, and Chatterjee and Sahoo (2014) used a 3D FEM model to study the effect of the elastic modulus on the contact pressure, contact area, and surface interference for a rigid flat in contact with an elastic-plastic fractal surface. However, only numerical solutions for global parameters, such as contact area and vertical displacement versus normal load, were reported in the previous two studies.

The objective of the present analysis was to elucidate the evolution of the subsurface stresses and plastic strains responsible for the accumulation of damage, ultimately leading to the removal of material in oscillatory contacts. Consequently, to model cumulative damage and material degradation, a failure criterion was implemented in the FEM analysis of an elastic-plastic half-space exhibiting isotropic strain hardening in reciprocating sliding contact with a rigid, rough surface characterized by fractal geometry. An approach based on the fracture energy for creating a crack of unit area was used to obtain a smooth transition from fully damaged material to failure. Numerical results displaying the variation of subsurface stresses, plasticity, and material removal rate with fractal parameters, normal load, and oscillation cycles illuminate the effect of surface topography (roughness) and accrual of plasticity-induced damage on the progression of the loss of material due to fretting wear.

4.2. Modeling and Computational Approaches

4.2.1. Surface Characterization

Fractal geometry is characterized by the scale-invariant properties of continuity, non-differentiability, and self-affinity, which are related to intrinsic physical laws that govern the generation of surfaces. Fractal geometry was developed by Mandelbrot (1967) to describe the irregularity and disorder of objects and was later introduced in the field of contact mechanics to characterize the topography of elastic-plastic contact surfaces (Majumdar and Bhushan, 1990, 1991) and the thermo-electro-mechanical behavior of contact interfaces (Wang and Komvopoulos, 1994a, 1994b, 1995; Komvopoulos, 2020). A 2D fractal surface $z(x)$ can be represented by a modified W-M function (Ausloos and Berman, 1985), expressed in modified form as follows (Yan and Komvopoulos, 1998):

$$z(x) = L\left(\frac{G}{L}\right)^{D-1}\sum_{n=0}^{M}\frac{\cos(2\pi\gamma^n x/L)}{\gamma^{(2-D)n}} \tag{4.1}$$

where L is the fractal sample length, G is the fractal roughness, D is the fractal dimension ($1 < D < 2$), and γ is a scaling parameter ($\gamma > 1$) used for phase randomization, which determines the density of frequencies in the surface profile. Surface flatness and frequency distribution density considerations have shown that an appropriate choice is $\gamma = 1.5$ (Komvopoulos and Yan, 1997). The scaling parameter γ also exists in the relation that characterizes self-affine fractals, given by $z(\gamma x) = \gamma^{(2-D)}z(x)$ (Berry and Lewis, 1980), indicating that if the lateral length x is magnified by γ, then the vertical length (height) z is magnified by $\gamma^{(2-D)}$. Equation (1) exemplifies a 2D surface profile by a series of cosine functions with frequencies geometrically increasing from the lowest frequency $\omega_l = 1/L$ to the highest frequency $\omega_h = 1/L_0$, where L_0 is the smallest characteristic length, typically presumed equal to at least 5–6 times the lattice distance for

continuum description to hold; thus, in the present study, L_0 was set equal to 5 nm. The parameter M in Eq. (4.1) is the number of frequencies in the surface profile, defined by

$$M = \text{int}\left[\frac{\log(L/L_0)}{\log\gamma}\right] \tag{4.2}$$

where int[…] denotes the integer part of the number inside the brackets. Both G and D are frequency invariant and can be experimentally determined from a log-log plot of the power spectral density (PSD) function of the real surface by a linear fit through the PSD data. The fractal parameters G and D control the amplitude of the wavelengths comprising the surface profile and the amplitude ratio of short-to-long wavelength components, respectively. Thus, Eq. (4.1) was used to generate random 2D surface profiles by varying the magnitudes of the scale-independent parameters G and D for the sample length range where the surface topography exhibited a fractal behavior. To avoid the coincidence of phases at all frequencies at $x = 0$ (Eq. (4.1)), the fractal surfaces used in the FEM simulations were generated in the length range of 200 to 2200 nm.

4.2.2. Finite Element Model

Figure 4.1 shows schematically a fractal surface in reciprocal sliding contact with a half-space under a normal load P. The oscillation amplitude and the penetration depth are denoted by δ and d, respectively. The fractal surface was generated from Eq. (4.1) using the parameters listed in Table 4.1. The half-space is discretized by a $5L \times 5L$ mesh consisting of 83,707 four-node, reduced-integration, quadrilateral elements with a total of 84,177 nodes. Due to the large stress and strain gradients in the region where penetration and reciprocal sliding occurred and to minimize the computation cost, the mesh was compartmentalized in four regions. The $0.01L \times L$ near-surface region I of the mesh was uniformly refined with $0.0005L$ size elements, representing ~48% of the total number of elements. The $0.2L \times 1.5L$ region II was meshed with elements of gradually increasing size from $0.0005L$ to $0.01L$. A $0.4L \times 5L$ transitional region III with an element size increasing from $0.01L$ to $0.05L$ was used to interface the foregoing mesh regions with a $4.6L \times 5L$ bulk region IV consisting of $0.05L$ size elements. The node displacements of the bottom boundary of the mesh were fully constrained, whereas the nodes at the left and right boundaries of the mesh were left unconstrained. An oscillation cycle comprised four consecutive simulation steps of incrementally increasing lateral displacement of the fractal surface up to the specified oscillation amplitude, i.e., sequential incremental sliding of the fractal surface in the ranges $[0, \delta]$, $[\delta, 0]$, $[0, -\delta]$, and $[-\delta, 0]$. In each simulation, the normal load was kept constant, the oscillation amplitude δ was fixed at $0.0025L$, and the number of oscillation cycles N was consecutively increased to 5.

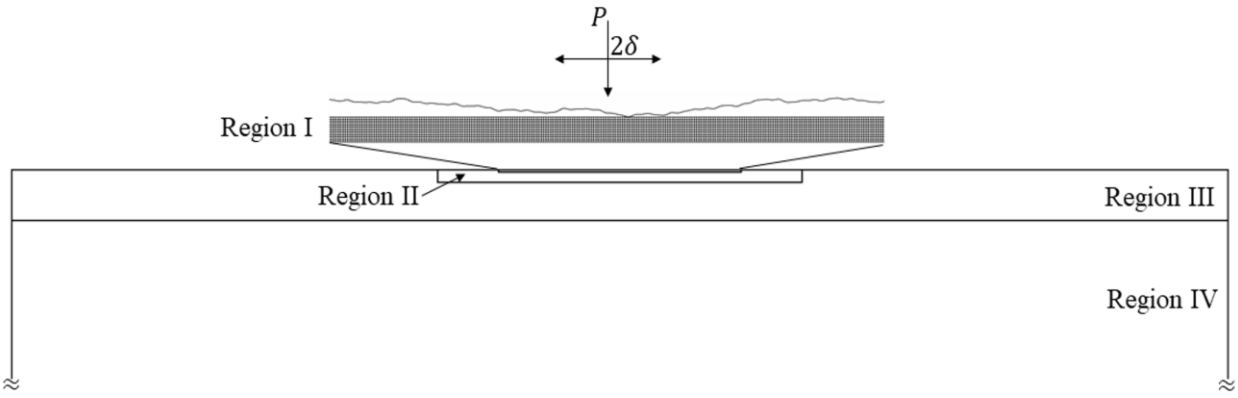

Figure 4.1 Contact model consisting of four regions with different finite element refinements.

4.2.3. Damage Model

To simulate the removal of fully damaged material due to the accumulation of plasticity-induced damage in the half-space during oscillatory sliding contact with the fractal surface, the cumulative damage model depicted in Fig. 4.2 was used in the present analysis. The effective stress $\bar{\sigma}$ versus equivalent strain $\bar{\varepsilon}$ response, shown in Fig. 4.2, comprised three characteristic deformation regions, i.e., elastic, strain hardening, and material degradation. The half-space material exhibited linear elastic deformation up to the initial yield strength Y_0 (point A), followed by elastic-plastic deformation for higher stresses. In the absence of material damage, the stress increased monotonically due to strain hardening (dashed curve). However, a different response commenced when the development of plasticity induced cumulative damage, quantified by a dimensionless damage variable ω $(0 \leq \omega \leq 1)$ given by

$$\omega = \int \frac{d\bar{\varepsilon}^p}{\bar{\varepsilon}_i^p} \tag{4.3}$$

where $\bar{\varepsilon}^p$ is the equivalent plastic strain and $\bar{\varepsilon}_i^p$ is the equivalent plastic strain at $\omega = 1$ (point B). Material degradation manifested itself in the form of a continuous decrease in yield stress and stiffness, controlled by a degradation parameter ζ $(0 \leq \zeta \leq 1)$. Full material degradation commenced when the equivalent plastic strain at failure $\bar{\varepsilon}_f^p$ was reached (point C). A gradual material degradation process was modeled to circumvent the instantaneous removal of fully damaged finite elements ($\omega = 1$), which could generate artificial stress waves and dynamic effects.

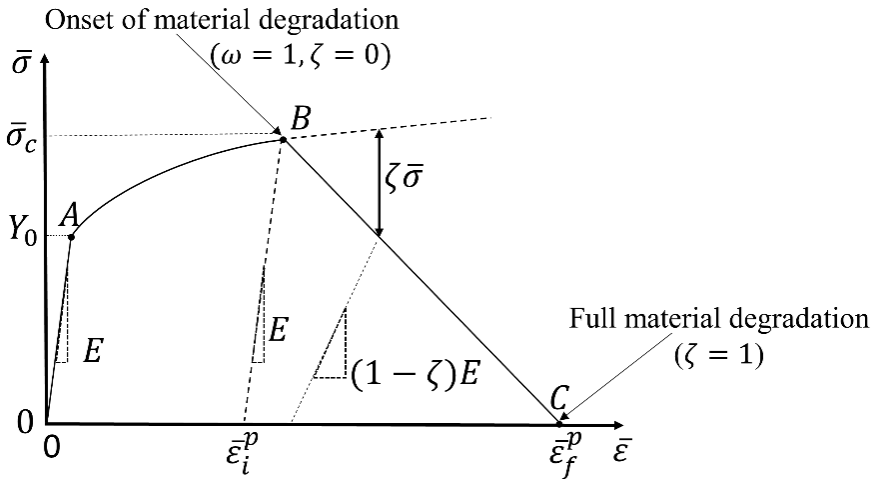

Figure 4.2. Effective stress $\bar{\sigma}$ versus equivalent strain $\bar{\varepsilon}$ diagram illustrating the evolution of damage leading to material degradation.

Modeling of damage accumulation (path AB) and material degradation (path BC) in plastically deformed finite elements required the implementation of a failure criterion. Therefore, the failure criterion proposed by Johnson and Cook (1985) was used in this study, which for quasi-static, isothermal, strain hardening deformation is given by

$$\bar{\varepsilon}_i^p = A + B\, e^{C\eta} \tag{4.4}$$

where A, B, and C are material damage constants and η is a triaxiality parameter, given by $\eta = \sigma_m/\sigma_M$, where σ_m is the hydrostatic stress and σ_M is the von Mises equivalent stress. Table 4.2 gives the material properties and damage constants assigned to the half-space. The mechanical properties given in Table 4.2 are typical of A2024-T351 aluminum alloy, a material widely used in aerospace, automotive, machining, and other industrial applications due to its high strength, low weight, good machinability, and good fatigue resistance (Asad et al., 2014).

For a smooth transition from the fully damaged state (point B) to failure (point C), an approach based on the fracture energy for creating a crack of unit area (Hillerborg et al., 1976) was used in the present analysis. A linear material degradation process (path BC) was modeled using the relation (ABAQUS/CAE 2022, Dassault Systèmes Simulia, Providence, RI):

$$\zeta = \frac{l_c\, \bar{\varepsilon}^p}{2\, G_f}\bar{\sigma}_c \tag{4.5}$$

where l_c is a characteristic length depending on the aspect ratio of finite element sides, G_f is the fracture energy for creating a crack of unit area, and $\bar{\sigma}_c$ is the effective stress at the inception of material degradation, i.e., $\omega = 1$ (point B). To prevent an artificial decrease in energy dissipation due to strain localization resulting from mesh refinement, an element aspect ratio close to unity was selected and l_c was set equal to the square root of the area of the smallest finite elements (region I, Fig. 4.1), i.e., $l_c = 0.0005L$. The degradation parameter ζ was included in the relation $\bar{\sigma}^* = (1-\zeta)\bar{\sigma}$, where $\bar{\sigma}^*$ is the reduced effective stress due to damage accumulation. A finite

element was removed from the FEM model when $\zeta = 1$. The parameter G_f was determined as the area under the true stress-strain curve up to fracture of the A2024-T351 aluminum alloy multiplied by the characteristic length l_c.

Table 4.1 Input parameters of the fractal surface.

Parameter	Magnitude
Sample length, L (nm)	2000
Scaling parameter, γ	1.5
Fractal roughness, G (nm)	$(0.5–75) \times 10^{-4}$
Fractal dimension, D	1.3, 1.4, 1.5
Smallest wavelength, L_0 (nm)	5
Oscillation amplitude, δ (nm)	5

Table 4.2 Material properties and damage parameters used in the FEM simulations.

Parameter	Magnitude
Density, ρ (kg/m^3)	2700[(a)]
Initial yield strength, Y_0 (MPa)	352[(a)]
Elastic modulus, E (GPa)	73[(a)]
Poisson's ratio, ν	0.33[(a)]
Strain hardening coefficient, K (MPa)	440[(a)]
Strain hardening exponent, n	0.42[(a)]
Fracture energy, G_f (N/mm)	0.084

Coefficient of friction, μ	0.1
Damage parameter, A	0.13[(b)]
Damage parameter, B	0.13[(b)]
Damage parameter, C	–1.5[(b)]

[(a)]Asad et al. (2014).
[(b)]Johnson and Holmquist (1989).

4.2.4. Constitutive Model

To model quasi-static, isothermal, isotropic strain hardening material behavior, the half-space was modeled to follow the stress-strain relation (Johnson and Cook, 1985)

$$\bar{\sigma} = Y_0 + K\bar{\varepsilon}^n \tag{4.6}$$

where Y_0 is the initial yield strength, K is the strain hardening coefficient, and n is the strain hardening exponent.

Yielding was determined by the von Mises yield criterion, given by

$$\bar{\sigma} = \left(\frac{3}{2}S_{ij}S_{ij}\right)^{1/2} = Y \tag{4.7}$$

where S_{ij} are components of the deviatoric stress tensor and Y is the current yield strength.

The evolution of plasticity was tracked by the equivalent plastic strain $\bar{\varepsilon}^p$, computed by

$$\bar{\varepsilon}^p = \int_{\Omega} \left(\frac{2}{3}d\varepsilon_{ij}^p d\varepsilon_{ij}^p\right)^{1/2} \tag{4.8}$$

where Ω is the strain path used to track the accumulation of plasticity and $d\varepsilon_{ij}^p$ are plastic strain increments.

4.2.5. Finite Element Simulations

All the FEM simulations were performed in displacement-control mode using the multi-physics code ABAQUS/Explicit (ABAQUS/CAE 2022, Dassault Systèmes Simulia, Providence, RI). Special attention was given to the selection of the time step. When using the explicit solver in a quasi-static analysis, a large time step can yield significant dynamic effects, whereas a smaller time step can greatly increase the computation time. Using a mass scaling factor k_m can reduce the computation time by a factor of $k_m^{1/2}$. To ensure that the selected time step preserved the quasi-static condition, the kinetic energy should be less than 5% of the internal energy. Consequently, a

time step $\Delta t \approx 0.1$ μs that yielded a kinetic energy below the admissible range of internal energy was used in all simulations.

4.2.6. Dimensionless Parameters

To obtain generalized solutions, the input and output simulation parameters were normalized by appropriate quantities. Specifically, the dimensionless fractal roughness was defined by $\bar{G} = G/L$, the dimensionless load $\bar{P}$ was given by P/Y_0L^2, and the normalized equivalent von Mises stress was expressed by $\bar{\sigma}_M = \sigma_M/Y_0$. The material removal (wear) rate was defined by $\bar{A}_r = A_r/LS$, where A_r is the total area of removed (fully damaged) finite elements and S is the total sliding distance traveled by the fractal surface during the simulated oscillation cycles. The plastic work W_p, frictional work W_f, and elastic work W_e were normalized by the external work W_{ex} to obtain the dimensionless parameters $\bar{W}_p$, $\bar{W}_f$, and $\bar{W}_e$, respectively. The normalized maximum penetration depth $\bar{d}_{\max}$ was defined by $d_{\max}/L$, where $d_{\max}$ is the average of all maximum penetration depths encountered in each simulation. The normalized wavelength amplitude of a fractal surface $\bar{\lambda}_n$ was obtained as the ratio of the wavelength λ_n to the sample length L, given by $\bar{\lambda}_n = (G/L)^{(D-1)}/\gamma^{(2-D)n}$ (Eq. (4.1)).

4.3. Results and Discussion

Figure 4.3 shows results of the normalized von Mises equivalent stress $\bar{\sigma}_M$ and the equivalent plastic strain $\bar{\varepsilon}^p$ for $D = 1.4$, $\bar{G} = 2.5 \times 10^{-7}$, and $\bar{P} = 14.2 \times 10^{-5}$, which provide insight into the effect of oscillation cycles on the development of subsurface stresses and plasticity. Normal loading ($N = 0$) produced high stresses immediately below the established microcontacts (Fig. 4.3(a)), resulting in highly localized plasticity (Fig. 4.3(b)). Plastic shearing during the first oscillation cycle ($N = 1$) generated material pile-ups, intensified the subsurface stresses (Fig. 4.3(c)), and enlarged the plastic zones beneath the microcontacts (Fig. 4.3(d)). Moreover, oscillatory sliding increased the penetration depth, resulting in more microcontacts. The increase of plasticity prompted the accumulation of damage in highly deformed elements, triggering the material degradation process (Eq. (4.5)) in the elements with $\omega = 1$ (Eq. (4.3)), ultimately leading to the removal of fully degraded elements ($\zeta = 1$). The loss of material after five oscillation cycles ($N = 5$) increased the number of microcontacts, contributing to the decrease of the concentration and magnitude of the high stresses (Fig. 4.3(e)) and the formation of a highly intensified plastic zone extending along the contact interface (Fig. 4.3(f)). These results revealed that the proliferation of plasticity principally adjacent to the contact interface promoted damage accumulation, causing the removal of several near-surface elements, consecutively increasing the surface conformity.

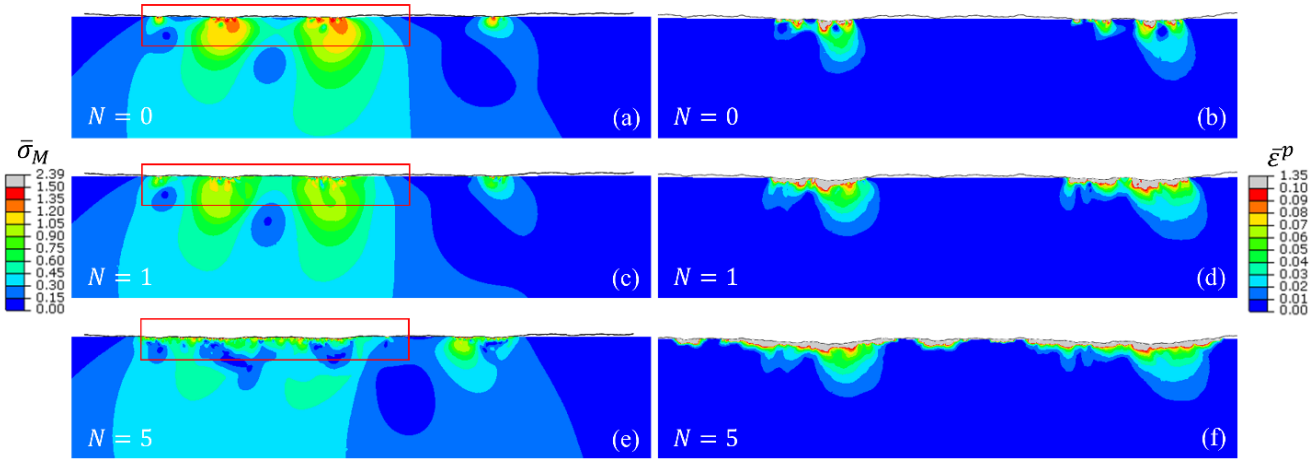

Figure 4.3 Normalized von Mises equivalent stress $\bar{\sigma}_M$ (left) and equivalent plastic strain $\bar{\varepsilon}^p$ (right) for $D = 1.4$, $\bar{G} = 2.5 \times 10^{-7}$, and $\bar{P} = 14.2 \times 10^{-5}$ obtained after (a,b) normal loading ($N = 0$), (c,d) the first oscillation cycle ($N = 1$), and (e,f) the fifth oscillation cycle ($N = 5$). The $\bar{\varepsilon}^p$ contours are within the boxed areas shown on the left.

Simulations with fractal surfaces characterized by different values of the fractal parameters were performed to elucidate the effect of surface texture on the subsurface stress field, the development of plasticity, and the removal of material adjacent to the contact interface due to cumulative damage. Results of the normalized von Mises equivalent stress $\bar{\sigma}_M$ and the equivalent plastic strain $\bar{\varepsilon}^p$ obtained at the end of normal loading ($N = 0$) for $D = 1.3, 1.4$, and 1.5, $\bar{G} = 2.5 \times 10^{-7}$, and $\bar{P} = 14.2 \times 10^{-5}$ are contrasted in Fig. 4.4. It is noted that the increase of the fractal dimension D enhances the dominance of higher frequency components (smaller amplitude wavelengths) in the surface topography; therefore, the higher the value of D the smoother the surface profile. Normal contact of the rougher surface ($D = 1.3$) with the half-space produced multiple microcontacts clustered in two neighboring regions with highly localized stresses (Fig. 4.4(a)) and large plastic strains adjacent to the contact interface accompanied by material flow into the valleys of the fractal surface formed by the shorter wavelengths (Fig. 4.4(b)). The smoother fractal surface ($D = 1.4$) yielded more microcontacts, which produced more localized high stresses and increased interaction of the stress fields of neighboring microcontacts (Fig. 4.4(c)), leading to lower plastic strains and much smaller plastic zones adjacent to the contact interface (Fig. 4.4(d)). The multiple microcontacts formed in the normal contact simulation with the smoothest fractal surface ($D = 1.5$) generated high stresses primarily at the surface (Fig. 4.4(e)) and insignificant plastic deformation within small and spotty near-surface plastic zones (Fig. 4.4(f)).

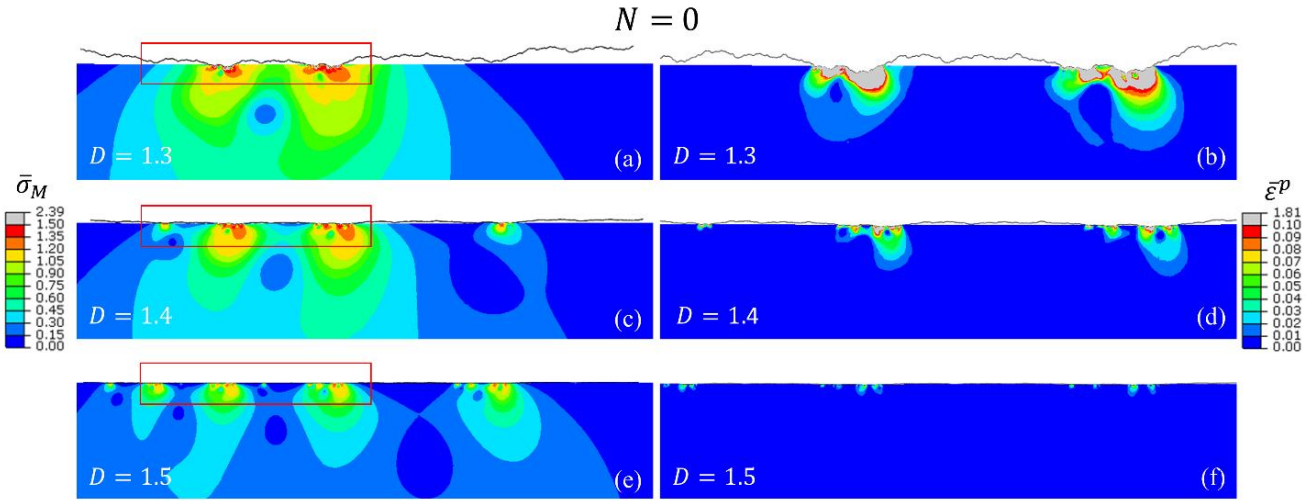

Figure 4.4 Normalized von Mises equivalent stress $\bar{\sigma}_M$ (left) and equivalent plastic strain $\bar{\varepsilon}^p$ (right) for $\bar{G} = 2.5 \times 10^{-7}$ and $\bar{P} = 14.2 \times 10^{-5}$ obtained after normal loading ($N = 0$): (a,b) $D = 1.3$, (c,d) $D = 1.4$, and (e,f) $D = 1.5$. The $\bar{\varepsilon}^p$ contours are within the boxed areas shown on the left.

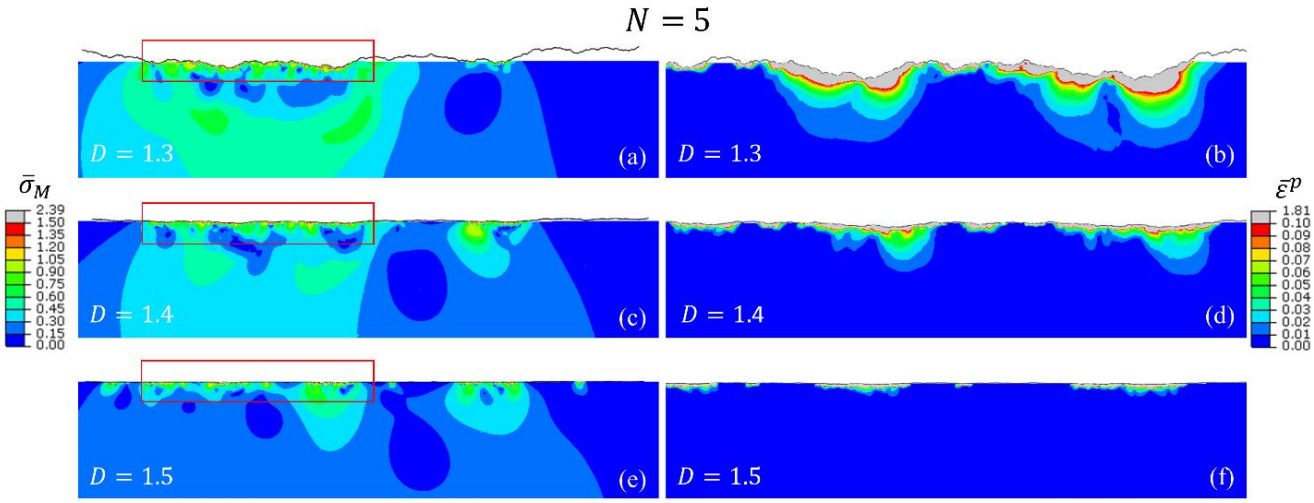

Figure 4.5 Normalized von Mises equivalent stress $\bar{\sigma}_M$ (left) and equivalent plastic strain $\bar{\varepsilon}^p$ (right) for $\bar{G} = 2.5 \times 10^{-7}$ and $\bar{P} = 14.2 \times 10^{-5}$ obtained after five oscillation cycles ($N = 5$): (a,b) $D = 1.3$, (c,d) $D = 1.4$, and (e,f) $D = 1.5$. The $\bar{\varepsilon}^p$ contours are within the boxed areas shown on the left.

Intensification of plasticity and material removal became prominent with oscillatory sliding as demonstrated by $\bar{\sigma}_M$ stress and $\bar{\varepsilon}^p$ strain results displayed in Fig. 4.5, which are for the same contact interface depicted in Fig. 4.4. Specifically, plastic shearing induced by reciprocal sliding enhanced the loss of material, resulting in the establishment of more microcontacts, subsequently decreasing the overall stress field due to augmentation of the surface conformity. Nevertheless, the rougher fractal surface with $D = 1.3$ still produced higher stresses (Fig. 4.5(a)) than the relatively smoother surfaces with $D = 1.4$ (Fig. 4.5(c)) and $D = 1.5$ (Fig. 4.5(e)). Conversely to the stresses, the proliferation of surface conformity due to the loss of material was accompanied by the evolution of plasticity. The rougher surface ($D = 1.3$) produced significantly larger plastic zones and plastic strains (Fig. 4.5(b)), resulting in more damage accumulation in the

elements at and adjacent to the contact interface, which were eventually removed, compared to the smoother surface ($D = 1.4$), which produced more but much smaller interconnected plastic zones (Fig. 4.5(d)). Oscillatory sliding induced plastic deformation even in the case of the smoothest surface ($D = 1.5$), which yielded virtually elastic deformation under normal loading (Fig. 4.4(f)), although plasticity was confined very close to the contact interface (Fig. 4.5(f)). In addition to the effect of the fractal dimension D on the intensity and spatial distribution of $\bar{\varepsilon}^p$, Figs. 4.5(b), 4.5(d), and 4.5(f) also provide a qualitative assessment of the effect of surface texture on the loss of material and the density and interaction of asperity microcontacts. Evidently, the removal of material and plasticity became less prominent with the increase of the fractal parameter D due to the formation of more microcontacts that shared the load more uniformly across the contact interface.

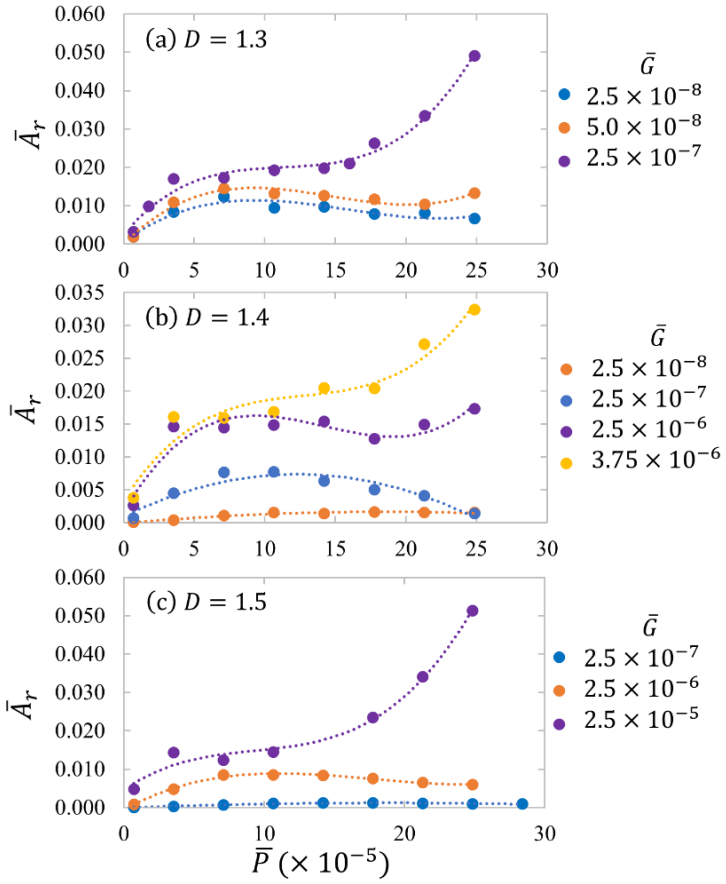

Figure 4.6 Material removal rate $\bar{A}_r$ versus normal load $\bar{P}$ for various values of $\bar{G}$ and (a) $D = 1.3$, (b) $D = 1.4$, and (c) $D = 1.5$.

Further insight into the effect of surface texture on material loss can be obtained in the light of the results displayed in Fig. 4.6, showing the material removal rate $\bar{A}_r$ as a function of normal load $\bar{P}$ for $D = 1.3, 1.4$, and 1.5 and different values of the dimensionless fractal roughness $\bar{G}$. The nonlinear dependence of $\bar{A}_r$ on $\bar{P}$ demonstrated in all simulation cases indicated a divergence from the linear load dependence of the material removal rate postulated by the classical wear law (Archard, 1953). It is also noted that $\bar{A}_r$ increased with the increase of $\bar{G}$ (for fixed D) and the decrease of D (for fixed $\bar{G}$), implying a decrease in material removal rate with decreasing surface

roughness, consistent with the results shown in Figs. 4.4 and 4.5 and the experimental evidence reported in the literature.

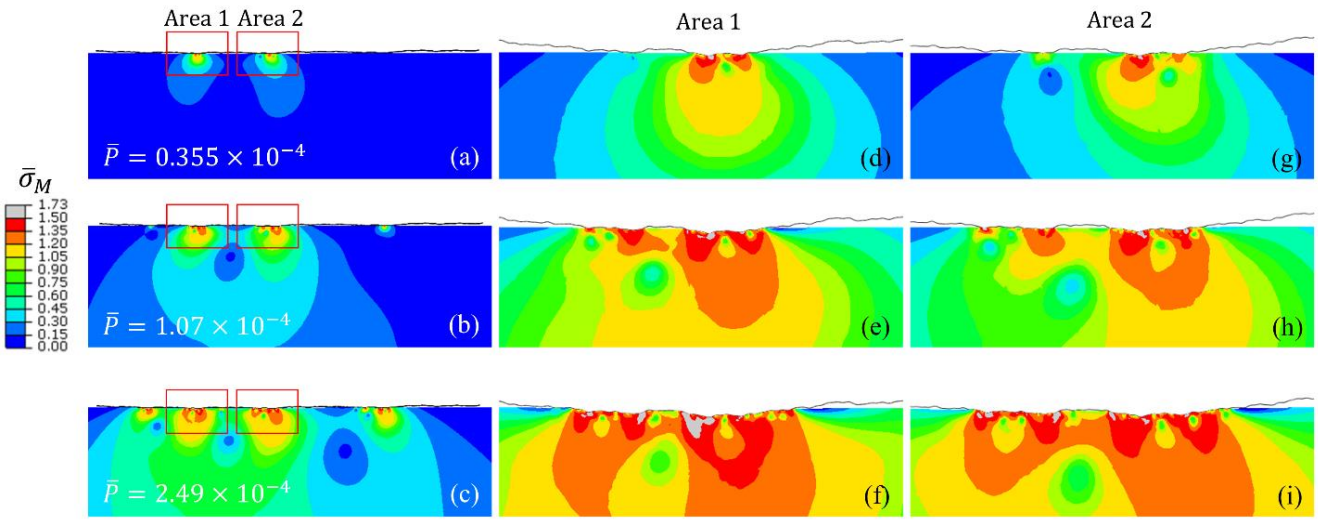

Figure 4.7 Normalized von Mises equivalent stress $\bar{\sigma}_M$ at the end of normal loading for various normal loads $\bar{P}$, $D = 1.4$, and $\bar{G} = 2.5 \times 10^{-7}$. Corresponding magnified stress distributions inside the boxed areas 1 and 2 shown on the left are displayed in the middle and right column, respectively.

Another important finding was the effect of surface roughness on the normal load dependence of the material removal rate. As shown in Fig. 4.6, $\bar{A}_r$ exhibited a bell-shaped distribution for relatively smooth fractal surfaces (i.e., high D and/or low $\bar{G}$) and a sigmoidal distribution for relatively rough fractal surfaces (i.e., low D and/or high $\bar{G}$). This trend can be explained by considering the effects of normal load and fractal parameters on surface conformity. Figure 4.7 shows the normalized von Mises equivalent stress $\bar{\sigma}_M$ at the end of normal loading in terms of the normal load $\bar{P}$ for $D = 1.4$ and $\bar{G} = 2.5 \times 10^{-7}$. Figures 4.7(a)–4.7(c) show the overall stress distribution, whereas Figs. 4.7(d)–4.7(f) and 4.7(g)–4.7(i) display magnified views of corresponding stress distributions close to the contact interface, within the boxed areas 1 and 2, respectively, shown in Figs. 4.7(a)–4.7(c). The load increase amplified the near-surface stresses, enlarged the real contact area, and augmented the surface conformity by inducing material flow into the valleys of the fractal surface (Figs. 4.7(e), 4.7(h), 4.7(f), and 4.7(i)). The progressive proliferation of the surface conformity, instigated by the load increase and the loss of material during sliding, contributed to mechanical interlocking of the fractal surface with the half-space, which strengthened with the accumulation of oscillation cycles, accordingly, reducing the relative slip distance at the contact interface. Thus, the bell-shaped distribution of $\bar{A}_r$ displayed by the relatively smooth surfaces (Fig. 4.6) can be attributed to the increase of $\bar{A}_r$ with $\bar{P}$ in the low-load range. In the high-load range, material plastic flow into the valleys of the fractal surface enhanced the surface conformity, resulting in mechanical interlocking, which decreased the relative slip distance of the fractal surface during oscillation and, sequentially, the material removal rate. The sigmoidal distribution of $\bar{A}_r$ demonstrated by the relatively rough fractal surfaces (Fig. 4.6) was also accredited to the increase of surface conformity due to plastic flow of material into the valleys of the fractal surface that resulted in mechanical interlocking. Similar to the trend for the smoother fractal surfaces, the increase of $\bar{A}_r$ with $\bar{P}$ for the rougher surface in the low-load range was due to the deeper penetration of the fractal surface. The intermediate-load range of nearly stable or slowly

changing $\bar{A}_r$ was ascribed to small changes in the relative slip distance due to small variations in the saturation of the surface valleys (i.e., the smaller wavelengths of the rough surface) by inflowing material. Finally, the increase of $\bar{A}_r$ in the high-load range was again due to the increase of the penetration depth of the fractal surface, attributed to the contribution of the larger wavelengths of the rougher surface. However, because the much larger surface valleys of the rough fractal surfaces were not fully occupied by plastically flowing material, the effect of the surface conformity and associated mechanical interlocking on the relative slip distance during oscillation was secondary; therefore, the consequence on the loss of material was not prominent in the high-load range.

Additional insight into the effects of normal load and contact interface topography on the material removal rate was obtained by considering the variation of the normalized elastic, plastic, and frictional work, $\overline{W}_e$, $\overline{W}_p$, and $\overline{W}_f$, respectively, with the normal load and fractal dimension. Simulations revealed different trends for $\overline{W}_e$ and $\overline{W}_p$ with increasing oscillation cycles and normal load for fixed $\bar{G}$ and $D = 1.3$ and 1.4. For the rougher fractal surface ($D = 1.3$), $\overline{W}_p$ was always dominant despite the increase of $\overline{W}_e$ with the oscillation cycles (Fig. 4.8), consistent with the evolution of $\bar{A}_r$ with the increase of the normal load for $\bar{G} = 2.5 \times 10^{-7}$ shown in Fig. 4.6(a). However, for the smoother fractal surface ($D = 1.4$), $\overline{W}_p$ was prevalent in the low-load range, whereas $\overline{W}_e$ became influential in the high-load range (Fig. 4.9). Since the loss of material depended on the plastic work, the foregoing results indicated that the decrease of $\bar{A}_r$ in the high-load range of the relatively smooth fractal surface, as shown in Fig. 4.6(b) for $\bar{G} = 2.5 \times 10^{-7}$, was due to the diminishment of the relative slip distance at the contact interface, instigated by the interlocking of the fractal surface with the half-space.

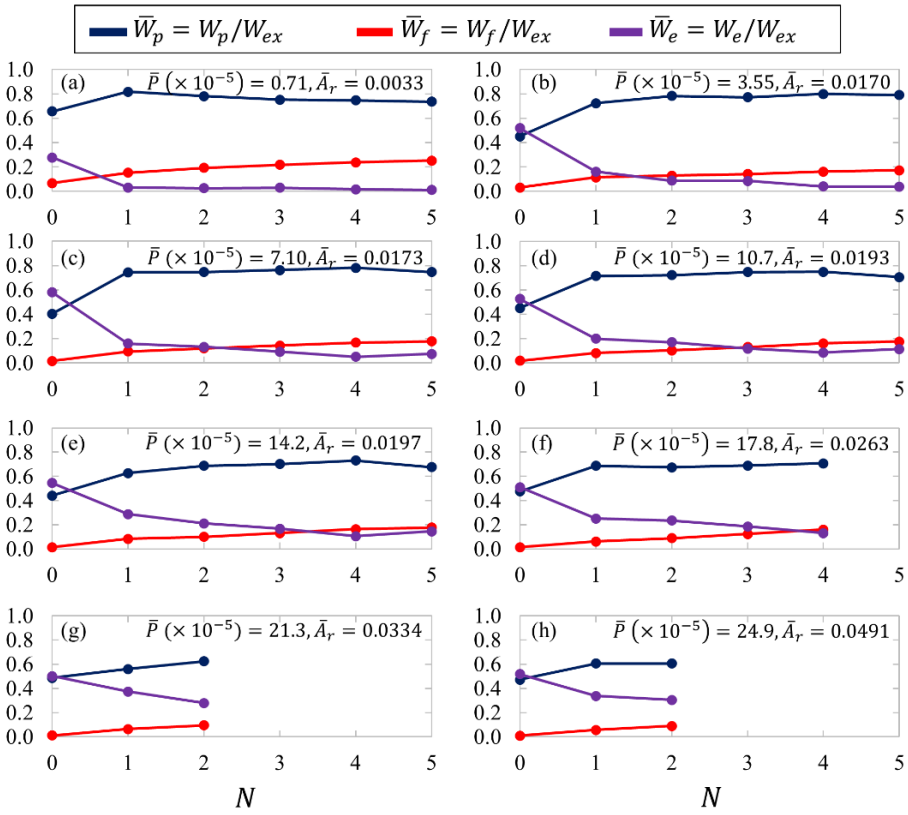

Figure 4.8 Normalized plastic work $\bar{W}_p$, frictional work $\bar{W}_f$, and elastic work $\bar{W}_e$ versus oscillation cycles N and normal load $\bar{P}$ for $D = 1.3$ and $\bar{G} = 2.5 \times 10^{-7}$. The normalized material removal rate $\bar{A}_r$ computed for the maximum cycle number is also shown for each simulation case.

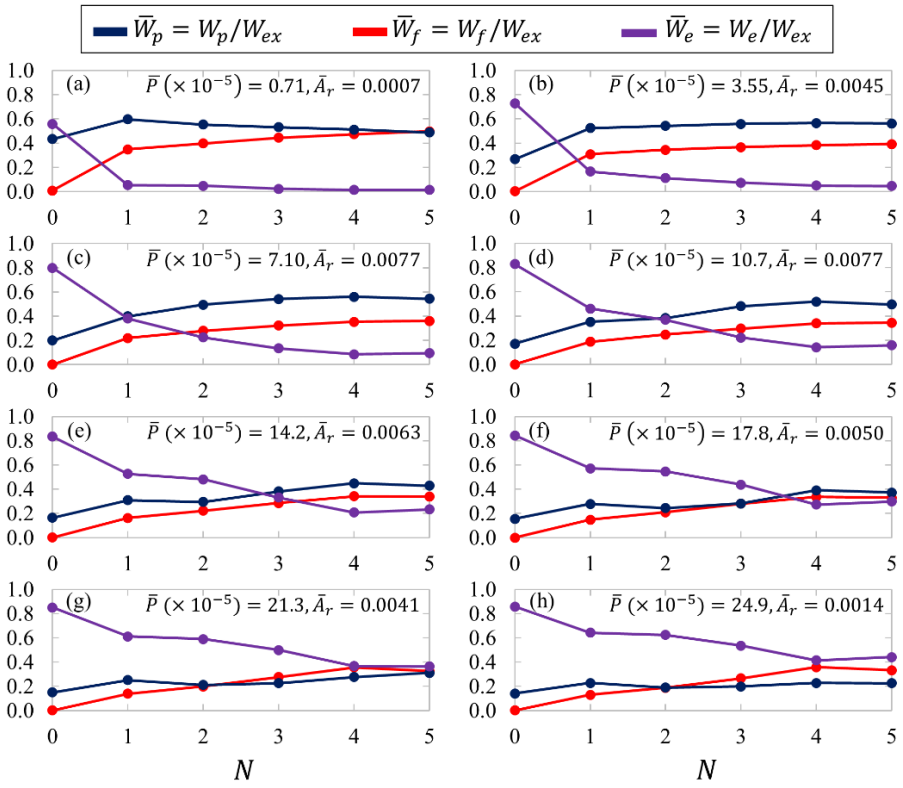

Figure 4.9 Normalized plastic work $\bar{W}_p$, frictional work $\bar{W}_f$, and elastic work $\bar{W}_e$ versus oscillation cycles N and normal load $\bar{P}$ for $D = 1.4$ and $\bar{G} = 2.5 \times 10^{-7}$. The normalized material removal rate $\bar{A}_r$ computed for the maximum cycle number is also shown for each simulation case.

To further elucidate the dependence of surface conformity and interface interlocking on the normal load and contact interface topography, results of the normalized maximum penetration depth $\bar{d}_{\max}$ for a given normal load $\bar{P}$ were compared with the range of normalized wavelength amplitudes $\bar{\lambda}_n$ comprising the fractal surfaces. Figure 4.10 shows $\bar{d}_{\max}$ as a function of $\bar{P}$ for $D = 1.3$, 1.4, and 1.5 and $\bar{G} = 2.5 \times 10^{-7}$. All simulations demonstrated a similar monotonic increase of $\bar{d}_{\max}$ with $\bar{P}$ and a noticeable upsurge of $\bar{d}_{\max}$ with decreasing D for fixed $\bar{P}$. Although the penetration depth at several microcontacts was less than $\bar{d}_{\max}$, the data shown in Fig. 4.10 can be used to approximately interpret the effect of fractal dimension and normal load on the surface conformity and, in turn, further elucidate the nonlinear variation of the material removal rate (Fig. 4.6). The normalized wavelength amplitudes $\bar{\lambda}_n$ corresponding to the fractal surfaces with $D = 1.3$, 1.4, and 1.5 are in the ranges $[1.48 \times 10^{-4}, 1 \times 10^{-2}]$, $[5.95 \times 10^{-5}, 2.3 \times 10^{-3}]$, and $[2.4 \times 10^{-5}, 5 \times 10^{-4}]$, respectively. Comparing the ranges of $\bar{\lambda}_n$ with the values of $\bar{d}_{\max}$ shown in Fig. 4.10, it can be seen that, for $D = 1.5$ and 1.4, $\bar{d}_{\max}$ exceeded the maximum $\bar{\lambda}_n$ at $\bar{P} \approx 2.5 \times 10^{-5}$ (Fig. 4.10(c)) and 4.5×10^{-5}(Fig. 4.10(b)), respectively, whereas for $D = 1.3$, the maximum $\bar{\lambda}_n$ was just attained at the highest normal load (Fig. 4.10(a)). These results provided further support to the assessment that the narrow surface valleys of the smoother fractal surfaces ($D = 1.4$ and 1.5) entailing small wavelengths were prematurely filled with plastically flowing material of the half-space, which, sequentially, enhanced the surface conformity, promoted surface interlocking, and reduced relative slip at the contact interface and, as a result, reduced the material removal rate. Alternatively, the effect of material filling of the surface valleys of the rougher fractal surface ($D =$

1.3) possessing a wider range of wavelength amplitudes on surface conformity was considerably less pronounced. Consequently, the accumulation of significantly more plastic deformation due to less restriction of relative slip at the contact interface yielded higher material removal rates for the rougher fractal surface. The foregoing explains the bell-shape and sigmoidal distributions of the material removal rate (Fig. 4.6).

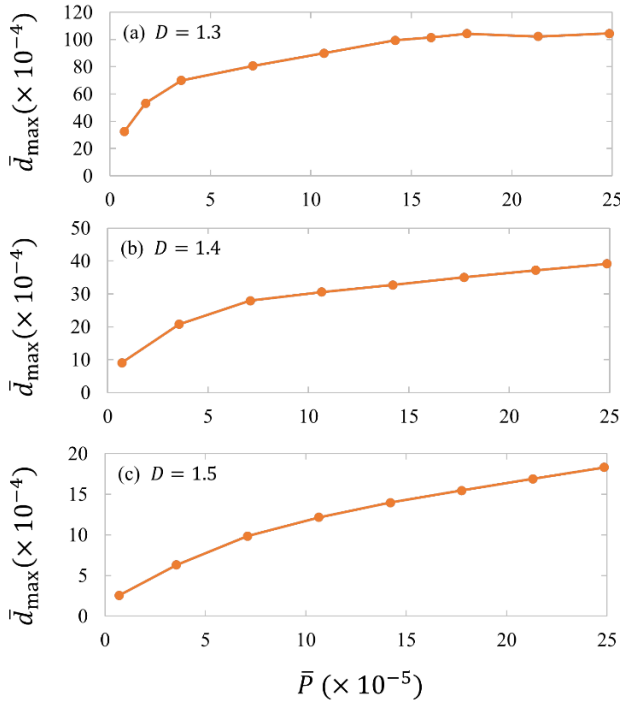

Figure 4.10 Normalized maximum penetration depth $\bar{d}_{\max}$ averaged over the total accumulated oscillation cycles of each simulation versus normal load $\bar{P}$ for $\bar{G} = 2.5 \times 10^{-7}$ and (a) $D = 1.3$, (b) $D = 1.4$, and (c) $D = 1.5$.

The present contact mechanics analysis of oscillatory sliding contact provided insight into the role of fractal parameters, normal load, and oscillation cycles in the development of subsurface stresses and plastic deformation and the dependence of the material removal (wear) rate on plasticity-induced damage accumulation. A novel finding was that the classical wear law (Archard, 1953), postulating a linear dependence of wear rate on normal load, not only breaks down at the atomic scale but also at the continuum level when the contact interface topography exhibits self-affinity. Another important result of the present analysis was that relative slip at the contact interface may diminish under certain conditions, depending on the applied normal load, surface topography, and loss of material. The computational mechanics approach developed in this study can be modified to include a constitutive law accounting for the effects of strain rate and frictional heating (e.g., the complete ductile failure criterion developed by Johnson and Cook (1985)) on plasticity-induced damage, leading to the loss of material at sliding surfaces exhibiting multi-scale roughness.

4.4. Conclusions

A contact mechanics analysis of the effects of surface topography (fractal) parameters, normal load, and oscillation cycles on plasticity-induced damage leading to progressive damage and loss of material in oscillatory contacts was performed in this study. A plane-strain FEM model of a rigid fractal surface in reciprocating sliding contact with an elastic-plastic, strain hardening half-space was used to analyze the removal of material with the development of damage. Based on the presented results and discussion, the following main conclusions can be drawn from this study.

(1) For a given set of fractal parameters, the subsurface stresses relaxed with the accumulation of oscillation cycles due to the increase of the contact area (surface conformity) with the normal load and the removal of material; however, plastic deformation extended along the contact interface forming a continuous plastic band.
(2) The subsurface stresses and plastic strains intensified with the decrease of fractal dimension (i.e., increase of surface roughness) and the accrual of oscillation cycles.
(3) The material removal rate exhibited a nonlinear dependence on normal load, indicating a departure from the classical linear wear law postulated by Archard (1953), even at the continuum level when the contact interface topography demonstrates self-affinity.
(4) The material removal rate increased with the increase of fractal roughness and the decrease of fractal dimension, indicating a decreasing trend of wear rate with surface smoothening.
(5) The nonlinear variation of the material removal rate with the normal load and fractal parameters was associated with the surface conformity and resulting mechanical interlocking of the fractal surface with the half-space surface, which reduced the loss of material by limiting relative slip at the contact interface.

The contribution of this study to the contact mechanics field is the establishment of a computational capability for investigating the effects of other important parameters, such as strain rate, oscillation amplitude, and frictional heating, on the development of plasticity-induced damage leading to the loss of material in mechanical devices operating in reciprocating sliding contact mode.

CHAPTER 5

A cohesive-zone-based contact mechanics analysis of delamination in homogeneous and layered half-spaces subjected to normal and shear surface tractions

5.1. Introduction

Delamination is commonly observed in multilayered structures used in various applications, such as semiconductor devices (Kim et al., 2022), electronics packaging (Morris, 2022), plastic packaging (Ügdüler et al., 2021), high-performance capacitors (Ko et al., 2010), sliding wear (Suh, 1973; Voevodin et al., 1996), cutting tools (Cho and Komvopoulos, 1997; Tabakov et al., 2017), thermal barrier coatings for turbines (Choi et al., 1999) and automotive engines (Murthy et al., 1990), and high-temperature materials (Nagarathnam and Komvopoulos, 1993). This phenomenon is controlled by an interfacial cohesive strength toughness parameter which, together with the mechanical properties of the layer and substrate materials, controls the inception of failure. Low interfacial cohesive strength can lead to layer delamination, thereby not serving the desired purpose of preserving the integrity of the substrate and close-fitting design tolerances. A layered structure may also evolve from an initially uniform structure during fabrication and/or usage. A characteristic example is the development of a strain-hardened surface layer on the surface of a machined part or a load bearing component. Therefore, even an initially homogeneous structure can become a layered structure during fabrication and/or usage. Consequently, basic understanding of interfacial delamination prompted by the mismatch of the layer and substrate physical properties is critical to the reliability and functionality of structures subjected to thermomechanical loadings.

Various experimental and computational methods have been used to study interfacial delamination in layered structures. Gerberich et al. (1999) identified five sequential stages of plasticity and interface fracture due to nanoindentation, resulting in layer decohesion from the substrate (delamination). It was reported that activation of dislocations followed by hardening and material pile-up around the nanoindenter were the precursors of plasticity-induced delamination at the layer/substrate interface. He et al. (2011) designed a test method for measuring the delamination toughness of bilayer coatings attached to non-planar components, which was guided by beam-theory solutions of the energy release rate and structure compliance. In addition, they used the finite element method (FEM) to study the effect of residual stress on the energy release rate and determined that the shear-to-normal stress ratio was highly dependent on the layer thickness and the modulus ratio of the two layers comprising the bilayer coating. Liu and Yang (2012) performed a FEM analysis of interfacial delamination in an indented stiff layer/compliant substrate system and obtained numerical results showing that both the delamination zone and the maximum nodal separation increased with the indentation depth and the decrease in layer thickness.

Significant advancements in fundamental understanding of interfacial delamination have been achieved by implementing cohesive constitutive laws in FEM analysis. The concept of a cohesive zone model (CZM), proposed by Dugdale (1960) and Barenblatt (1962), has been widely used to analyze localized damage or plastic flow in the close proximity of crack tips. Subsequently, various cohesive zone laws (in the form of interface traction-separation relationships accounting for elastic and softening deformation prior to final failure) were integrated in analyses of crack initiation and growth and interfacial fracture. Alfano et al. (2009) performed a comparative study of various CZMs used to model the instigation of interfacial cracking and delamination.

The integration of CZMs in FEM studies provided an effective computational methodology for undertaking complex interface problems in layered structures. For instance, Yan and Shang (2009) demonstrated the use of different CZMs in FEM simulations of interfacial fracture of micrometer-thick films, showing that the cohesive strength and work of separation are the most dominant parameters in CZMs. Song and Komvopoulos (2013) used a CZM that obeyed a bilinear traction-separation constitutive law to model the layer/substrate interface in a FEM analysis of adhesive contact between a rigid sphere and an elastic film attached to an elastic-perfectly plastic substrate and obtained numerical solutions that provided insight into the evolution of interfacial delamination during a full load-unload cycle. Mróz and Mróz (2015) presented a CZM-based analytical study of progressive delamination in bilayer systems subjected to pure shear loading, which shed light into the mode of delamination, the effect of material properties on the damage process, the critical interface stress, and the fracture energy. Walter et al. (2016) used different fracture mechanic methods to study the adhesive strength of a polyimide passivation layer on copper-film stacks deposited on a silicon substrate and the dependence of the critical energy release rate on the mode of loading and evaluated the delamination data using both analytical models and CZM-FEM analysis.

More recently, Lin et al. (2017) used a combined approach based on molecular dynamics (MD) simulations and CZM-FEM analysis to study the interfacial fracture energy and delamination in multilayered integrated circuit packaging. Specifically, critical material parameters, such as the interfacial fracture energy, used in the interfacial cohesive constitutive law were derived from the MD simulations and were then input in the FEM model to analyze interfacial delamination in the multilayered structure due to indentation loading. Soroush et al. (2018) developed an FEM model of interlaminar and intralaminar delamination damage in laminated composite plates subjected to impact using a CZM and a progressive damage model. Hassan et al. (2019) introduced the interfacial strength and fracture toughness of a steel-steel bilayer sheet measured from a peel-off test into a CZM-FEM model to study interfacial delamination in the bilayer sheet caused by normal loading and provided experimental evidence showing more accurate estimates of delamination damage growth obtained with a liner-exponential traction-separation softening law than a linear softening law. Long et al. (2019) used a CZM-FEM approach to investigate the failure characteristics of bi-material systems in uniaxial tension and observed a transition from coating cracking to interface delamination with increasing coating thickness. Liang et al. (2021) performed a CZM-FEM analysis of damage and fracture at the interfaces of ceramic films and metal substrates under uniaxial tensile loading and reported a dependence of the interface strength on both the residual radial force and the axial pressure and a catastrophic failure for thicker films.

Although the foregoing studies (and several others) greatly contributed to the elucidation of various challenging problem in interface mechanics, further research is needed to elucidate interface delamination in elastic-plastic homogeneous and layered media subjected to normal and shear (frictional) surface tractions. Consequently, the purpose of this study was to provide additional insight into interfacial delamination in half-spaces subjected to indentation and sliding contact loading. To accomplish this objective, a CZM was incorporated in a FEM analysis to simulate interface separation when appropriate fracture energy conditions were satisfied. Simulation results revealing the evolution of subsurface stresses and plasticity illuminate the effects of indentation depth and sliding distance on interfacial delamination in homogeneous and layered half-spaces with different elastic-plastic properties, interfacial cohesive strength, and layer

thickness. The present study elucidates the important role of elastic-plastic property mismatch at the layer/substrate interface of layered half-spaces and provides a modeling framework for analyzing interfacial delamination in multilayered structures subjected to quasistatic and dynamic contact loadings.

5.2. Modeling Approach

5.2.1. Finite Element Model

Figure 5.1 shows a schematic of the plane-strain contact model of a rigid cylinder with a radius R sliding against a deformable layered half-space examined in this study. The cylinder indents the half-space up to a maximum depth d and then slides laterally by a total distance s. The half-space comprises a surface layer with a thickness $h = 0.1R$ and a half-space substrate and is discretized by an $8R \times 8R$ FEM mesh consisting of 36,162 four-node, reduced-integration, quadrilateral finite elements with a total of 37,658 nodes. The layer/substrate interface comprises pairs of nodes initially having the same coordinates. To accurately capture the large stress/strain gradients adjacent to the contact interface and the separation at the layer/substrate interface and to reduce the computational time, the mesh is compartmentalized in three segments centered at the point O of initial contact. The near-surface region of the mesh with dimensions $2h = 0.2R$ and $l = 2.2R$ is uniformly refined with elements having a size $l_c = 0.005R$, representing ~ 49% of the total number of elements, of which half are layer elements and the other half are substrate elements (inset of Fig. 5.1). Outside of this region, the substrate is meshed with elements with size gradually increasing from $0.005R$ to $0.1R$. Finally, the outer part of the mesh is uniformly meshed with $0.1R$ size elements. The nodes at the bottom boundary of the mesh are constrained in both x- and y-directions, whereas the nodes at the left and right boundaries of the mesh are not constrained. All the FEM simulations comprised three sequential phases, i.e., indentation of the half-space by the rigid cylinder to a depth d, sliding of the cylinder against the half-space in the x-direction by a distance s, and, finally, full unloading of the cylinder.

Surface contact is simulated with a finite sliding algorithm, which treats the surfaces of the deformable half-space and the rigid cylinder as slave and master surfaces, respectively, and controls the relative separation and slip between the interacting surfaces. Each slave node coming into contact with the master surface is constrained to slide against the master surface, while the position of the slave node relative to the master surface is continuously tracked by the algorithm during the deformation. The finite sliding algorithm was implemented in the FEM analysis by using automatically generated contact elements. At each integration point of a contact element, the overclosure is adjusted to prevent a surface point of the deformed layer surface from penetrating the surface of the rigid cylinder and the relative shear slip is computed afterwards. Coulomb friction is modeled by assigning to the contact elements a coefficient of friction, which relates the maximum allowable shear stress at the contact interface to the local contact pressure. All simulations were performed in displacement-control mode, using the multi-physics code ABAQUS/Standard (implicit solver)(ABAQUS Analysis User's Guide, 2022) .

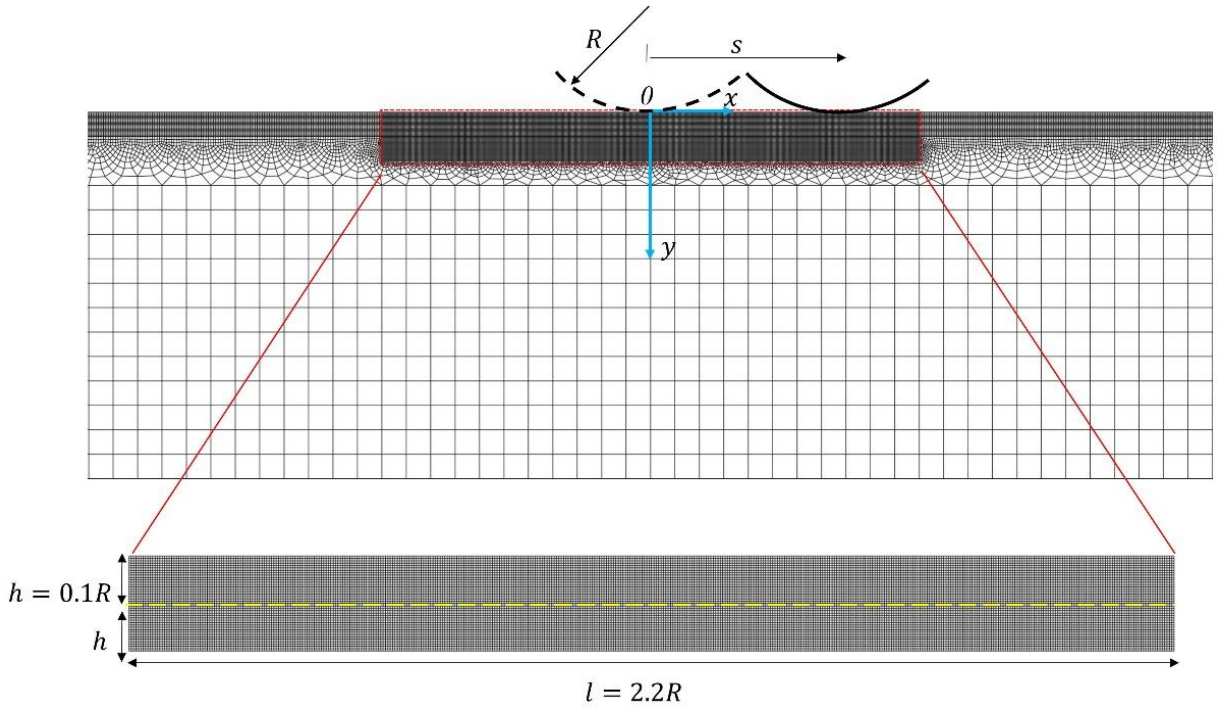

Figure 5.1 Finite element mesh (top) and refined mesh adjacent to the contact interface (bottom) (The yellow dashed line corresponds to the delamination interface and the layer/substrate interface.)

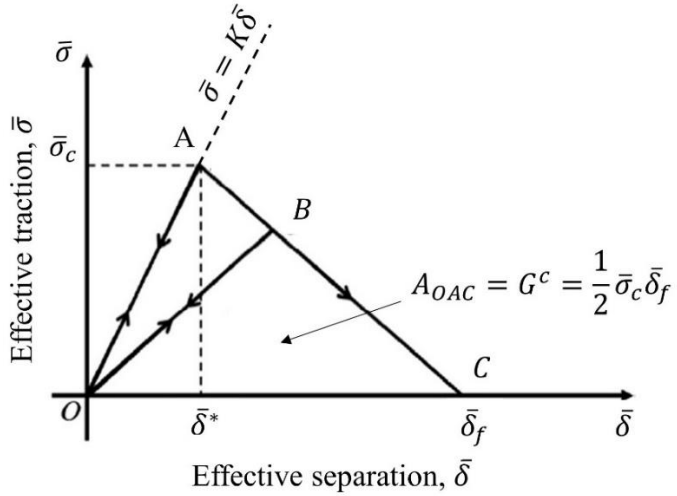

Figure 5.2 The cohesive model of the effective traction $\bar{\sigma}$ versus effective separation $\bar{\delta}$ at the delamination interface.

5.2.2. Cohesive Zone Model and Interfacial Delamination

Interfacial delamination under combined normal and tangential loading is modelled with the surface-based CZM for mixed-mode loading depicted in Fig. 5.2. The CZM relates the effective cohesive interface traction $\bar{\sigma}$ to the effective separation $\bar{\delta}$ at the interface through the following linear relation (Camanho et al., 2003):

$$\bar{\sigma} = k\bar{\delta} = \sqrt{\delta_n^2 + \delta_s^2} \tag{5.1}$$

where k is the initial stiffness (a penalty parameter not representative of a physical quantity), and δ_n and δ_s are the relative separation distances in the normal and tangential directions, respectively. Ideally, the initial stiffness should be infinite so that it does not affect the overall compliance of the model in the OA path; however, a finite stiffness value must be used to avoid numerical errors (ABAQUS Analysis User's Guide, 2022; Turon et al., 2007). Preliminary simulations revealed that $k = 106$ MPa/mm was a good choice for the present analysis; therefore, this stiffness value was used for both the normal and the tangential nodal displacements at the layer/substrate interface.

When the peak value of the applied traction is reached (point A), the interface stiffness begins to degrade according to a damage initiation criterion. Various criteria of damage initiation have been proposed, such as the maximum nominal stress and quadratic nominal stress criteria. A comparative study Rocha and Campilho (2018) has shown better agreement between experimental and FEM results based on the quadratic nominal stress criterion for damage initiation. According to this damage initiation criterion, interfacial delamination is instigated when the following traction-based relation is satisfied (Camanho et al., 2003):

$$\left(\frac{\langle t_n \rangle}{\sigma_c}\right)^2 + \left(\frac{t_s}{\tau_c}\right)^2 = 1 \tag{5.2}$$

where t_n $(= k\delta_n)$ and t_s $(= k\delta_s)$ are the interface tractions in the normal and tangential directions, and σ_c and τ_c are the critical cohesive normal and tangential tractions, assumed equal in this study. The Macaulay bracket (< >) is used in Eq. (5.2) to indicate that a purely compressive stress state does not initiate damage.

In mixed-mode loading, the critical separation distance $\bar{\delta}_c$ (point A) at which Eq. (5.2) is satisfied is given by

$$\bar{\delta}_c = \left(\frac{\sigma_c}{k}\right)\left(\frac{\tau_c}{k}\right)\left[\frac{1+\gamma^2}{\left(\frac{\tau_c}{k}\right)^2 + \gamma^2\left(\frac{\sigma_c}{k}\right)^2}\right]^{1/2} \tag{5.3}$$

where g is the ratio of the shear displacement δ_s to the normal displacement δ_n of node pairs, which are derived from Eq. (5.2) and the traction-displacement stiffness relations. Equations (5.2) and (5.3) are used to determine the initiation of delamination.

Stiffness degradation is represented by a linear softening behavior (path AC in Fig. 5.2) obeying the relation

$$\bar{\sigma} = \bar{\sigma}^*(1 - D) \tag{5.4}$$

where $\bar{\sigma}$ is the current effective interface cohesive strength, $\bar{\sigma}^*$ is the effective interface cohesive strength in the absence of damage, and D is a scalar degradation parameter, given by

$$D = \frac{1 - \bar{\delta}_c/\bar{\delta}}{1 - \bar{\delta}_c/\bar{\delta}^f}, \quad 0 \le D \le 1 \tag{5.5}$$

where $\bar{\delta}^f$ is the effective separation distance corresponding to the fully degraded stiffness (point C).

The area under the traction-separation response (OAC) is equal to the critical fracture energy G^c. For a substrate much thicker than the layer, the critical fracture energy in the normal and tangential interface directions G_n^c and G_s^c, respectively, are given by (Krenk, 1992; Freund and Suresh, 2004)

$$G_n^c = \frac{1}{2}\left(\frac{h}{E'}\right)\sigma_c^2 \tag{5.6}$$

$$G_s^c = \frac{1}{2}\left(\frac{h}{G}\right)\tau_c^2 \tag{5.7}$$

where h is the layer thickness, E' is the effective elastic modulus, and G is the shear modulus.

Under mixed-mode loading, the stiffness degradation and $\bar{\delta}^f$ depend on the following fracture energy-based criterion (Camanho et al., 2003):

$$\frac{G_n}{G_n^c} + \frac{G_s}{G_s^c} = 1 \tag{5.8}$$

where G_n and G_s are the fracture energies in the normal and shear (lateral) directions of the layer/substrate interface given by

$$G_n = \frac{k\bar{\delta}_c\bar{\delta}^f}{2(1+\gamma^2)} \tag{5.9}$$

$$G_s = \frac{k\bar{\delta}_c\bar{\delta}^f\gamma^2}{2(1+\gamma^2)} \tag{5.10}$$

Substitution of Eqs. (5.9) and (5.10) into Eq. (5.8) yields the following expression for $\bar{\delta}^f$,

$$\bar{\delta}^f = \frac{2(1+\gamma^2)}{\left(\frac{1}{G_n^c} + \frac{\gamma^2}{G_s^c}\right)k\bar{\delta}_c} \tag{5.11}$$

Accordingly, Eq. (5.11) is used to determine failure due to delamination.

FEM simulations that use CZMs often encounter convergence difficulties at the instant of node separation at the delamination interface, known to evolve from an elastic snap-back instability commencing as soon as the stress reaches the interface cohesive strength. This convergence problem can be avoided by introducing a small fictitious viscosity in the CZM that is

used to characterize the delamination interface (Gao and Bower, 2004). Consequently, a small viscous dissipation parameter equal to 0.001, which resulted in negligibly small energy dissipation, is introduced into the CZM to prevent instabilities due to the node separation at the delamination interface.

5.2.3. Constitutive Model

To model quasistatic, isothermal, isotropic strain hardening material behavior, the half-space is modelled to obey the following constitutive law:

$$\sigma = E\varepsilon \ \ (\sigma < Y)\ ,\ \ \sigma = K\varepsilon^n \ (\sigma \geq Y) \tag{5.12}$$

where σ is the true stress, ε is the true strain, E is the elastic modulus, Y is the yield strength, K is the strength coefficient, and n is the strain hardening exponent (assumed equal to 0.2 in this study).

Yielding is determined by the von Mises equivalent stress σ_{eq} yield criterion, given by

$$\sigma_{\mathrm{eq}} = \left(\frac{3}{2}S_{ij}S_{ij}\right)^{1/2} = Y \tag{5.13}$$

where S_{ij} are components of the deviatoric stress tensor.

The development of plasticity is traced by the equivalent plastic strain $\varepsilon_{\mathrm{eq}}^{\mathrm{p}}$, calculated by

$$\varepsilon_{\mathrm{eq}}^{\mathrm{p}} = \int_{\Omega} \left(\frac{2}{3}d\varepsilon_{ij}^{\mathrm{p}}d\varepsilon_{ij}^{p}\right)^{1/2} \tag{5.14}$$

where Ω is the strain path used to track the accumulation of plasticity and $d\varepsilon_{ij}^{\mathrm{p}}$ are plastic strain increments.

5.2.4. Dimensionless parameters

To obtain generalized solutions, both input and output parameters are normalized by appropriate quantities. Specifically, the dimensionless indentation depth $\bar{d}$, sliding distance $\bar{s}$, and layer thickness $\bar{h}$ are defined by d/R, s/R, and h/R, respectively. This normalization of the foregoing dimensional parameters is appropriate because the cylinder radius represents the relevant length scale of the problem. In fact, the ratio d/R has been used to represent global deformation in numerous contact mechanics studies. The delamination fraction α is defined as the number of separated node pairs at the layer/substrate interface divided by the total number of interface node pairs. The delamination ratio β is given as α_l/α_h, where α_l and α_h are the delamination fractions of a layered half-space with different layer properties and a homogeneous half-space with substrate properties, respectively. The elastic modulus ratio is defined as the ratio of the elastic modulus of the layer E_l divided by that of the substrate E_s, i.e., $\bar{E} = E_l/E_s$. Similarly, the yield strength ratio is defined as the yield strength of the layer Y_l divided by that of the substrate Y_s, i.e., $\bar{Y} = Y_l/Y_s$. Thus, the values of the dimensionless parameters$\bar{E}$ and $\bar{Y}$ are indicative of the mismatch between the layer and substrate mechanical properties.

5.3. Results and Discussion

Interfacial decohesion (delamination) in a homogeneous elastic-plastic half-space is discussed first to establish a reference for the effects of normalized parameters, such as sliding distance $\bar{s}$ and indentation depth $\bar{d}$, and the interface cohesive strength σ_c on interfacial delamination in a layered elastic-plastic half-space with varying elastic-plastic properties and layer thickness.

5.3.1. Delamination in Homogeneous Half-Spaces

The dependence of the effective nodal separation $\bar{\delta}$ at the cohesive interface before and after unloading on the sliding distance $\bar{s}$ and indentation depth $\bar{d}$ for a homogeneous elastic-plastic half-space can be interpreted considering the results displayed in Fig. 5.3. For a short sliding distance ($\bar{s} = 0.1$), interfacial delamination is confined within a short distance from the center of indentation ($x/w = 0$), with unloading inducing a slight increase in effective nodal separation (Fig. 5.3(a)). For a fixed indentation depth ($\bar{d} = 0.002$), a longer sliding distance ($\bar{s} = 0.3$) results in a profound increase in both the delamination length and the effective nodal separation, especially after unloading (Fig. 5.3(b)). Although the unloading does not affect the delamination length, it enhances the effective nodal separation, particularly with the increase of the sliding distance. A similar trend is observed with the increase of the indentation depth ($\bar{d} = 0.0025$) (or load) for a fixed sliding distance ($\bar{s} = 0.1$) (Fig. 5.3(c)).

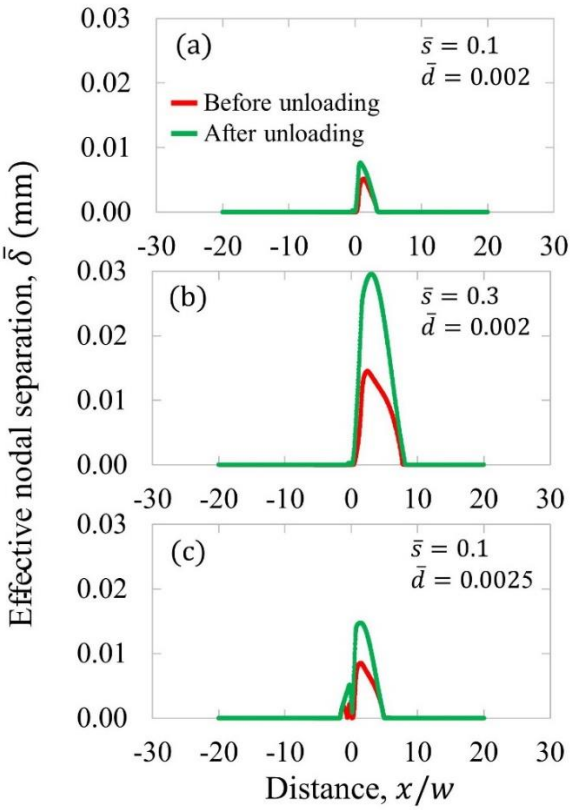

Figure 5.3 Effective nodal separation $\bar{\delta}$ profiles at the delamination interface ($\bar{h}$ = 1) obtained (—) before and (—) after unloading versus distance *x*/*w* measured from the center of initial contact (*x*/*w* = 0) for a homogeneous elastic-plastic half-space with $E = 100$ GPa, $Y = 200$ MPa, and $\sigma_c = 100$ MPa: (a) $\bar{s} = 0.1$, $\bar{d} = 0.002$, (b) $\bar{s} = 0.3$, $\bar{d} = 0.002$, and (c) $\bar{s} = 0.1$, $\bar{d} = 0.0025$.

The dependence of the delamination fraction α on the sliding distance $\bar{s}$, cohesive strength σ_c, and indentation depth $\bar{d}$ is illustrated in Fig. 5.4. In all cases, the delamination fraction increases monotonically with sliding distance. The simulations reveal two different tendencies. For a fixed indentation depth ($\bar{d} = 0.002$), a profound decrease in the delamination fraction occurs with increasing cohesive strength, because more energy is needed to separate the node pairs, whereas for a fixed cohesive strength ($\sigma_c = 100$ MPa), increasing the indentation depth from 0.002 to 0.0025 increases the delamination fraction significantly, especially with increasing sliding distance. For $\bar{s} = 0.3$ and $\sigma_c = 100$ MPa, for example, increasing the indentation depth by 25% fosters interfacial delamination more than twice. It is noted that for a relatively high cohesive strength and small indentation depth (or light load), pure indentation loading does not induce delamination.

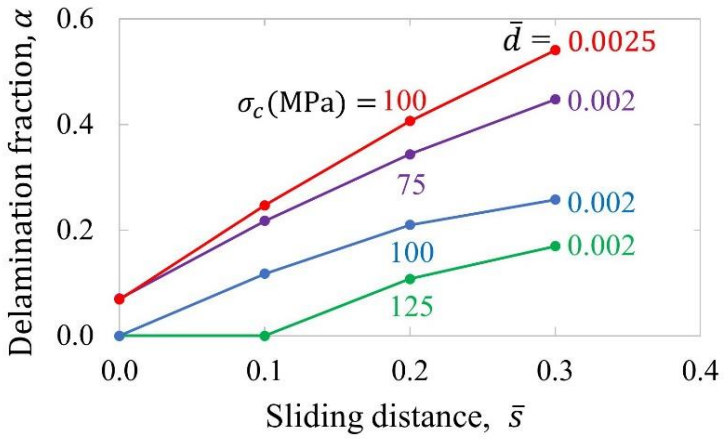

Figure 5.4 Delamination fraction α after unloading versus sliding distance $\bar{s}$ for a homogeneous elastic-plastic half-space with $E = 100$ GPa, Y = 200 MPa, $\bar{d} = 0.002$, 0.0025, and $\sigma_c = 75-125$ MPa.

The distributions of the equivalent von Mises stress σ_{eq} in a homogeneous elastic-plastic half-space shown in Fig. 5.5 provide further insight into interfacial delamination due to indentation loading, sliding, and unloading. Because an indentation depth $\bar{d} = 0.002$ does not cause delamination for $\sigma_c = 100$ MPa (Fig. 5.4), the stress field is characteristic of an indented homogeneous half-space (Fig. 5.5(a)). However, sliding by a distance $\bar{s} = 0.3$ induces delamination at the cohesive interface (Figs. 5.3(b) and 5.4), resulting in localized stress discontinuities and stress intensification in the region above the partially delaminated cohesive interface (Fig. 5.5(b)). Unloading promotes lateral expansion of the high residual stresses above the cohesive interface (Fig. 5.5(c)), attributed to the increase in effective nodal separation in the delaminated portion of the cohesive interface upon unloading (Fig. 5.3(b)).

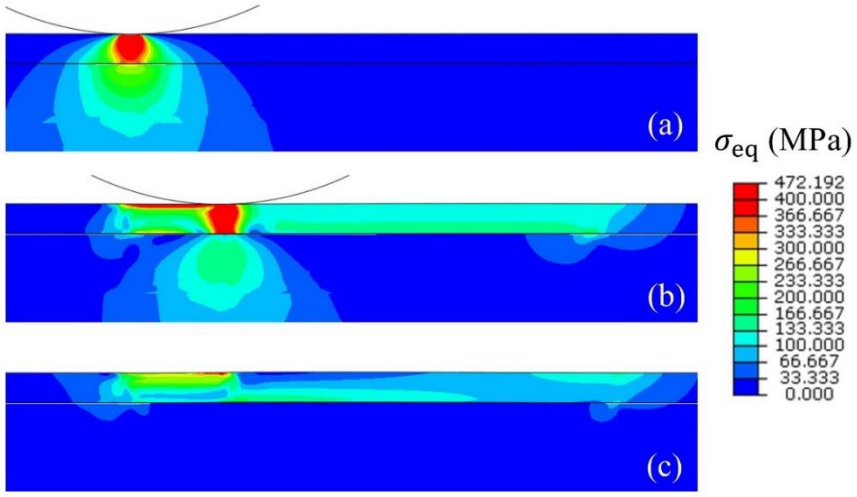

Figure 5.5 Contours of the equivalent von Mises stress σ_{eq} for a homogeneous elastic-plastic half-space with $E = 100$ GPa, $Y = 200$ MPa, and $\sigma_c = 100$ MPa at three sequential simulation stages: (a) indentation ($\bar{d}$ = 0.002), (b) sliding ($\bar{s}$ = 0.3, $\bar{d}$ = 0.002), and (c) unloading. (The horizontal black line corresponds to the delamination interface.)

5.3.2. Delamination in Layered Half-Spaces

Simulation results for layered elastic half-spaces are presented first to illuminate the effect of the elastic modulus mismatch (represented by elastic modulus ratio $\bar{E}$) on the delamination at the layer/substrate interface, hereafter referred to as interfacial delamination. Figure 5.6 shows the variation of the delamination ratio β after unloading with the elastic modulus ratio $\bar{E}$ for $E_s = 85 - 200$ GPa. The figure reveals two important trends. First, all simulation cases demonstrate a monotonic increase in β with $\bar{E}$, originating from a common point ($\beta = 1$) that corresponds to the homogeneous half-space case ($\bar{E} = 1$). The tendency for interfacial delamination to intensify with increasing elastic modulus mismatch can be attributed to the proliferation of the interfacial stresses due to layer stiffening, leading to further nodal separation upon unloading. Second, a nonlinear increase in β with decreasing E_s occurs for fixed E_l. This trend does not imply that a more compliant substrate promotes delamination; rather it suggests a more prominent effect of the layer's elastic modulus on interfacial delamination for more compliant substrates. For $\bar{E} = 2.5$, for instance, the delamination length is about 5.5 and 2 times greater than that corresponding to the homogeneous half-space for $E_s = 85$ and 200 GPa, respectively.

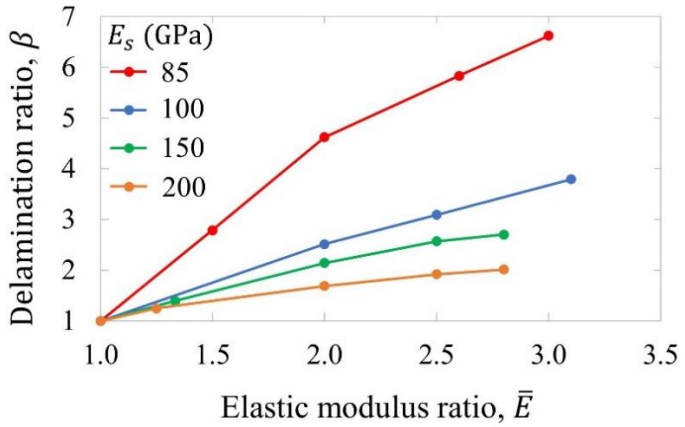

Figure 5.6 Delamination ratio β after unloading versus elastic modulus ratio $\bar{E}$ for an elastic layered half-space with $E_s = 85$–200 GPa and $\sigma_c = 100$ MPa ($\bar{h} = 0.1$, $\bar{d} = 0.002$, and $\bar{s} = 0.1$).

The foregoing result can be explained by considering the stresses produced by the sliding process in elastic layered half-spaces with different layer and substrate elastic moduli. Figure 5.7 shows contours of the equivalent von Mises stress σ_{eq} in an elastic layered half-space produced before unloading for various $\bar{E}$ values and the corresponding delamination fraction α. For a fixed substrate elastic modulus ($E_s = 100$ GPa), layer stiffening intensifies the stresses in the layer and the layer/substrate interface, consequently increasing the delamination fraction (Figs. 5.7(a)–5.7(c)). In the case of homogeneous half-space ($\bar{E} = 1$), high stresses develop below the contact interface and interfacial delamination is limited ($\alpha = 0.05$) due to minor stress intensification at the delamination interface (Fig. 5.7(a)). The tensile and shear stresses arising at interface nodal points slightly to the right of the cylinder increase the effective nodal separation locally, causing delamination at those node pairs where the decohesion condition (Eq. (5.2)) was satisfied. The increase in layer stiffness, significantly fortifies the stresses at the layer/substrate interface, consequently increasing the delamination fraction by a factor of about 3 and 4, i.e., $\alpha = 0.13$ and 0.20 for $\bar{E} = 2$ and 3, respectively (Figs. 5.7(b) and 5.7(c)). A similar trend is observed with the

decrease of substrate stiffness, characterized by the augmentation of interfacial delamination. Specifically, for the most compliant substrate ($\bar{E} = 2$), high stresses develop below the contact interface and across a small interfacial region, resulting in localized delamination ($\alpha = 0.13$) (Fig. 5.7d). Substrate stiffening promotes the evolution of much higher stresses in the layer and the layer/substrate interface, contributing to an increase in delamination fraction with substrate stiffness, i.e.,$\alpha = 0.17$ and 0.22 for $\bar{E} = 1.33$ and 1, respectively (Figs. 5.7(e) and 5.7(f)).

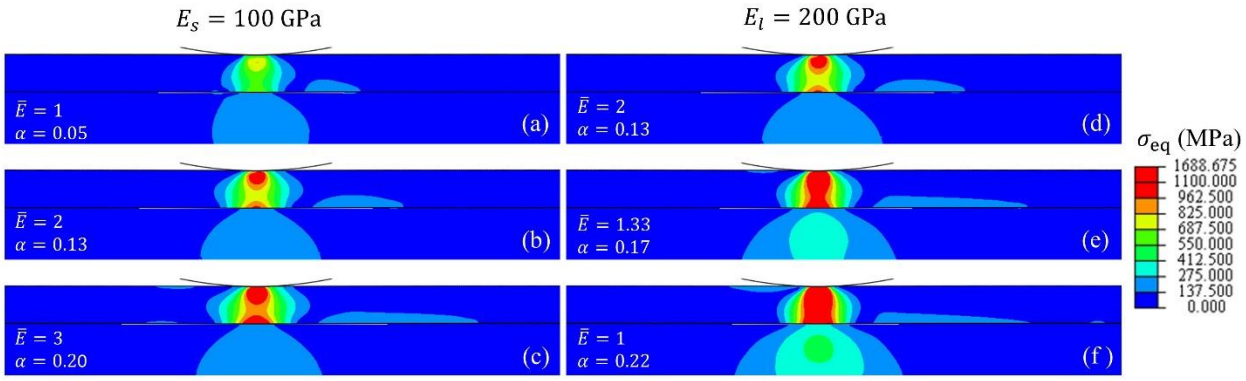

Figure 5.7. Contours of the equivalent von Mises stress σ_{eq} versus elastic modulus ratio $\bar{E}$ and delamination fraction α obtained before unloading for an elastic layered half-space with (a)–(c) $E_s = 100$ GPa and $E_l = 100, 200$, and 300 GPa ($\bar{E}$ = 1, 2, and 3, respectively), (d)–(f) E_l = 200 GPa and E_s = 100, 150, and 200 GPa ($\bar{E}$ = 2, 1.33, and 1, respectively), and $\sigma_c = 100$ MPa ($\bar{h}$ = 0.1, $\bar{d}$ = 0.002, and $\bar{s}$ = 0.1). (The horizontal black line corresponds to the delamination interface.)

Simulation results for elastic-plastic layered media are presented next to reveal the effect of plasticity on the evolution of interfacial delamination. Figure 5.8 shows the delamination fraction α after unloading versus the yield strength ratio $\bar{Y}$. Although interfacial delamination does not occur for $Y_s = 50$ MPa, all other simulations demonstrate an initial increase in α with $\bar{Y}$ followed by a decrease beyond a certain $\bar{Y}$ value, depending on the yield strength of the substrate Y_s. Specifically, the maximum α for $Y_s = 100, 200$ and 300 MPa corresponds to $\bar{Y} \cong 1.3, 0.75$, and 0.5, respectively. Moreover, although a higher yield strength of the substrate produces a higher delamination fraction in the low range of $\bar{Y}$, an opposite tendency occurs in the high range of $\bar{Y}$, where the delamination fraction decreases sharply. This trend is also reflected in the results of the effective nodal separation presented next.

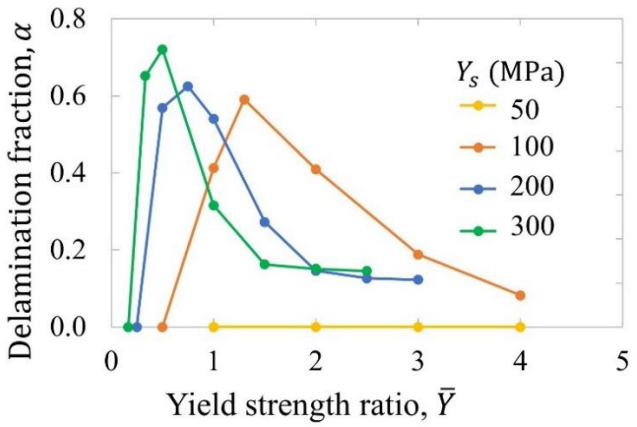

Figure 5.8 Delamination fraction α after unloading versus yield strength ratio $\bar{Y}$ for an elastic-plastic layered half-space with $E_l = E_s = 100$ GPa ($\bar{E} = 1$), Y_s = 50–300 MPa, and $\sigma_c = 100$ MPa ($\bar{h}$ = 0.1, $\bar{d}$ = 0.0025, and $\bar{s}$ = 0.3).

Figure 5.9 shows distributions of the effective nodal separation $\bar{\delta}$ before and after unloading for a layered elastic-plastic half-space with $\bar{Y} = 0.75$ and 1. Before unloading, significantly larger nodal separation distances arise for the relatively lower strength layer ($\bar{Y} = 0.75$), especially in the interfacial region $-10 < x/w < 0$, compared to the higher strength layer ($\bar{Y} = 1.5$). A notable amplification of the nodal separation distances originates upon unloading, especially for $\bar{Y} = 0.75$, where much larger nodal separations develop in the interfacial region $0 < x/w < 12$ and much lower in the region $-10 < x/w < 0$, contrary to what is found before unloading. This can be attributed to the effect of residual stresses in the layer causing it to conform and the nodal separations to adjust accordingly. For $\bar{Y} = 1.5$, however, the increase in nodal separation upon unloading is much less pronounced than that for $\bar{Y} = 0.75$. The difference between these two cases can also be quantified in terms of the delamination fraction, i.e., $\alpha = 0.55$ and 0.62 ($\bar{Y} = 0.75$) and $\alpha = 0.27$ and 0.27 ($\bar{Y} = 1.5$) before and after unloading, respectively. Despite the increase of the effective nodal separation in Fig. 5.9(b), the delamination fraction does not change upon unloading because the delamination criteria (Eqs. 5.2–5.11) are not satisfied in this case. This is also the reason for the constancy of the delamination fraction seen in some of the unloading simulations presented in following figures. The results shown in Fig. 5.9 illustrate that increasing $\bar{Y}$ (or Y_l) by a factor of 2 decreases $\bar{\delta}_{\max}$ by a factor of ~3 and the delamination length by a factor >2, indicating a profound effect of the yield strength of the layer on interface delamination.

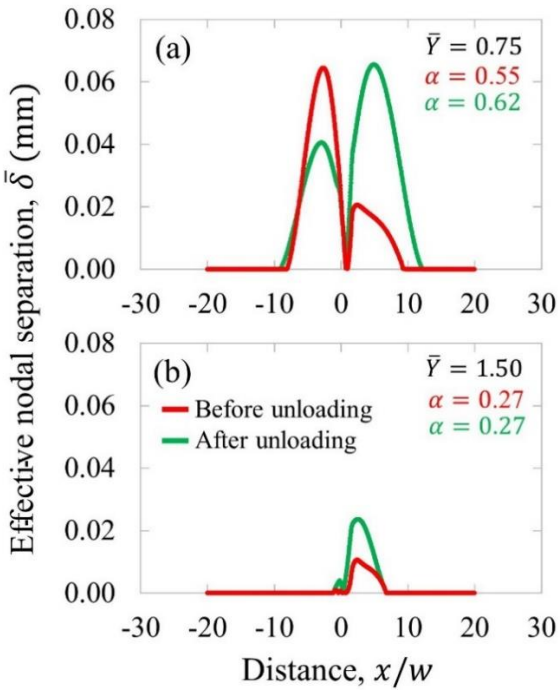

Figure 5.9 Effective nodal separation $\bar{\delta}$ profiles at the delamination interface ($\bar{h}$ = 1) obtained (—) before and (—) after unloading versus distance x/w measured from the center of initial contact (x/w = 0) for a layered elastic-plastic half-space with $E_l = E_s = 100$ GPa ($\bar{E}$ = 1), $E_s = 200$ MPa, (a) $Y_l = 150$ MPa ($\bar{Y} = 0.75$), (b) $Y_l = 300$ MPa ($\bar{Y}$ = 1.5), and $\sigma_c = 100$ MPa ($\bar{h}$ = 0.1, $\bar{d}$ = 0.0025, and $\bar{s}$ = 0.3).

The results shown in Figs. 5.8 and 5.9 can be interpreted by considering the effect of the yield strength ratio $\bar{Y}$ on the subsurface stress and strain fields before and after unloading. Figure 5.10 shows contours of the von Mises equivalent stress σ_{eq} in an elastic-plastic layered half-space for different values of the yield strength ratio $\bar{Y}$. For $\bar{Y} = 0.25$ (Fig. 5.10(a)), two small pockets of high stress form before unloading, one adjacent to the contact interface and another in the substrate just below the layer/substrate interface. However, the generated interfacial stresses do not satisfy the fracture energy criteria to instigate delamination ($\alpha = 0$), consistent with the result shown in Fig. 5.8. For $\bar{Y} = 0.75$ (Fig. 5.10(c)), significantly higher stresses occur in the layer, spreading laterally and through the layer/substrate interface and causing interfacial delamination ($\alpha = 0.55$). For $\bar{Y} = 1.5$ (Fig. 5.10(e)), a larger zone of high stresses develops in the layer; nonetheless, both stress spreading within the layer and delamination are less ($\alpha = 0.27$) than those for $\bar{Y} = 0.75$. All simulations demonstrate extremely small residual stresses in the substrate just below the layer/substrate interface after unloading, suggesting that plastic deformation is confined within the layer and at the layer/substrate interface. A comparison of Figs. 5.10(b), 5.10(d), and 5.10(f) indicates that, although the increase in $\bar{Y}$ progressively intensifies the residual stresses, the effect on the delamination length does not show a specific trend. Specifically, for $\bar{Y} = 0.75$ (Fig. 5.10(d)), the delamination length increases from 0.55 to 0.62 after unloading, whereas for $\bar{Y} = 1.5$ (Fig. 5.10(f)), the effect of unloading on the delamination length is negligible.

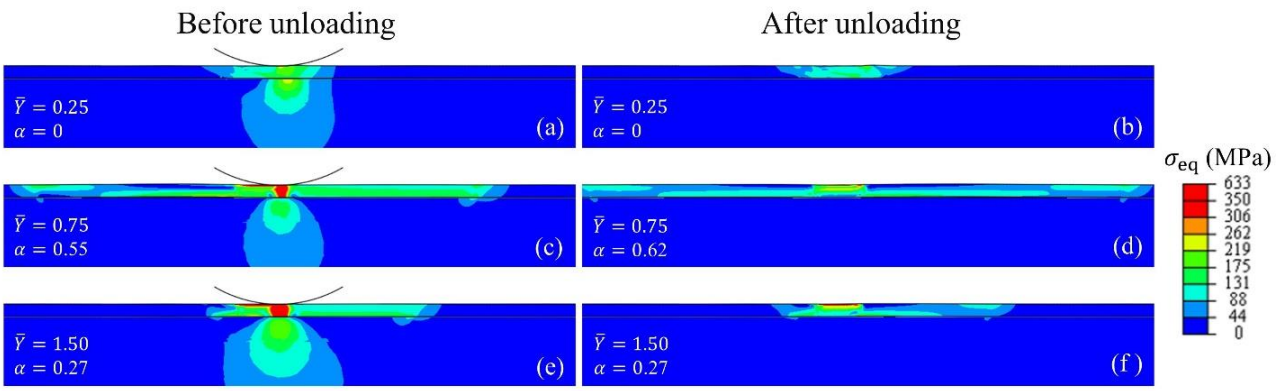

Figure 5.10 Contours of the equivalent von Mises stress σ_{eq} before (left) and after (right) unloading versus yield strength ratio $\bar{Y}$ and delamination fraction α for an elastic-plastic layered half-space with $E_l = E_s = 100$ GPa ($\bar{E}$ = 1), $Y_s = 200$ MPa, $Y_l =$ 50, 150, and 300 MPa ($\bar{Y} = 0.25, 0.75$, and 1.5, respectively), and σ_c = 100 MPa ($\bar{h}$ = 0.1, $\bar{d}$ = 0.0025, and $\bar{s}$ = 0.3). (The horizontal black line corresponds to the delamination interface.)

The contours of the equivalent plastic strain $\varepsilon_{\mathrm{eq}}^{\mathrm{p}}$ shown in Fig. 5.11 provide further insight into the previous findings, confirming the strong effect of the yield strength of the layer on interfacial delamination. Despite the widespread plastic deformation in the bulk of the layer and at the layer/substrate interface for $\bar{Y} = 0.25$ (Fig. 5.11(a)), the relatively low stresses in the low-strength layer (Fig. 5.10(a)) do not lead to delamination ($\alpha = 0$). Moreover, while layer strengthening ($\bar{Y} = 0.75$) reduces widespread plasticity in the layer (Fig. 5.11(b)), it also intensifies the stresses at the layer/substrate interface (Fig. 5.10(c)), resulting in delamination ($\alpha = 0.55$), which is further augmented upon unloading ($\alpha = 0.62$) (Fig. 5.11(b)). Interestingly, further layer strengthening ($\bar{Y} = 1.5$) reduces plasticity in the layer significantly, with large plastic strains being confined to the upper region of the layer (Fig. 5.11(c)); but although this is accompanied by stress intensification (Fig. 5.10(e)), delamination decreases and remains unaffected even after unloading ($\alpha = 0.27$) (Fig. 5.10(f)). A similar result is encountered by varying the yield strength of the substrate while maintaining a high yield strength of the layer (Figs. 5.11(d)–5.11(f)), signifying a dominant effect of layer plasticity on interfacial delamination.

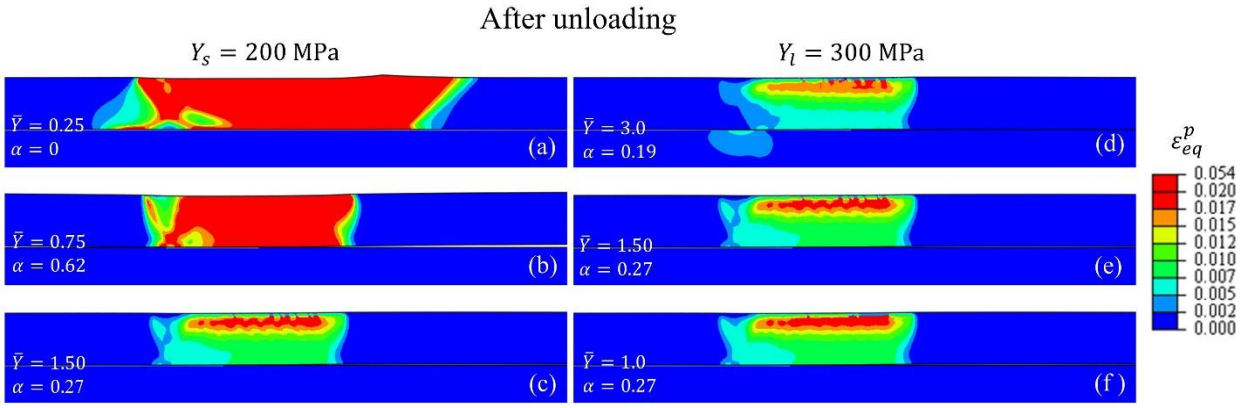

Figure 5.11 Contours of the equivalent plastic strain ε_{eq}^{p} after unloading versus yield strength ratio $\bar{Y}$ and delamination fraction α for an elastic-plastic layered half-space with $E_l = E_s = 100$ GPa ($\bar{E}$ = 1), (a–c) $Y_s = 200$ MPa and $Y_l = 50, 150,$ and 300 MPa ($\bar{Y}$ = 0.25, 0.75, and 1.5, respectively), (d–f) Y_l = 300 MPa and Y_s = 100, 200, and 300 MPa ($\bar{Y}$ = 3, 1.5, and 1, respectively), and σ_c = 100 MPa ($\bar{h}$ = 0.1, $\bar{d}$ = 0.0025, and $\bar{s}$ = 0.3). (The horizontal black line corresponds to the delamination interface.)

Figure 5.12 shows the distributions of effective nodal separation $\bar{\delta}$ acquired before and after unloading of an elastic-plastic layered half-space for different values of yield strength ratio $\bar{Y}$. These results provide additional supporting proof to the foregoing contention. In all simulation cases, unloading enhances surface separation without affecting the delamination fraction. The highest yield strength ratio ($\bar{Y} = 3$) produces the smallest nodal surface separations and delamination fraction ($\alpha = 0.19$) (Fig. 5.12(a)). Decreasing $\bar{Y}$ instigates larger delamination gaps, but only a small increase in delamination fraction, i.e., $\alpha = 0.27$ for both $\bar{Y} = 1.5$ (Fig. 5.12(b)) and $\bar{Y} = 1$ (Fig. 5.12(c)). The results shown in Fig. 5.12 can be further interpreted by examining the corresponding stress fields before and after unloading, shown in Fig. 5.13. A comparison of the stress fields before or after unloading shows close similarity, though the stresses are less spread out in the layer for $\bar{Y} = 3$ than $\bar{Y} = 1.5$ and 1, consistent with the corresponding delamination fractions and the variation of α with $\bar{Y}$ displayed in Fig. 5.8.

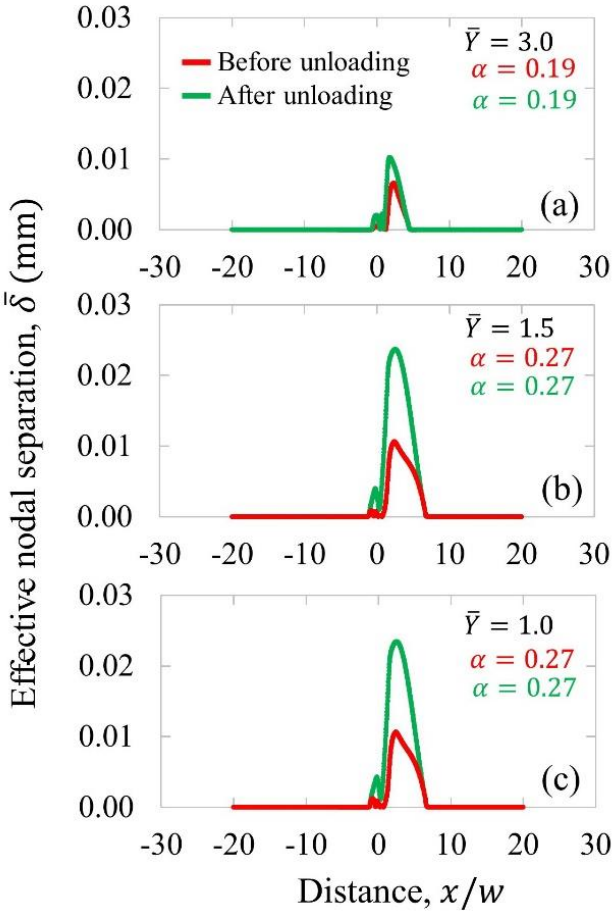

Figure 5.12 Effective nodal separation $\bar{\delta}$ profiles at the delamination interface ($\bar{h}$ = 1) obtained (—) before and (—) after unloading versus distance x/w measured from the center of initial contact (x/w = 0) for a layered elastic-plastic half-space with $E_l = E_s = 100$ GPa ($\bar{E}$ = 1), Y_l = 300 MPa, (a) Y_s = 100 MPa ($\bar{Y}$ = 3), (b) Y_s = 200 MPa ($\bar{Y}$ = 1.5), (c) Y_s = 300 MPa ($\bar{Y}$ = 1), and σ_c = 100 MPa ($\bar{h}$ = 0.1, $\bar{d}$ = 0.0025, and $\bar{s}$ = 0.3).

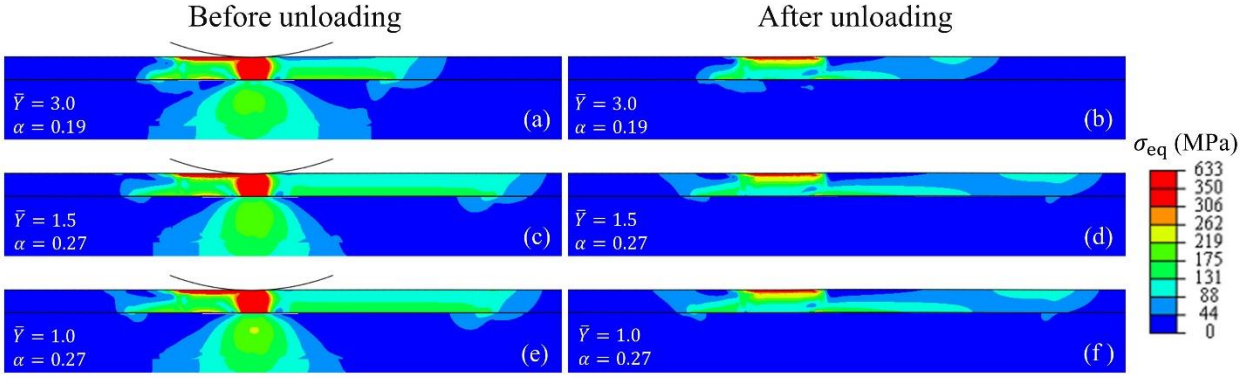

Figure 5.13 Contours of the equivalent von Mises stress σ_{eq} before (left) and after (right) unloading versus yield strength ratio $\bar{Y}$ and delamination fraction α for an elastic-plastic layered half-space with $E_l = E_s = 100$ GPa ($\bar{E}$ = 1), Y_s = 300 MPa, Y_s = 100, 200, and 300 MPa ($\bar{Y}$ = 3, 1.5, and 1, respectively), and σ_c = 100 MPa ($\bar{h}$ = 0.1, $\bar{d}$ = 0.0025, and $\bar{s}$ = 0.3). (The horizontal black line corresponds to the delamination interface.)

In addition to the elastic-plastic material properties of the layered half-space, the layer thickness is another important parameter affecting the stresses arising at the layer/substrate interface and, consequently, interfacial delamination. Figure 5.14 shows the delamination fraction α after unloading as a function of layer thickness $\bar{h}$ for different values of $\bar{Y}$. All simulation cases display a monotonic decrease in α with increasing $\bar{h}$ and $\bar{Y}$. This trend can be explained by considering that a thicker and stronger layer can accommodate much higher stresses compared to a thinner and weaker layer, hence significantly lessening the stresses at the layer/substrate interface and in the bulk of the substrate. In fact, the material near the interface may not even experience plastic deformation in the case of a thicker layer, despite the material property mismatch between the layer and the substrate.

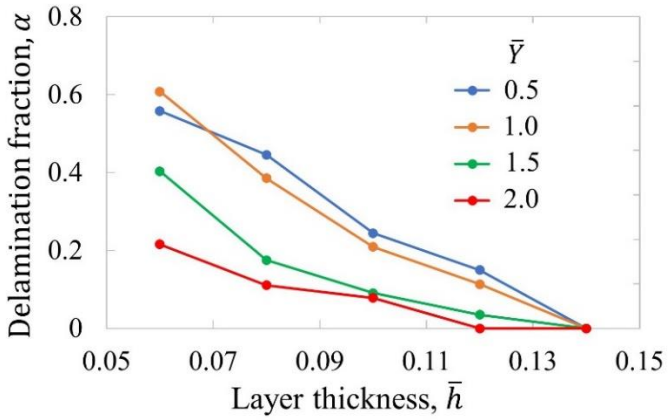

Figure 5.14 Delamination fraction α after unloading versus delamination layer thickness $\bar{h}$ for an elastic-plastic layered half-space with $E_l = E_s = 100$ GPa ($\bar{E} = 1$), Y_s = 200 MPa, Y_l = 100–400 MPa ($\bar{Y}$ = 0.5–2, respectively) and σ_c = 100 MPa ($\bar{d} = 0.002$, $\bar{s} = 0.2$).

5.4. Conclusions

A contact mechanics analysis of interfacial delamination in homogeneous and layered elastic-plastic half-spaces subjected to normal and shear tractions generated by indentation and sliding was performed in this study. A surface-based CZM was implemented in a FEM analysis to model nodal separation at the delamination interface (layer/substrate interface for layered half-spaces) when appropriate fracture energy conditions were satisfied. A parametric study demonstrated that increasing the indentation depth and/or sliding distance and decreasing the cohesive strength enhances interfacial delamination in homogeneous elastic-plastic half-spaces, even more after unloading, the primary reason being the high stresses spreading in the region above the delamination interface. An elastic FEM analysis of layered half-spaces showed that increasing the elastic modulus of the layer while fixing that of the substrate results in high stress localization, whereas the reverse causes more pronounced stress intensification in the bulk of the layer and at its interface with the substrate, with both scenarios leading to the enhancement of delamination at the layer/substrate interface. Simulations of an elastic-plastic FEM analysis demonstrated a significant effect of the yield strength mismatch between the layer and the substrate on the delamination process, characterized by a transition from increasing to decreasing delamination with the increase of the layer-to-substrate yield strength ratio. This trend is attributed to a change from intensifying to lessening subsurface stresses and less plastic deformation in the layer and the layer/substrate interface. The effect of layer strengthening on interfacial delamination is more

profound than that of substrate stiffening. Moreover, increasing the layer thickness while maintaining a high yield strength of the layer effectively suppresses delamination at the layer/substrate interface. The results of this study provide insight into the effects of indentation depth, sliding distance, and elastic-plastic property mismatch between the layer and substrate of layered half-spaces on interfacial delamination. The present analysis can be further extended to include a plasticity-induced damage model for studying cumulative damage in strain-hardening half-spaces subjected to cyclic dynamic contact loading by a rigid surface exhibiting multiscale roughness.

CHAPTER 6

Conclusions

Computational contact mechanics analyses were performed to study the evolution of plasticity and material damage of two contacting bodies under normal and/or tangential loads. The results of this thesis provide important insight into the development of stress field, plastic strain and material removal under indentation, fretting and sliding mechanics. Surface roughness modeling and its effect were also discussed followed by a material failure study of the interfacial delamination process. The major findings of this thesis are summarized below.

First, the evolution of plasticity in an elastic-plastic, strain-hardening half-space indented by a rigid single flat or patterned surface was interpreted in the context of quasi-static, plane-strain FEM simulations. A mesh independence study was conducted, and the computed contact pressure distribution was compared against an analytical solution of a single flat surface indenting an elastic substrate to ensure the adequacy of the mesh. Numerical results showed the development of high stresses and strains in the vicinities of the contact edge and corners of a flat-surface indenter. While similar stress and strain fields were observed for a patterned-surface indenter during the initial stage of indentation, as the indentation depth increased, the deformation in the half-space was largely affected by the interaction of neighboring stress and strain fields. The normal force response included an initial elastic response and a steady-state response wherein the normal force increased gradually as the indentation progressed for both flat- and patterned-surface indentation. However, a third stage of the normal force response was found in the case of patterned-surface indentation, mainly caused by cavity filling that increased the contact area. Geometric factors, such as the side wall angle, exhibited a profound effect on plasticity, with small side wall angle producing a higher normal force due to the resulting larger contact area. In addition, larger protrusion distance and lower coefficient of friction produced a higher normal force, increased cavity filling, and intensified the stress and strain fields. At a large normal displacement where cavity filling was significant, the maximum equivalent plastic strain in the half-space approached that of flat-surface indentation.

Next, a quasi-static, plane-strain FEM analysis was performed to examine the evolution of plasticity and material removal in an elastic-plastic half-space due to reciprocating sliding contact with a rigid cylindrical surface. Strain hardening material behavior and a plasticity-based ductile damage model was used to simulate the removal of fully damaged material. A dimensionless plastic-strain-based damage parameter was used to track the damage accumulation in the finite elements. Once the damage parameter reached unity, a linear stiffness degradation process was initiated, which was controlled by a dimensionless degradation parameter that increased from 0 to 1, at which instant the element was removed from the finite element mesh. The penetration depth increased with the load and the number of oscillation cycles, tending to stabilize after a few cycles especially at high loads. A parametric study elucidated the effects of normal load and the coefficient of friction on the development of plasticity and the removal of material with accumulating oscillation cycles. Specifically, the dimensionless plastic and wear areas increased with the coefficient of friction due to the enhancement of plastic shearing, revealing a dominant role of friction in plasticity and material loss. However, while the wear area initially increased linearly with the oscillation cycles, later it decreased when the load was increase above a threshold level, contrary to the classical adhesive wear law proposed by

Archard. This trend was explained in terms of the distribution of the plastic shear strain in low- and high-load oscillations. Particularly, high plastic shear strains developed adjacent to the contact interface in the low-load case, whereas in the high-load case, lower plastic shear strains occurred below the interface. The fraction of contact area in slip mode demonstrated a monotonic decrease with increasing load, indicating that a high load hindered interfacial slip due to the restriction of the rigid cylinder's movement by the surrounding material, consequently causing less plastic shearing under high-load oscillation conditions and, in turn, less material loss.

Plastic deformation and material loss in an elastic-plastic half-space subjected to fretting contact with a random rough (fractal) rigid surface was then investigated in the context of numerical results of a quasi-static, plane-strain FEM analysis. Plasticity-induced damage was tracked using a plasticity-based dimensionless parameter, while stiffness degradation was controlled by a dimensionless degradation parameter. The rough surface was modeled by fractal geometry, characterized by the properties of continuity, non-differentiability, and self-affinity. In general, both subsurface stresses and plastic strains intensified as the decrease of fractal dimension (rougher surface) and the increase of fretting cycles. For fixed fractal parameters, the increase of the normal load and the occurrence of material removal lowered the intensity of subsurface stresses with increasing number of oscillation cycles and a continuous plastic band formed along the contact interface. Rougher surfaces demonstrated higher material removal rate exhibiting a nonlinear load dependence, in contrast to the classical wear law of Archard. This nonlinear load dependence of the wear rate was attributed to the effects of increasing surface conformity and mechanical interlocking of the fractal surface with the half-space with the increase of the applied load, which restricted relative slip at the contact interface and, in turn, reduced the material loss.

The problem of subsurface delamination in homogeneous and layered elastic-plastic half-spaces due to indentation and sliding loading by a rigid cylinder was examined using a quasi-static FEM analysis. A surface-based cohesive zone model was used to simulate delamination at mesh locations where a fracture-energy-based separation condition was satisfied. The effect of material property mismatch in layered half-spaces was examined by varying the elastic modulus ratio, defined as the layer's elastic modulus over that of the substrate, and the yield strength ratio, obtained as the yield strength of the layer divided by that of the substrate. A larger indentation depth, greater sliding distance, and smaller cohesive strength promoted delamination in the homogeneous half-space persisting throughout unloading due to high stresses developing in the layer above the delamination interface. In the case of elastic behavior, the delamination at the layer/substrate interface was enhanced with the increase of the elastic modulus of the layer while keeping that of the substrate constant or fixing the layer's elastic modulus and increasing that of the substrate, both intensifying the stresses in the layer. In the case of elastic-plastic behavior, the yield strength mismatch demonstrated a significant effect on delamination. Specifically, delamination initially increased and then decreased with increasing yields strength ratio. This trend was attributed to first intensifying and then lessening of the subsurface stresses and the limited plastic deformation in the layer and at the interface. Moreover, delamination at the layer/substrate interface was found to decrease with the increase of the layer thickness.

In summary, the main contribution of this thesis in the field of contact mechanics is the establishment of FEM-based modeling approaches for investigating the evolution of plasticity and material failure (including plasticity-induced damage, material removal, and subsurface

delamination) in terms of the applied normal load and/or a combination of normal and tangential loading, the number of oscillation cycles, coefficient of friction, and surface topology (roughness). The developed numerical methodology provided detailed insight into complex contact problems and the capability for evaluating product designs involving surface contact. The constitutive models for strain hardening material and plastic damage can be modified to enable modeling for temperature-dependent applications, such as thermomechanical modeling of the frictional heating process in mechanical wire bonding and electromechanical relays in battery-control systems. Furthermore, the plastic damage model used in the current framework can be tuned to model specific material behaviors, such as fracture for various triaxiality levels.

ABAQUS analysis user's guide, 2022.

ABAQUS/CAE 2020. User's manual. Dassault Systèmes Simulia Corp., Providence, RI, USA.

Abu Al-Rub, R.K., Voyiadjis, G.Z., 2004. Analytical and experimental determination of the material intrinsic length scale of strain gradient plasticity theory from micro- and nano-indentation experiments. Int. J. Plast. 20, 1139–1182.

Aghababaei, R., Warner, D.H., Molinari, J.-F., 2017. On the debris-level origins of adhesive wear. Proc. Natl. Acad. Sci. USA 114, 7935–7940.

Aizawa, T., Tamaki, M., Fukuda, T., 2014. Large area micro-texture imprinting onto metallic sheet via CNC stamping. Procedia Eng. 81, 1427–1432.

Alfano, M., Furgiuele, F., Leonardi, A., Maletta, C., and Paulino, G. H., 2009, "Mode I Fracture of Adhesive Joints Using Tailored Cohesive Zone Models," *Int. J. Fract.* 157, pp. 193–204.

Ambrico, J.M., Begley, M.R., 2000. Plasticity in fretting contact. J. Mech. Phys. Solids 48, 2391–2417.

Archard, J.F., 1953. Contact and rubbing of flat surfaces. J. Appl. Phys. 24, 981–988.

Asad, M., Mabrouki, T., Ijaz, H., Aurangzeb Khan, M., Saleem, W., 2014. On the turning modeling and simulation: 2D and 3D FEM approaches. Mech. Ind. 15, 427–434.

Ausloos, M., Berman, D.H., 1985. A multivariate Weierstrass-Mandelbrot function. Proc. R. Soc. Lond. A 400, 331–350.

Barenblatt, G. I., 1962, "The Mathematical Theory of Equilibrium Cracks in Brittle Fracture," *Adv. Appl. Mech.* 7, pp. 55–129.

Bazrafshan, M., de Rooij, M.B., Schipper, D.J., 2018. On the role of adhesion and roughness in stick-slip transition at the contact of two bodies: A numerical study. Tribol. Int. 121, 381–388.

Ben Tkaya, M., Zahouani, H., Mezlini, S., Kapsa, Ph., Zidi, M., Dogui, A., 2007. The effect of damage in the numerical simulation of a scratch test. Wear 263, 1533–1539.

Berry, M.V., Lewis, Z.V., 1980. On the Weierstrass-Mandelbrot fractal function. Proc. R. Soc. Lond. A 370, 459–484.

Björklund, S., 1997. A random model for micro-slip between nominally flat surfaces. ASME. *J. Tribol*. 119, 726–732.

Block, J.M., Keer, L.M., 2008. Periodic contact problems in plane elasticity. J. Mech. Mater. Struct. 3, 1207–1237.

Bortoleto, E.M., Rovani, A.C., Seriacopi, V., Profito, F.J., Zachariadis, D.C., Machado, I.F., Sinatora, A., Souza, R.M., 2013. Experimental and numerical analysis of dry contact in the pin on disc test. Wear 301, 19–26.

Camanho, P. P., Davila, C. G., and de Moura, M. F., 2003, "Numerical Simulation of Mixed-Mode Progressive Delamination in Composite Materials," *J. Comp. Mater*. 37, pp. 1415–1438.

Cattaneo, C., 1938. Sul contato di due corpo elastici. Atti Accad. Naz. Lincei, Cl. Sci. Fis., Mat. Nat., Rend., 27, 342–348, 434–436, 474–478.

Cen, J., Komvopoulos, K., 2022. Plasticity-induced damage and material loss in oscillatory contacts. Int. J. Solids Struct. 254–255, 111932.

Chakravarthy, S.S., Curtin, W.A., 2011. Stress-gradient plasticity. Proc. Nat. Acad. Sci. USA 108, 15716–15720.

Chandra, A., 1986. A generalized finite element analysis of sheet metal forming with an elastic-viscoplastic material model. ASME J. Eng. Ind. 108, 9–15.

Chatterjee, B., Sahoo, P., 2014. Finite element based contact analysis of fractal surfaces – effect of varying elastic modulus. Procedia Eng. 90, 116–122.

Chen, Z., Etsion, I., 2019. Model for the static friction coefficient in a full stick elastic-plastic coated spherical contact. Friction 7, 613–624.

Cho, S.-S., and Komvopoulos, K., 1997, "Wear Mechanisms of Multi-Layer Coated Cemented Carbide Cutting Tools," ASME *J. Tribol.* 119, pp. 8–17.

Choi, J.-Y., Ko, Y.B., Kim, J., Yoon, G.S., Park, J., Heo, Y.M., La, M., 2017. Direct metal to metal imprinting for developing 1-step manufacturing process of patterned metal surface. Procedia Eng. 207, 1022–1026.

Choi, S. R., Hutchinson, J. W., and Evans, A. G., 1999, "Delamination of Multilayer Thermal Barrier Coatings," *Mech. Mater.* 31, pp. 431–447.

Dimaki, A.V., Shilko, E.V., Dudkin, I.V., Psakhie, S.G., Popov, V.L., 2020. Role of adhesion stress in controlling transition between plastic, grinding and breakaway regimes of adhesive wear. Sci. Rep. 10, 1585.

Dugdale, D. S., 1960, "Yielding of Steel Sheets Containing Slits," *J. Mech. Phys. Solids,* 8, pp. 100–104.

Elwasli, F., Zemzemi, F., Mkaddem, A., Mzali, S., Mezlini, S., 2015. A 3D multi-scratch test model for characterizing material removal regimes in 5083-Al alloy. Mater. Des. 87, 352–362.

Eriten, M., Polycarpou, A.A., Bergman, L.A., 2011. Physics-based modeling for fretting behavior of nominally flat rough surfaces. Int. J. Solids Struct. 48, 1436–1450.

Etsion, I., 2010. Revisiting the Cattaneo–Mindlin concept of interfacial slip in tangentially loaded compliant bodies. ASME. *J. Tribol.* 132, 020801.

Fleck, N.A., Hutchinson, J.W., 1993. A phenomenological theory for strain gradient effects in plasticity. J. Mech. Phys. Solids 41, 1825–1857.

Fleck, N.A., Muller, G.M., Ashby, M.F., Hutchinson, J.W., 1994. Strain gradient plasticity: Theory and experiment. Acta Metall. Mater. 42, 475–487.

Fouvry, S., Kapsa, P., Vincent, L., 1996. Quantification of fretting damage. Wear 200, 186–205.

Frérot, L., Aghababaei, R., Molinari, J.-F., 2018. A mechanistic understanding of the wear coefficient: From single to multiple asperities contact. J. Mech. Phys. Solids, 114, 172–184.

Freund, L., and Suresh, S., 2004, *Thin Film Materials: Stress, Defect Formation and Surface Evolution*, Cambridge University Press, Cambridge, U. K.

Gao, Y. F., and Bower, A. F., 2004, "A Simple Technique for Avoiding Convergence Problems in Finite Element Simulations of Crack Nucleation and Growth on Cohesive Interfaces," *Modelling Simul. Mater. Sci. Eng.* 12, p. 453.

Gerberich, W. W., Kramer, D. E., Tymiak, N. I., Volinsky, A. A., Bahr, D. F., and Kriese, M. D., 1999, "Nanoindentation-Induced Defect–Interface Interactions: Phenomena, Methods and Limitations," *Acta Mater.* 47, pp. 4115–4123.

Ghosh, S., Kikuchi, N., 1988. Finite element formulation for the simulation of hot sheet metal forming processes 26, 143–161.

Giannakopoulos, A.E., Suresh, S., 1998. A three-dimensional analysis of fretting fatigue. Acta Mater. 46, 177–192.

Gong, Z.-Q., Komvopoulos, K., 2004a. Mechanical and thermomechanical elastic-plastic contact analysis of layered media with patterned surfaces. ASME J. Tribol. 126, 9–17.

Gong, Z.-Q., Komvopoulos, K., 2004b. Surface cracking in elastic-plastic multi-layered media due to repeated sliding contact. ASME J. Tribol. 126, 655–663.

Goryachev, I.G., Malanchuk, N.I., Martynyak, R.M., 2012. Contact interaction of bodies with a periodic relief during partial slip. J. Appl. Math. Mech. 76, 621–630.

Hassan, M., Ali, A., Ilyas, M., Hussain, G., and ul Haq, I., 2019, "Experimental and Numerical Simulation of Steel/Steel (St/St) Interface in Bi-Layer Sheet Metal," *Int. J. Lightweight Mater. Manuf.* 2, pp. 89–96.

He, M. Y., Hutchinson, J. W., and Evans, A. G., 2011, "A Stretch/Bend Method for In Situ Measurement of the Delamination Toughness of Coatings and Films Attached to Substrates," ASME. *J. Appl. Mech.* 78, p. 011009.

Hertz, H., 1882. Über die berührung fester elastischer körper (On the contact of rigid elastic solids). *J. Reine Angewandte Mathematik* 92, 156–171. (English translation: Hertz, H. (1896). *On the contact of elastic solids. In: Miscellaneous Papers by H. Hertz.* Jones, D. E., and Schott, G. A. (eds.), London: Macmillan, pp. 146–162.)

Hillerborg, A., Modēer, M., Petersson, P.-E., 1976. Analysis of crack formation and crack growth in concrete by means of fracture mechanics and finite elements. Cem. Conc. Res. 6, 773–781.

Hirai, Y., Fujiwara, M., Okuno, T., Tanaka, Y., Endo, M., Irie, S., Nakagawa, K., Sasago, M., 2001. Study of the resist deformation in nanoimprint lithography. J. Vac. Sci. Technol. B 19, 2811–2815.

Hirai, Y., Konishi, T., Yoshikawa, T., Yoshida, S., 2004. Simulation and experimental study of polymer deformation in nanoimprint lithography. J. Vac. Sci. Technol. B 22, 3288–3293.

Hu, G.-D., Panagiotopoulos, P.D., Panagouli, Scherf, O., Wriggers, P., 2000. Adaptive finite element analysis of fractal interfaces in contact problems. Comput. Methods Appl. Mech. Eng. 182, 17–37.

Hu, Z., Lu, W., Thouless, M.D., Barber, J.R., 2016. Effect of plastic deformation on the evolution of wear and local stress fields in fretting. Int. J. Solids Struct. 82, 1–8.

Jäger, J. 1998. A new principle in contact mechanics. ASME J. Tribol. 120, 677–684.

Johnson, G.R., Cook, W.H., 1985. Fracture characteristics of three metals subjected to various strains, strain rates, temperatures and pressures. Eng. Fract. Mech. 21, 31–48.

Johnson, G.R., Holmquist, T.J., 1989. Test data and computational strength and fracture model constants for 23 materials subjected to large strains, high strain rates, and high temperatures. Tech. Rep. LA-11463-MS, Los Alamos National Laboratory.

Johnson, K.L., 1985. Contact Mechanics. Cambridge University Press, Cambridge, UK.

Kim, J.-H., Kil, H.-J., Lee, S., Park, J., and Park, J.-W., 2022, "Interfacial Delamination at Multilayer Thin Films in Semiconductor Devices," ACS *Omega* 7, pp. 25219−25228.

Kim, N.H., Choi, K.K., Chen, J.S., 2001. Die shape design optimization of sheet metal stamping process using meshfree method. Int. J. Numer. Meth. Engng. 51, 1385–1405.

Klimchuk, T., Ostryk, V., 2020. Stress distributions in the Cattaneo–Mindlin problem on a contact with slip and adhesion of two cylindrical bodies. Front. Mech. Eng. 6, 22.

Ko, S. W., Dechakupt, T., Randall, C. A., Trolier-McKinstry, S., Randall, M., and Tajuddin, A., 2010, "Chemical Solution Deposition of Copper Thin Films and Integration into a Multilayer Capacitor Structure," *J. Electroceram.* 24, pp. 161–169.

Komvopoulos, K., 2012. Adhesive wear. In: *Handbook of Lubrication and Tribology*, *Volume II: Theory and Design*, 2nd edition, R. W. Bruce (ed.), CRC Press, Boca Raton, FL, Chapter 7, pp. 7-1–7-21.

Komvopoulos, K., 2020. A multiscale theoretical analysis of the mechanical, thermal, and electrical characteristics of rough contact interfaces demonstrating fractal behavior. Frontiers Mech. Eng. 6, 36.

Komvopoulos, K., Choi, D.-H., 1992. Elastic finite element analysis of multi-asperity contacts. ASME J. Tribol. 114, 823–831.

Komvopoulos, K., Yan, W., 1997. A fractal analysis of stiction in microelectromechanical systems. ASME J. Tribol. 119, 391–400.

Krenk, S., 1992, "Energy Release Rate of Symmetric Adhesive Joints," *Eng. Fract. Mech.* 43, pp. 549–559.

Kuno, M., Waterhouse, R.B., Nowell, D., Hills, D.A., 1989. Initiation and growth of fretting fatigue cracks in the partial slip regime. Fatigue Fract. Eng. Mater. Struct. 12, 387–398.

La, M., Hwang, T.Y., Choi, J.-Y., Hong, S., Park, S.J., Kang, J., Choi, D., 2020. Development of a metal-to-metal imprinting process: transcription quality analysis and surface wettability characterization. Appl. Surf. Sci. 527, 146823.

Li, J., Lu, Y.H., 2013. Effects of displacement amplitude on fretting wear behaviors and mechanism of Inconel 600 alloy. Wear 304, 223–230.

Liang, L., Chen, L., Wu, L., and Tan, H., 2021, "Interface Strength, Damage and Fracture Between Ceramic Films and Metallic Substrates," *Materials 14,* p. 353.

Lim, Y., Venugopal, R., Ulsoy, A.G., 2014. Process Control for Sheet-Metal Stamping: Process Modeling, Controller Design and Shop-Floor Implementation. Springer-Verlag, London, UK.

Lin, P., Shen, F., Yeo, A., Liu, B., Xue, M., Xu, H., and Zhou, K., 2017, "Characterization of Interfacial Delamination in Multi-Layered Integrated Circuit Packaging," *Surf. Coat. Techno*l. 320, pp. 349–356.

Liu, M., and Yang, F. Q., 2012, "Finite Element Analysis of the Indentation-Induced Delamination of Bi-Layer Structures," *J. Comput. Theoret. Nanosci.* 9, pp. 851–858.

Long, H., Liang, L., and Wei, Y., 2019, "Failure Characterization of Solid Structures Based on an Equivalence of Cohesive Zone Model," *Int. J. Solids Struct*. 163, pp. 194–210.

Long, Y., Twiefel, J., Wallaschek, J., 2017. A review on the mechanisms of ultrasonic wedge-wedge bonding. J. Mater. Process. Technol. 245, 241–258.

Lou, Y., Yoon, J.W., Huh, H., 2014. Modeling of shear ductile fracture considering a changeable cut-off value for stress triaxiality. Int. J. Plast. 54, 56–80.

Majumdar, A., Bhushan, B., 1990. Role of fractal geometry in roughness characterization and contact mechanics of surfaces. ASME J. Tribol. 112, 205–216.

Majumdar, A., Bhushan, B., 1991. Fractal model of elastic-plastic contact between rough surfaces. ASME J. Tribol. 113, 1–11.

Mandelbrot, B., 1967. "How long is the coast of Britain?" Statistical self-similarity and fractional dimension. Science 156, 636–638.

Martínez, F.J., Canales, M., Izquierdo, S., Jiménez, M.A., Martínez, M.A., 2012. Finite element implementation and validation of wear modelling in sliding polymer–metal contacts. Wear 284–285, 52–64.

McColl, I.R., Ding, J., Leen, S.B., 2004. Finite element simulation and experimental validation of fretting wear. Wear 256, 1114–1127.

Mindlin, R.D., 1949. Compliance of elastic bodies in contact. ASME J. Appl. Mech. 16, 259–268.

Mindlin, R.D., Deresiewicz, H., 1953. Elastic spheres in contact under varying oblique forces. ASME J. Appl. Mech. 20, 327–344.

Morris, B. A., 2022, *The Science and Technology of Flexible Packaging: Multilayer Films from Resin and Process to End Use*, 2nd edition, Elsevier.

Mostaani, A., Pereira, M.P., Rolfe, B.F., 2015. Comparison of ductile damage models during scratch tests – A numerical study. Proc. 8th Int. Conf. BALTTRIB'2015, 26-27 Nov. 2015, pp. 126-133.

Mróz, Z., and Mróz, K. P., 2015, "Analysis of Delamination and Damage Growth in Joined Bi-Layer Systems," *Geomech. Energy Environ*. 4, pp. 4–28.

Murthy, A. K., Komvopoulos, K., and Brown, S. D., 1990, "Processing and Characterization of Multi-Layered Wear-Resistant Ceramic Coatings," ASME *J. Eng. Mater. Technol.* 112, pp. 164–174.

Nagarathnam, K., and Komvopoulos, K., 1993, "Microstructural Characterization and *In Situ* Transmission Electron Microscopy Analysis of Laser-Processed and Thermally Treated Fe-Cr-W-C Clad Coatings," *Metal. Trans. A* 24A, pp. 1621–1629.

Oh, S.I., 1982. Finite element analysis of metal forming processes with arbitrarily shaped dies. Int. J. Mech. Sci. 24, 479–493.

Pereira, K., Yue, T., Abdel Wahab, M., 2017. Multiscale analysis of the effect of roughness on fretting wear. Tribol. Int. 110, 222–231.

Pourdavoud, N., Wang, S., Mayer, A., Hu, T., Chen, Y., Marianovich, A., Kowalsky, W., Heiderhoff, R., Scheer, H.-C., Riedl, T., 2017. Photonic nanostructures patterned by thermal nanoimprint directly into organo-metal halide perovskites. Adv. Mater. 29, 1605003.

Rashad, M., Pan, F., Yu, Z., Asif, M., Lin, H., Pan, R., 2015. Investigation on microstructural, mechanical and electrochemical properties of aluminum composites reinforced with graphene nanoplatelets. Prog. Nat. Sci. Mater. Int. 25, 460–470.

Riccardi, A, Montanari, R., 2004. Indentation of metals by a flat-ended cylindrical punch. Mater. Sci. Eng. A 381, 281–291.

Rocha, R. J. B., and Campilho, R. D. S. G., 2018, "Evaluation of Different Modelling Conditions in the Cohesive Zone Analysis of Single-Lap Bonded Joints," *J. Adhes.* 94, pp. 562–582.

Sahoo, P., Ghosh, N., 2007. Finite element contact analysis of fractal surfaces. *J. Phys. D* 40, 4245–4252.

Salib, J., Kligerman, Y., Etsion, I., 2008. A model for potential adhesive wear particle at sliding inception of a spherical contact. Tribol. Lett. 30, 225–233.

Sarkar, S., Singh, I.V., Mishra, B.K., Shedbale, A.S., Poh, L.H., 2019. A comparative study and ABAQUS implementation of conventional and localizing gradient enhanced damage models. Finite Elem. Anal. Des. 160, 1–31.

Shiotsu, T., Uemura, K., Tochino, T., Ooi, S., Onishi, Y., Yasuda, M., Kawata, H., Kobayashi, T., Hirai, Y., 2014. Simulation of the template release process based on fracture mechanics in nanoimprint lithography. Microelectron. Eng. 123, 105–111.

Song, Z., and Komvopoulos, K., 2013, "Delamination of an Elastic Film from an Elastic–Plastic Substrate During Adhesive Contact Loading and Unloading," *Int. J. Solids Struct.* 50, pp. 2549–2560.

Song, Z., Komvopoulos, K., 2014. Contact mechanics analysis of oscillatory sliding of a rigid fractal surface against an elastic–plastic half-space. Philo. Mag. 94, 3215–3233.

Soroush, M., Malekzadeh Fard, K., and Shahravi, M., 2018, "Finite Element Simulation of Interlaminar and Intralaminar Damage in Laminated Composite Plates Subjected to Impact," *Lat. Am. J. Solids Struc*t. 15, p. e90.

Suh, N. P., 1973, "The Delamination Theory of Wear," *Wear* 25, pp. 111–124.

Tabakov, V. P., Vereschaka, A. S., and Alexey A. Vereschaka, A. A., 2017, "Multilayer Composition Coatings for Cutting Tools: Formation and Performance Properties," *Mech. Ind.* 18, p. 706.

Traub, M.C., Longsine, W., Truskett, V.N., 2016. Advances in nanoimprint lithography. Annu. Rev. Chem. Biomol. Eng. 7, 583–604.

Turon, A., Dávila, C. G., Camanho, P. P., and Costa, J., 2007, "An Engineering Solution for Mesh Size Effects in the Simulation of Delamination Using Cohesive Zone Models," *Eng. Fract. Mech.* 74, pp. 1665–1682.

Ügdüler, S., De Somer, T., Van Geem, K. M., Roosen, M., Kulawig, A., Leineweber, R., and De Meester, S., 2021, "Towards a Better Understanding of Delamination of Multilayer Flexible Packaging Films by Carboxylic Acids," *ChemSusChem* 14, pp. 4198–421.

Vingsbo, O., Söderberg, S., 1988. On fretting maps. Wear 126, 131–147.

Voevodin, A. A., Schneider, J. M., Rebholz, C., and Matthews, A., 1996, "Multilayer Composite Ceramicmetal-DLC Coatings for Sliding Wear Applications," *Tribol. Int*. 29, pp. 559–570.

Walter, T., Lederer, M., and Khatibi, G., 2016, "Delamination of Polyimide/Cu Films Under Mixed Mode Loading," *Microelect. Rel.* 64, pp. 281–286.

Wang, N.-M., Budiansky, 1978. Analysis of sheet metal stamping by a finite-element method. ASME J. Appl. Mech. 45, 73–82.

Wang, S., Khatir, S., Abdel Wahab, M., 2020. Proper orthogonal decomposition for the prediction of fretting wear characteristics. Tribol. Int. 152, 106545.

Wang, S., Komvopoulos, K., 1994a. A fractal theory of the interfacial temperature distribution in the slow sliding regime: Part I – Elastic contact and heat transfer analysis. ASME. *J. Tribol.* 116, 812–822.

Wang, S., Komvopoulos, K., 1994b. A fractal theory of the interfacial temperature distribution in the slow sliding regime: Part II – Multiple domains, elastoplastic contacts and applications. ASME J. Tribol. 116, 824–832.

Wang, S., Komvopoulos, K., 1995. A fractal theory of the temperature distribution at elastic contacts of fast sliding surfaces. ASME J. Tribol. 117, 203–215.

Waterhouse, R.B., 1984. Fretting wear. Wear 100, 107–118.

Xia, Y., Lim, B., 2010. Beyond the confines of templates. Nature 467, 923–924.

Xing, Y.M., Lu, J., 2004. An experimental study of residual stress induced by ultrasonic shot peening. J. Mater. Process. Technol. 152, 56–61.

Xu, A., Vodenitcharova, T., Kabir, K., Flores-Johnson, E.A., Hoffman, M., 2014. Finite element analysis of indentation of aluminium foam and sandwich panels with aluminium foam core. Mater. Sci. Eng. A 599, 125–133.

Yamamoto, M., Kuwabara, T., 2007. Micro form rolling: imprinting ability of microgrooves on metal shafts. J. Mater. Process. Technol. 201, 232–236.

Yan, W., Komvopoulos, K., 1998. Contact analysis of elastic-plastic fractal surfaces. J. Appl. Phys. 84, 3617–3624.

Yan, Y., and Shang, F., 2009, “Cohesive Zone Modeling of Interfacial Delamination in PZT Thin Films,” *Int. J. Solids Struct.* 46, pp. 2739–2749.

Yue, T., Abdel Wahab, M., 2017. Finite element analysis of fretting wear under variable coefficient of friction and different contact regimes. Tribol. Int. 107, 274–282.

Zhang, H., Etsion, I., 2021. Evolution of adhesive wear and friction in elastic-plastic spherical contact. Wear 478–479, 203915.

Zhang, L., Ma, S., Liu, D., Zhou, B., Markert, B., 2019. Fretting wear modelling incorporating cyclic ratcheting deformations and the debris evolution for Ti-6Al-4V. Tribol. Int. 136, 317–331.

Zhou, J., Komvopoulos, K., 2005. Nanoconfinement effect on the mechanical behavior of polymer thin films. Proc. Mater. Res. Soc. Symp. 880E, BB4.3.1–BB4.3.6.

Zhou, Z.R., Vincent, L., 1995. Mixed fretting regime. Wear 181–183, 531–536.

Zimniak, Z., Piela, A., 2000. Finite element analysis of a tailored blanks stamping process. J. Mater. Process. Technol. 106, 254–260.